Transport, clustering and chemical kinetics of cell surface molecules influenced by actomyosin cortex

by

Sk Raj Hossein

2021

A thesis submitted to
the Jawaharlal Nehru University for the degree of
Doctor of Philosophy

Certificate:

This is to certify that the thesis entitled **"Transport, clustering and chemical kinetics of cell surface molecules influenced by actomyosin cortex"** submitted by Sk Raj Hossein for the award of the degree of Doctor of Philosophy of Jawaharlal Nehru University is his original work. This has not been published or submitted to any other University for any other Degree or Diploma.

Prof. S. Sridhar
(Director)
Raman Research Institute
Bangalore 560 080
India

Prof. Pramod Pullarkat
(Thesis Co-Supervisor)

Prof. Madan Rao
(Thesis Supervisor)

Declaration:

I hereby declare that the work reported in this thesis is entirely original. This thesis is composed independently by me at Raman Research Institute under the supervision of Prof. Madan Rao. I further declare that the subject matter presented in this thesis has not previously formed the basis for the award of any degree, diploma, membership, associateship, fellowship or any other similar title of any university or institution.

Prof. Pramod Pullarkat
Raman Research Institute
(Thesis Co-Supervisor)

Prof. Madan Rao
National Centre for Biological Sciences
(Thesis Supervisor)

Sk Raj Hossein

Dedicated to

My Family

Acknowledgements

I am extremely grateful to my supervisor Prof. Madan Rao for his encouragement, guidance and support to complete my thesis work. I appreciate all his contributions of time and ideas to make my PhD work productive and stimulating. The joy and enthusiasm he has for research were motivational for me, even during tough times in the PhD. His contributions towards my academic improvements were fundamental but what really stood out to me was the gentleness and compassion he extended towards me. I am grateful to Prof. Pramod Pullarkat for being my co-supervisor and the constant support and suggestions during my research work. I would like to thank my thesis advisory committee members Prof. V.A. Raghunathan Prof. Abhishek Dhar for numerous helpful feed backs on various occasions throughout my PhD. I am grateful to Dr. Shashi Thutupalli and Prof. Satyajit Mayor for all their support during my PhD tenure. I would like to thank Prof. Chandan Dasgupta for many helpful discussions. I want to thank all the faculties who taught us in IISc and RRI for their invaluable teachings. I would like to thank Amitabh Dandapat and Kashinath Chakraborty for introducing me to the beauty of physics in my school days.

My life would have been difficult without all the support that I got from the scientific community in RRI, IISc and NCBS. After spending all these years alongside my lab members, I really think it could not have been better anywhere else. I would like to thank Debshankar, Amit, Alkesh, Krishnan, Saptarshi, Abhishek, Sujan, Ajay, Ishutesh, Jyothsna, Ayan, Amar, Rituparno, Suman, Amit Das, Kabir, Amit Singh, Alex, Richard, Pragya and Anirban for being there. I would like to thank Sushil, Meera, Niranjan, Sabbir, Raviranjan, Karamveer, Shivam, Aniruddh, Kartick, Abir, Deepak, Amrita, Safi, Nazma, Debashish, Anagha, Samim, Rajib, Chaitra and many other friends in RRI for all the joyful moments we shared. I would like to thank Adhip, Pranab for their friendship and help. I would like to thank

Rahul, Aswini, Abrar, Darius, Suvrajit, Shankarshan, Aniruddh, and many other friends in NCBS for insightful discussions. In Bangalore, I always felt at home with the company of Sumit, Saiantan, Tathagata, Tanujit, Moumita, Sufiraja, Anjana, Jyoti, Debsankar, Santanu, Debadrita and Rituparno. Its not possible to thank you enough for all the experiences that we shared. I would also like to thank my school and collage friends Mrinmoy, Jaman, Noor, Rajsekhar, Rajkumar, Mithun, Prosenjit, Utpal, Sutapa, Iyamin and Alomgir for all the fantastic times we have shared.

I would specially like to thank Santanu and Amit for being with me throughout. Jyoti and Debshankar and Debadrita gave all the care I needed. My heartfelt thanks to Rituparno. His contribution towards the completion of this work has been massive. When nothing worked in life, he was always there to help me with his endless compassion and love. Some of my fondest memories revolve around the countless hearty and entertaining discussions with Debadrita and Rituparno over anything from music, politics, literature, art, religion, food, movies and even soap operas. It will only make me emotional if I continue hence let me stop here and recall all our cherished moments together.

I would like to thank people at RRI admin for helping me whenever the need was there. I would like to thank Radha, Marisa, Vidya and Gayathri for all their help. I would also like to thank NCBS administration for hosting me and for all help and support.

Finally, I would like to state that any amount of acknowledgement that I can express towards my family will not be enough: whatever good that is there in me has come from all of them. I express my deepest gratitude to my parents for their constant support and sacrifice. I thank my grandparents and uncles for everything they have done for my well being. I would like to thank my younger brothers Imdad and Sarif for taking significant responsibilities at home and encouraging me throughout this journey. I would like to thank my little sister Nargis for always cheering me and all other members of my family for their unconditional love and support.

Synopsis

The cell membrane is the gateway between the outside and the inside of the cell. The cell membrane, a multicomponent bilayer, comprising lipids, proteins and sugars, plays an essential role in *signalling* or transfer of information, *sorting* or the processing of information, and endo/exo-cytosis or the transfer of molecules, together with the transfer of small molecules and ions. These fundamental cellular processes are crucially dependent on the spatio-temporal organization and control of membrane molecules. Given the importance of molecular organization in the membrane, not surprisingly, there have been many studies devoted to this, and many models proposed to describe the organization and regulation of the cell membrane. Amongst these, the most influential models have been the *Fluid Mosaic* and the *Lipid Raft* models - both these models are grounded in the equilibrium physics of the lipid membrane and treat the cell membrane, with its constituent lipids and proteins as an independent organ. However, many recent experiments have established that the plasma membrane is intimately coupled to the actomyosin cortex. This actomyosin cortex is a thin, $\approx 200\,\mathrm{nm}$, fluid layer adjoining the plasma membrane, that largely comprises of actin cytoskeleton and myosin motors. Many cell membrane molecules can bind, directly or indirectly, to cortical actin. The cell membrane thus experiences active stresses, both systematic and stochastic, arising from the nonequilibrium dynamics of actomyosin cortex. These stresses effect the dynamics of the cell membrane shape and the local clustering and transport of cell membrane molecules. In other words, the spatio-temporal organizations of cell membrane molecules are strongly influenced by the intimate coupling to the active actomyosin cortex (and vice-versa). This leads to the description of the cell surface as an *Active Composite* of a multicomponent, asymmetric bilayer juxtaposed with a thin cortical actomyosin layer - a fundamentally nonequilibrium description of the cell surface organization that appears to consistently explain many experimental

results.

This thesis is a theoretical study of the in-plane Transport, Clustering and Chemical Reaction kinetics of cell membrane molecules within a model of the Active Composite Cell Surface.

Transport kinetics of cell-surface molecules influenced by the actomyosin cortex

In the active composite model, the coupling of the membrane to actin configurations is expected to affect the dynamics and organization of the membrane components. A coarse-grained active hydrodynamics description of the active composite cell surface [1, 2] successfully explains statistics of density fluctuations and transport of such actin-binding membrane proteins observed in experiments [3, 4]. Much of these behaviours were recapitulated in a minimal *in vitro* system comprising a thin layer of short actin filaments and Myosin-II minifilaments on a supported bilayer[5]. These experiments have been the primary motivation for the agent-based Brownian dynamics simulations described in this thesis. These simulations use the minimal ingredients incorporated in the ıin vitro setup - that of a collection of molecules which bind/unbind to actin filaments and move in the active medium comprising actin and myosin in two and quasi-two dimensions.

The results on cluster statistics and transport kinetics, based on simulations and analytical calculations, are in qualitative agreement with the experiments both *in vivo* and *in vitro*. For instance, the exponential tails appearing in the probability distribution of the number and the scaling of the variance of the number is precisely the behaviour seen in earlier *in vitro* experiments. In addition, calculating the radial distribution function, we show how activity-induced clustering of passive particles arises naturally from such a minimal description. We have also found that there is a crossover from an intermediate time super-diffusive to late time diffusive behaviour as a consequence of active driving. The transport behaviour shows a striking dependence on temperature and active forcing - at low temperatures, the diffusion coefficient is insensitive to temperature, and crosses over to a linear temperature

dependence at higher temperatures, in qualitative agreement with experiment [4]. Finally, recognizing that the viscosity of the cortical layer is different from that of the membrane, we show that a friction coefficient mismatch has a strong effect on the mean number of bound particles and the diffusion coefficient. This opens up the possibility of local tuning of viscosity mismatch, for instance, by locally recruiting the so-called "membrane rafts" or liquid-ordered regions on the cell membrane or by locally regulating the concentrations of actin, myosin or cross-linkers. This could result in yet another mechanism by which the cell surface might locally control the clustering and transport of specific membrane proteins.

Membrane-Cortex composite as a random field glass with line-disorder

The diffusion constant of a typical protein in an intact plasma membrane is about 20-fold less than those in an artificial membrane. This was a serious puzzle, till the development of high-speed cameras for single-molecule tracking showed that the plasma membrane is partitioned into compartments induced by the cortical actin meshwork and membrane molecules get temporarily confined in these compartments, undergoing hop-diffusion [6]. Hop-diffusion of transmembrane proteins that possess a cytoplasmic domain is thought to result from the direct interaction between the protein molecules and the actin meshwork. However, the hop-diffusion of upper leaflet molecules which do not have direct binding to the actin cytoskeleton is far more puzzling. The *Picket-Fence* model was proposed to account for hop-diffusion of these molecules [7]. In the picket-fence model, a fraction of transmembrane protein (picket) is immobilized by binding to the membrane skeleton (fence) and forms compartments for other unbound molecules. This serves as an obstacle for lateral diffusion of membrane molecules.

The successful interpretation of the diffusion coefficient mismatch by the picket-fence model has motivated us to study the underlying physics of cage-hopping transport in the vicinity of a random field-glass induced by the quenched random disposition of the cortical actin meshwork. The cortical meshwork adjoining the plasma membrane provides a quenched random environment with correlated line disorder. This pins those cell membrane molecules that directly bind to it, giving rise to

the suggested picket fence. This in turn, provides obstacles to other molecules, even small molecules such as upper leaflet lipids with no direct interaction with the cortical meshwork. This is a new model for random pinning and its influence on molecular transport, quite distinct from the random pinning potentials studied in the literature, in that the effects of topological confinement are significant. Our study is again based on a multi-agent Brownian dynamics simulation in quasi-two dimensions. Activity or dynamical remodelling of the picket-fence can lead to fluidisation and hence larger diffusive transport of the cell surface molecules.

Clustering and Chemical kinetics of interacting cell-surface molecules influenced by the actomyosin cortex

Many cell surface signalling protein receptors form transient clusters or signalling platforms, sites of efficient chemical reactions. Many studies of cell surface signalling have demonstrated the role of actin and myosin in the creation, maintenance and dissolution of these localised platforms. This provides the motivation for the study of chemical reaction kinetics within the Active Composite model of the cell surface.

We have studied the clustering and chemical kinetics of particles interacting with a fluid medium comprising actin filaments and myosin minifilaments using an agent-based Brownian dynamics simulation. As a result of the contractile activity of myosin minifilaments, the actin filaments are subjected to active forces and torques, that spontaneously generate flows and defects such as localised asters. This results in *both* enhanced active diffusive transport and transient clustering of particles that bind/unbind to actin. In the context of chemical reactions, both irreversible and reversible, this leads to a dramatic enhancement of chemical reaction rates (measured by the gain) compared to thermal equilibrium. Our numerical results can be understood using a mean-field calculation based on the Smoluchowski's diffusion-controlled reaction theory. Both simulations and mean-field theory suggest a optimum chemical reaction output as a function of the active driving, which in the Active Composite picture, is locally regulatable by the cell.

Synopsis

Prof. Madan Rao Sk Raj Hossein

Simons Centre for the Study of Living Machines
National Centre for Biological Sciences (TIFR)
Bengaluru 560 065
India

References

[1] K. Gowrishankar, S. Ghosh, S. Saha, C. Rumamol, S. Mayor, and M. Rao, Cell **149**, 1353 (2012).

[2] K. Gowrishankar, and M. Rao, Soft Matter **12**, (2016).

[3] D. Goswami, K. Gowrishankar, S. Bilgrami, S. Ghosh, R. Raghupathy, R. Chadda, R. Vishwakarma, M. Rao, and S. Mayor, Cell **135**, 1085 (2008).

[4] S. Saha, I.-H. Lee, A. Polley, J. T. Groves, M. Rao, and S. Mayor, Molecular biology of the cell **26**, 4033 (2015).

[5] D. V. Köster, K. Husain, E. Iljazi, A. Bhat, P. Bieling, R. D. Mullins, M. Rao, and S. Mayor, Proceedings of the National Academy of Sciences **113**, E1645 (2016).

[6] A. Kusumi, Y. Sako, and M. Yamamoto, Biophysical journal, **65**, (1993).

[7] T. Fujiwara, K. Ritchie, H. Murakoshi, K. Jacobson and A. Kusumi, J. Cell Biol. **157**, 904 (2002).

Publications

- Interacting passive advective scalars in an active medium
  Sk Raj Hossein, Ritparno Mandal, and Madan Rao
  Physical Review E **98**, 052608 (2018)
  doi:10.1103/PhysRevE.98.052608

- Stratification, multivalency and turnover of the active cortical machinery are required for steady active contractile flows at the cell surface
  Sk Raj Hossein, Ritparno Mandal, and Madan Rao
  arXiv:2105.11358, cond-mat.soft, (2021)

Contents

List of Figures

List of Tables

Chapter 1

Introduction

1.1 Cell surface organization and function

All cells sense the environment and interact with the outside world to serve different functions. These actions take place on the cell membrane, a multicomponent bilayer comprising lipids, proteins and sugars. For example, the cell membrane plays an essential role in the processing and transfer of information [1]. This cell signalling mechanism makes it possible for cells to respond appropriately to a specific environmental stimulus. Cell receive information from the environment and transmit it into the intracellular space through a sophisticated molecular system on the cell surface. Signalling molecules integrate the information into a directed pathway. Recent developments in experimental techniques have established that the spatio-temporal organisation [2, 3, 4] of signalling molecules (receptors) is crucial for the cell to distinguishing weak signals from a very noisy environmental background with high precision and sensitivity.

1.1.1 Equilibrium Organization of cell membrane

Given the importance of molecular organisation in the membrane, not surprisingly, many studies have been done, and models have been proposed to answer how organisation takes place on the cell surface and how a cell benefits from this. Among these, the most influential models have been the Fluid mosaic [5] and Lipid Raft [6] models. The organisation of lipid and proteins in the cell membrane has typically been described in terms of equilibrium models of lateral organisation of multicom-

ponent lipids [5, 6, 7, 8, 9]. The multicomponent lipid equilibrium phase diagram in temperature and composition shows either in the homogeneously mixed regime as envisaged by the famous Fluid mosaic model or a low-temperature phase segregated regime where the liquid-ordered phase of lipid (lo-lipid) is separated from the liquid disordered phase of lipid (ld-lipid) as proposed by the famous Raft model.

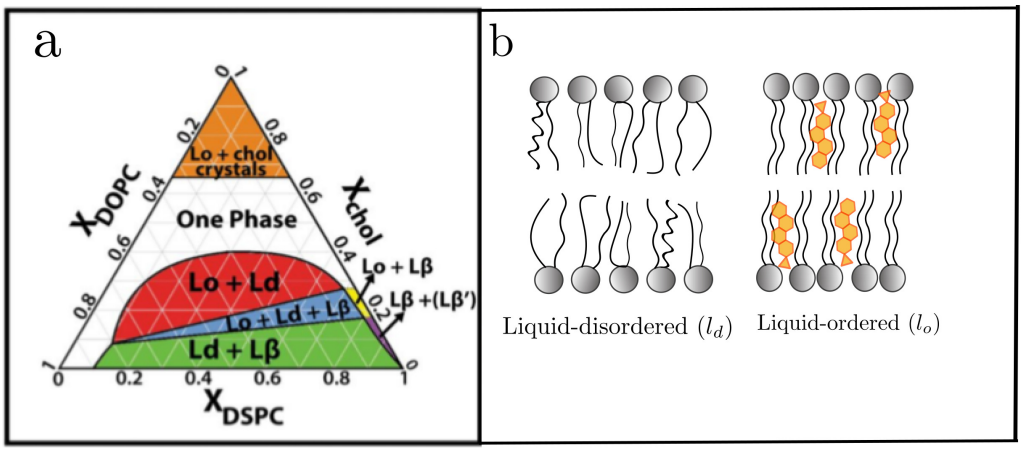

Figure 1.1 (a) Ternary phase diagram for DSPC/DOPC/chol at 23 °C. Numbers on the DOPC-DSPC axis correspond to DSPC, numbers on the DSPC-cholesterol axes to CHOL (Image Courtesy : [10]). (b) Organization of lipid molecules in the liquid ordered (lo-lipid) and the liquid disordered phase is shown here. Liquid ordered phase is a mixture of cholesterol (yellow molecule) with a phospholipid and/or sphingolipids.

In both these models, protein organisation follows lipid organisation. According to the fluid mosaic model proposed by Singer and Nicolson, the plasma membrane in a living cell is a two dimensional fluid of lipid in which proteins of various shapes and sizes are embedded in a mosaic-like fashion. Above the phase segregation temperature, the lipid bilayer exists in a fluid phase, characterised by disordered lipid chains and high lipid mobility. The presence of cholesterol in rafts leads to a tighter packing of lipid chains, which results in lower lateral mobility of lipids in the raft domain below phase segregation temperature. Proteins get segregated according to their affinity to the component of the raft lipid phase. Thus rafts can act as a sorting platform which compartmentalises cellular process. However, such lipid segregation, as seen here in giant plasma membrane vesicles derived from the cell membrane is only observed at low temperature (23 °C - 5 °C), much lower than the

physiological temperature (37 °C) [8]. Both of these models treat the cell membrane as an independent organelle and are based on the equilibrium physics.

1.1.2 Active Organization of cell membrane

Recent experiments have established that the plasma membrane is intimately coupled to the actomyosin cortex [20, 21, 22, 23, 24]. The actomyosin cortex is a 200 *nm* thin layer [26] comprising of the actin-cytoskeleton and myosin motors, sitting just beneath the plasma membrane. Recent advances in fluorescence spectroscopy experiments and high optical resolution microscopy have provided indisputable evidence for nanoclusters of many membrane molecules. Experimental findings based on fluorescence resonance energy transfer (FRET) analysis [11] on the organisation of both upper leaflet GPI anchored lipid tethered protein (GPI-AP) and a variety of trans membrane proteins revealed the existence of a large population of nanoclusters. Later, it has been found by Sharma et al. [12] using a combination of homo and hetero FRET that GPI-APs co-exists on the cell membrane as a mixture of nearly 30% oligomers composed of mostly four molecules. As argued in Rao et. al.[13] the concentration-independent steady-state percentage of GPI-APs nanoclusters suggests that this mechanism is out of chemical equilibrium. Later, super-resolution microscopy techniques such as near field scanning optical microscopy (NSOM) [14] and photoactivated localisation microscopy (PALM) [15] confirmed the GPI-AP nanoclustering. Further evidence for the existence of nanoclusters has been provided by single-particle tracking (SPT) experiment and fluorescence correlation spectroscopy (FCS) on nano volumes [16]. Ras family of GTPases [2], T cell receptors and B cell receptors [17] are also shown to form nanoclusters. Such protein nanoclustering and their functional implications are a subject of intense investigation.

The ubiquitous presence of protein nanoclusters in the plasma membrane leads to the crucial question of why nature has chosen this feature. One possible answer might be that this provides multiple, ligand-binding sites in close proximity [18]. The clustered ligand binding sites increase the ligand rebinding probability. Moreover, the nanoclusters might increase the effective ligand-binding affinity for multivalent ligands. The nanoclusters in the plasma membrane offer a general way to digitalised analogue input signals. The nanoclusters provide a discrete switch-like

output because of their short lifetime. For example, the ligation of the EGF receptor nanocluster activates K-Ras, which acts as digital signalling molecule to the downstream kinase signalling cascade [19]. This allows the pathway to be sensitive to a small amount of activating ligand.

These nanoclusters are very dynamic, and indeed, as one perturbs the myosin contractility or perturbs the level of cholesterol in the case of GPI anchored protein, these nanoclusters disappear and gives rise to fragmented monomeric configuration [11, 12, 20]. Interestingly one could restore the nanoclusters by restoring the amount of actomyosin contractility and cholesterol in the case of GPI anchored proteins. This dramatically indicates that these dynamic nanocluster are contingent on non-equilibrium forces arising from actomyosin contractility. These observations provided motivation for the cell surface model as an active composite [21] of a multicomponent, asymmetric bilayer juxtaposed with a thin cortical actomyosin layer. This fundamental non-equilibrium description of the cell surface organisation consistently explains many experimental results.

1.2 Active Composite cell surface

Recent experiments have established that the plasma membrane must always be thought of in the context of the actomyosin cortex, as a composite [13, 20, 21, 22, 23, 24]. Here, we will ignore the molecular details and present a coarse-grained physical structure of the membrane composite comprising of: i) plasma membrane and ii) actomyosin cortex. We will emphasise the non-equilibrium nature of the cell surface, which is taken into account in the active composite model[21, 25] of the cell surface.

1.2.1 Plasma membrane

The plasma membrane is a thin (5-10 nm) semipermeable lipid layer that separates the interior of the cell from the outside environment. This continuous, unbroken fluid sheet not only protect the cell and provides a fixed environment inside the cell; but also functions as a gateway for the cell. Plasma membrane regulates the

transport of nutrients, essential manufactured molecules (hormones, enzyme) and toxic material inside and outside the cell. The plasma membrane plays a crucial role in the response of the cell to external stimuli. This process is known as signal transduction. Receptors in the plasma membrane combine with the stimuli (binding of ligands). Due to an external stimulus may cause the membrane to generate a signal that stimulates or inhibits internal activities. The principal components of the plasma membrane are phospholipids, cholesterol, proteins and carbohydrate groups. The main fabric of the plasma membrane is the phospholipids. The most celebrated model of plasma membrane organisation is a fluid-mosaic model, proposed by Singer and Nicolson in 1972. The bilayer of a fluid-mosaic membrane is present in a fluid state, and individual lipid molecules can move laterally within the plane of the membrane. The structure and arrangement of membrane proteins in the fluid-mosaic model occur as a mosaic that penetrate the lipid sheet. Most importantly, the fluid-mosaic model presents cellular membranes as dynamic structures in which the components are mobile and capable of coming together to engage in various types of interactions. The mobility of individual lipid molecules within the bilayer of the plasma membrane can be directly observed under the microscope by linking the polar heads of the lipids to gold particles or fluorescent compounds. It is estimated that a phospholipid can diffuse from one end of a bacterium to the other end in a second or two. In contrast, it takes a phospholipid molecule a matter of hours to days to move across to the other leaflet.

In artificial lipid bilayers, cholesterol and sphingolipids tend to self-assemble into microdomains. These patches of cholesterol and sphingolipid are referred to as lipid rafts. Proteins, such as GPI-anchored protein tend to clustered in these ordered lipid rafts. Attempts to demonstrate the presence of lipid rafts in living cell by conventional microscopy have generally been unsuccessful because of their short live and small size (5 to 25 nm diameter). The organisation of these rafts can be understood with the help of equilibrium physics of phase segregation. When a system is quenched from a homogeneous state above phase separation temperature (T_c) into an unstable state below T_c domains form in the system and evolve with time until the system reaches the phase separated equilibrium state. These domains coarsen and grows according to a power law $l(t) \sim t^{\alpha}$, where $l(t)$ is the characteristic size of the

domains. However this phase segregation has been observed in large vesicles formed from plasma membrane compounds (devoid of actin) at 5 °C - 20 °C and not at the physiological temperature 37 °C. So these equilibrium models where the protein organisation follow the lipid organisation are unable to explain the organisation of proteins in the cell membrane. Recent experiments have established that the plasma membrane is strongly coupled to the actomyosin cortex. Many plasma membrane proteins interact with the actomyosin cortex, and their dynamics are affected by the dynamics of the actomyosin cortex. In this thesis our objective is to study the dynamics of such proteins.

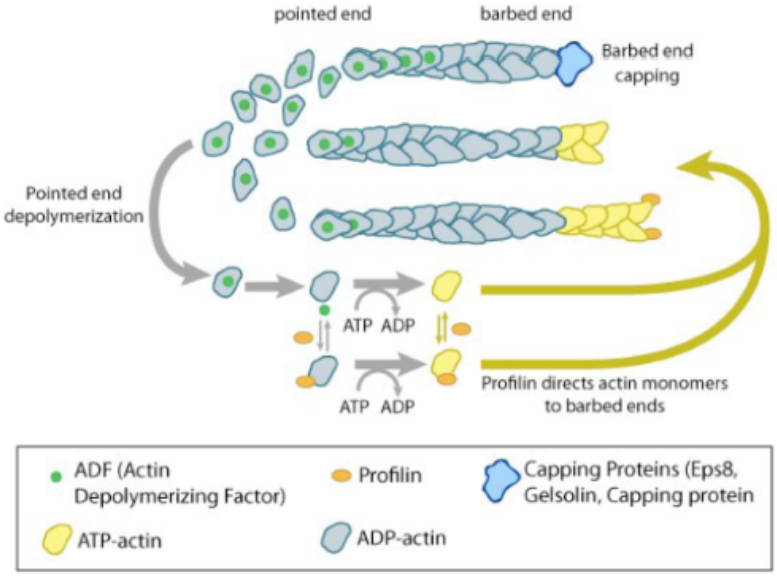

Figure 1.2 Polymerisation of actin filaments and treadmilling: ATP bound monomers get attached to the barbed end, and ADP bound monomers getting detached from the pointed end. In steady-state, actin filaments reach a constant length and a move with respect to the medium in a process called treadmilling. Profilin enhances the rate of attachment at the plus end while the capping proteins are used as length regulators (Image Courtesy: [27]).

.

1.2.2 Actomyosin cortex

The actomyosin cortex is a thin layer of the actin cytoskeleton and myosin motors. Its thickness varies from cell to cell ($\sim$250 nm in HeLa cells [26]). This thin film

sits just beneath the plasma membrane. The principal constituents of the cortex are actin, myosin, and lots of actomyosin regulators. First, we will discuss the physical properties of the building blocks, namely actin, myosin and then the combined actomyosin.

Actin

Actin filament comprising of actin monomers of size vary from $7 - 10\ nm$. The actin filament has a structural polarity due to head to tail assembly of the actin monomers. The two ends of the actin filament denoted as the minus (or pointed) and the plus (or barbed) ends. The polymerisation in the barbed is faster than the pointed end. Due to this asymmetry in polymerisation and depolymerisation filament move with respect to the medium. This phenomena called treadmilling is shown in Fig. 1.2.

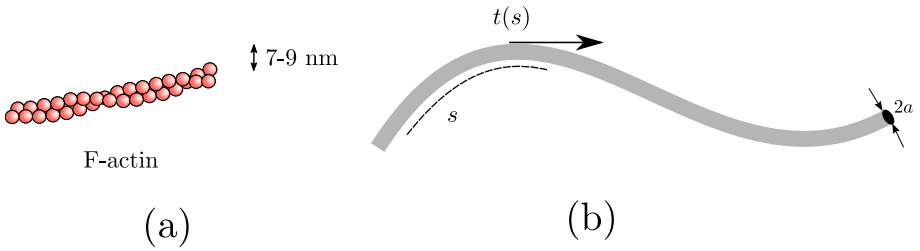

Figure 1.3 (a) The cytoskeletal actin filament. (b) Actin filament can be considered as an elastic rod, when the length of the rod is very long compared to the monomeric dimension a, and that the rigidity is high ($l_p \gg a$). This elastic curve can be characterized by the length s along its backbone and a unit tangent vector $\vec{t}$, defines the local orientation of the filament.

.

These are inextensible filaments and their length does not change significantly. Based on the mechanical properties actin filament can be described as semiflexible polymer. Semiflexible polymers mechanics are governed by the interplay between entropy and bending elasticity. This inextensible filaments with finite resistance to bending can be modelled as a worm-like chain (WLC) [28], where overlooking the chemistry behind the monomers, one can describe the filament as a semiflexible rod of thickness $2a$ and parametrised by an arc length s. As one moves along the filament, the local tangent vector changes. The curvature is simply the rate at which

the tangent vector changes as one moves along the arc length(s). The bending energy cost due to this curvature is given by

$$H_{bend} = \frac{\kappa}{2} \int ds \left| \frac{\partial \vec{t}}{\partial s} \right|^2 \tag{1.1}$$

The bending modulus κ has units of energy times length. A natural energy scale due to Brownian fluctuation is $k_B T$, where T is the temperature, and k_B is the Boltzmann's constant. Thus, one can define a length scale called the persistence length of the filament as being the ratio of the κ and thermal energy. The persistence length of $l_p = \kappa / k_B T$ is the characterisation of the stiffness of the filament. For actin filament, the value is around $\sim 10\ \mu m$. The contour length of the actin varies in a range from 200 nm to 5 μm within the cell. This lower limit might appear surprising. The typical length of the actin filament in cell is smaller than the persistence length. In electron microscopy, the actin cortex is visualised as densely crosslinked actin meshwork. The clustering dynamics and statistics of membrane-anchored proteins (GPI-APs) suggests a presence of active driving by more dynamic actin filament [21] behind their nanoclustering.

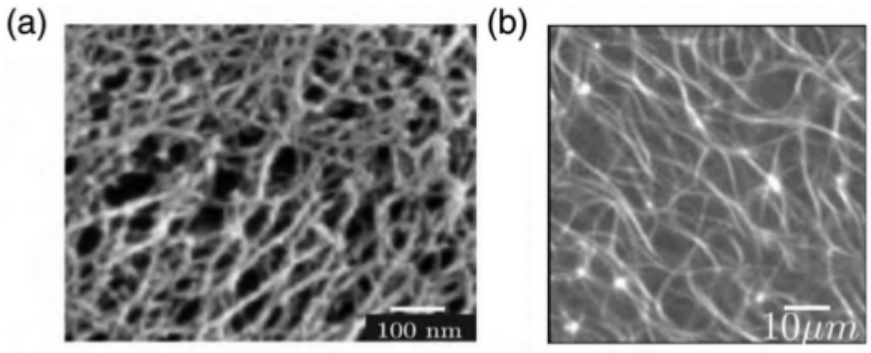

Figure 1.4 (a) Electron micrograph of a fixed and rotary-shadowed filamin-F-actin network at an actin concentration 1 mg/ml average filament length 15 μm. (b) Confocal microscopy image of a fluorescently labeled bundled filamin F-actin network at high filamin concentrations(Image courtesy [30]).

So, the actin cytoskeleton is simultaneously composed of dynamic actin filaments and dense, relatively static meshwork.

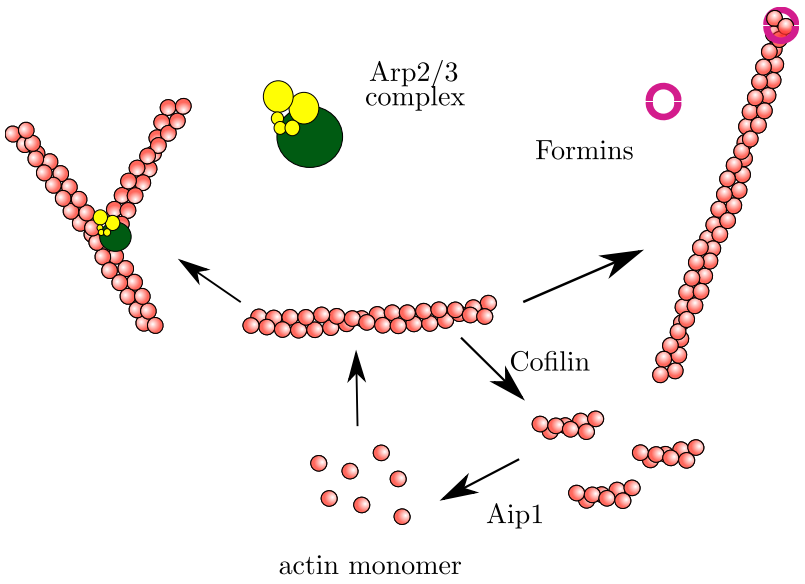

Figure 1.5 Schematic for formin nucleated linear actin filament (right) and Arp2/3 nucleated branched actin filament (left). Arp2/3 complex promotes the assembly of a new filament from the side of a preexisting one at a 70° Y-branched angle. Cofilin participates in active severing of actin filaments.

The actin filament appear both as linear filament and branched filament. The polar dynamic actin filaments are nucleated by Formin, and the branched actin filaments are nucleated by ARP complexes. In cells, actin filaments are organised either in the form of bundles or weblike networks. These different structures are initiated by the action of distinct nucleating proteins. The long straight filaments produced by formins make bundles, and the ARP complex makes webs. The mesh size ξ depends on the density of crosslinkers that binds to the actin. The presence of these crosslinkers is important in maintaining the contractile stress in this actin meshwork.

These structures are susceptible to de-polymerisation by cofilin. They serve as a severing agent i.e, they brake and cuts the filament at designated points. Due to both the breakages of the filament by cofilin and unbinding of crosslinkers, relaxation of stress happens. This turnover happens in a stress-dependent manner. The nucleation and growth of actin are governed by signalling processes. The turnover of actin and myosin is very much regulated in the cell when compared to in-vitro reconstitution experiments.

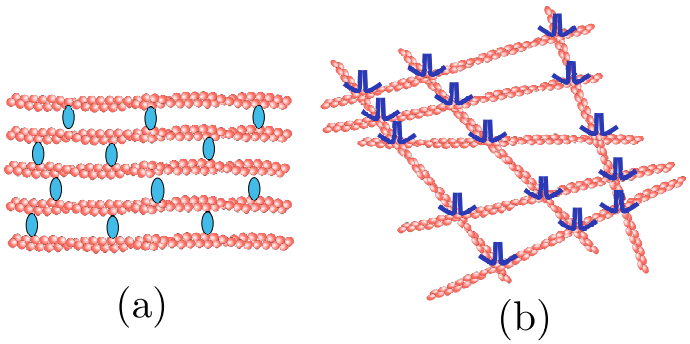

Figure 1.6 Actin cross-linking in various forms. (a) Fimbrin produces tight arrays of filaments by forming tight cross-links between parallel filaments. (b) Filamin dimers cross-links actin filaments towards formation of actin gels.

Actin cortex as a meshwork

The diffusion constant of molecules in an intact plasma membrane is about 20-fold less than those in an artificial membrane [31]. Several experiments have demonstrated that this slowdown in the intact plasma membrane is due to the coupling between membrane and actin cytoskeleton [31, 32, 33, 36]. The development of high-speed cameras for single-molecule tracking showed that the plasma membrane is partitioned into compartments induced by the cortical actin meshwork and membrane molecules get temporarily confined in these compartments, undergoing hop-diffusion. Hop-diffusion is characterised by a large microscopic diffusion coefficient (5-10 $\mu m^2 s^{-1}$) at short time (0.1 ms) within a compartment and a smaller, macroscopic diffusion coefficient (0.2-0.5 $\mu m^2 s^{-1}$) at long times ($>$ 10 ms), which is determined by the confinement time and compartment size. Hop-diffusion of transmembrane proteins that possess a cytoplasmic domain is thought to result from the direct interaction between the protein molecules and the actin meshwork. However, the hop-diffusion of upper leaflet molecules which do not have any direct or indirect binding site to the actin cytoskeleton is far more puzzling. The picket-fence model was proposed to account for hop-diffusion of these molecules. In the picket-fence model, a fraction of transmembrane protein (picket) is immobilised by binding to the membrane skeleton (fence) and forms compartments for other unbound molecules. This serves as an obstacle for lateral diffusion of membrane molecules.

Myosin

Another essential constituent of the actomyosin cortex is myosin which is a molecular motor. Myosin plays a vital role in several cellular processes such as cell adhesion, cell migration, muscle contraction, etc., where force sensing and stress generation are involved. Myosin has an actin-binding site and ATP binding site in there head, followed by a long neck. A vast family of myosin is present in the cell, namely Myosin-I, Myosin-II and so on. They can be classified on the basis of structure, size, the number of motorheads and their cellular localization. Myo-II has two motorheads and localizes in the actin cortex, beneath the plasma membrane and in stress fibres.

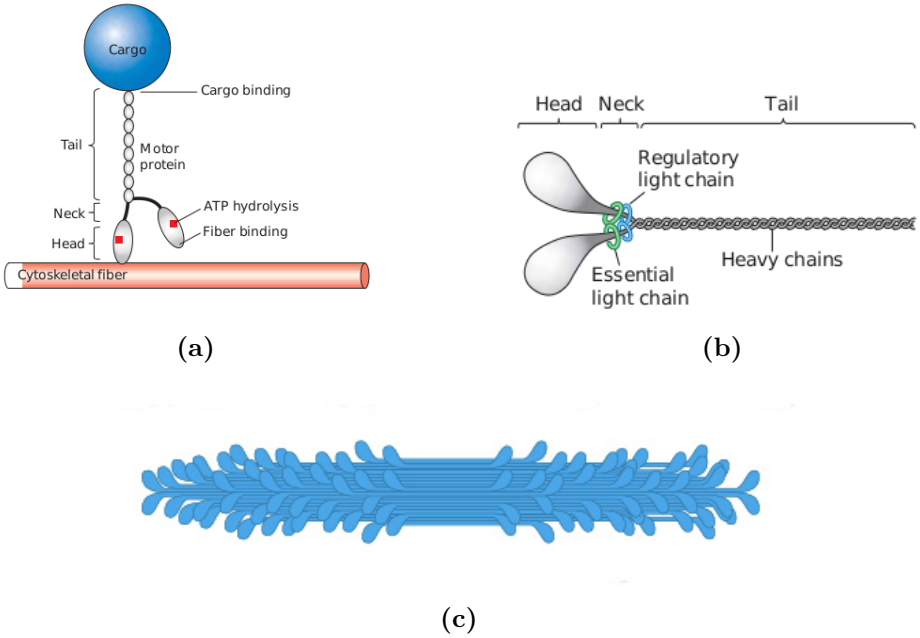

Figure 1.7 (a) Myosin motors carrying cargo on a actin filament track. (b) Myosin II molecule composed of two heavy chains and four light chains. The light chains are two types, and one copy of each present on on each myosin head. (c) Myosin II forms bundles which is called myosin minifilament(Image Courtesy: [37]).

Its head binds to the actin filament and hydrolyses ATP; using the energy of ATP hydrolysis, it literally walks on the actin filament. The tail domain assembles myosin II molecules into bipolar filaments with motorheads on the two ends and the tails packed in the centre (Fig. 1.7c). These bundles form a myosin minifilament. Each

bundle has around 30-50 myosin heads. The size of myosin minifilament is around 300 nm.

Combined Actomyosin Unit

We have talked about actin and myosin separately. Now, we will bring them together and discuss about the active current and stresses generated by the actomyosin unit. The head of the Myosin-II motor binds to the actin filament and selectively move towards the plus end of actin filament. This walking of myosin motor can move actin filament around, when the myosin minifilament is held on the other side. This gives rise to a current, which is proportional to the orientation of the actin filament. The bipolar architecture of myosin minifilaments allows it to slide antiparallel actin filaments with respect to each other. This sliding activity can give rise to either a contractile or an extensile force, depending on the arrangement of the actin filaments [38]. Remarkably, in the cell contractile arrengments are seen. The bias of actin-myosin assembly towards contraction and the mechanism behind the contractile activity is still a subject of investigation. One answer lies in the buckling of actin filaments. Actin filaments are semiflexible polymer with persistence length 10 μm. They can resist stretching but readily buckle under the compression force induced by myosin motors. Computational models show that buckling can cause a contraction in both bundle and networks [39, 40]. In-vitro experiments support these predictions [41]. Another proposed mechanism behaind this contraction is polarity sorting of filament by myosin motor. The directional movement of motors along actin leads to this polarity sorting. This process shows a contraction of filaments in the absence of buckling. Analytical prediction of polarity sorting of the filaments [42, 43] has been observed in in-vitro experiments [44] and as well as in cell [45]. In -vitro expriment shows formation of a radial array of filaments known as aster, where the plus end of the filaments are inward and myosin motor accumulate at the centre [44]. This is a clear signature of polarity sorting. This process generates flow in the actomyosin cortex and eventually, it contracts.

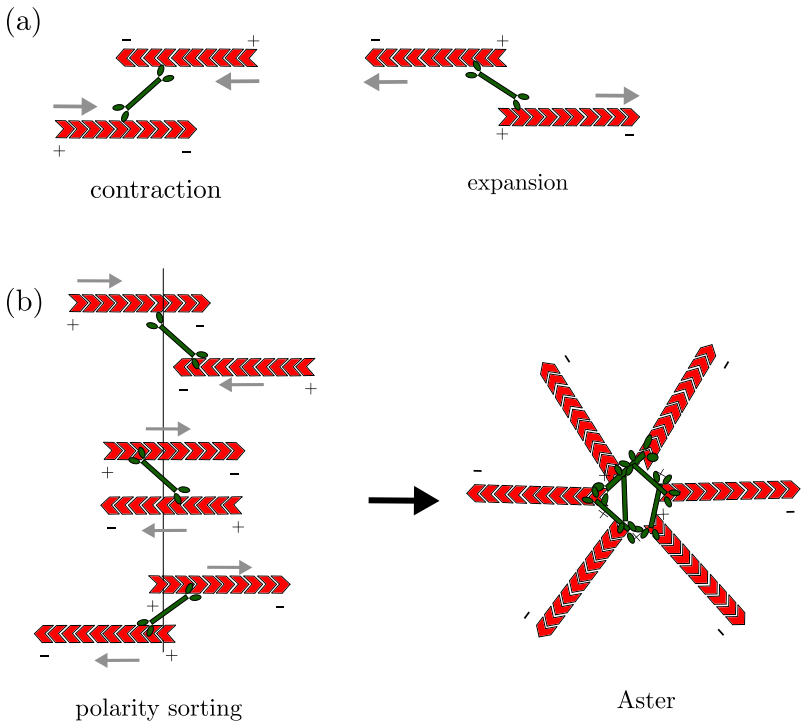

Figure 1.8 Active current and active stresses generated by the actomyosin unit. (a) Contractile and extensile actomyosin configurations due to myosin sliding on a pair of actin filaments. (b) Polarity sorting capacity of Myosin minifilament leads actin filaments towards aster formation.

1.3 Active mechanics of the cell surface: Continuum hydrodynamics

The collection of actin filament and myosin-II motors can be thought as an active fluid. It behaves like a fluid in the dilute or semidilute limit for a small filament length. This fluid description could be valid when the crosslinker density is low, and the turnover of crosslinkers is fast. The continuum hydrodynamics description [21, 46] of this active fluid is an extension of nematohydrodynamics [48]. Active matter consists of active agents, each capable of consuming energy and use that energy to generate directed motion and stresses. Active matter systems are out of equilibrium, and the defining difference with the other familiar nonequilibrium system is in the nature of energy input. The energy input for the active matter system is local, at the level of each particle, rather than at the system's boundaries as in a shear flow.

Active systems exhibit emergent structures with collective behaviour, anomalous fluctuation statistics, nonequilibrium order-disorder transitions, pattern formation.

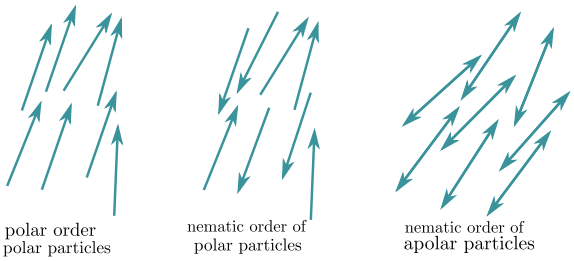

Figure 1.9 Schematic of the various orientationally ordered states. Polar active particles, have a head and a tail and are generally self-propelled along their long axis. They can order in polar states (left) or nematic states (center). Head-tail symmetric apolar active particles can order in nematic states (right).

The elongated self-propelled agents of active matter cooperatively order either in the polar phase or nematic phase depending on the nature of broken symmetry. In a polar phase, all the microscopic objects are on average aligned in the same direction. The polar order is described by a vector order parameter $\mathbf{p}$, known as the polarization. Nematic ordering can be obtained in two ways, either in systems where polar self-propelled objects are parallel but with random head-tail orientations or in systems where the self-propelled particles are themselves head-tail symmetric. Nematic order is described by a tensor order parameter $\mathbf{Q}$, known as the alignment tensor. A cartoon of the different cases is shown in Fig. 1.9. We can think the polar dynamic actin filaments as a polar active matter agent in a solvent. The dynamics of active polar actin filaments is described by their local density field $c(\mathbf{r},t)$ and local orientation field $\mathbf{n}(\mathbf{r},t)$ defined as [21, 46, 47]:

$$
\begin{aligned}
c(\mathbf{r},t) &= \sum_i \delta(\mathbf{r}-\mathbf{r}_i(t)) \\
\mathbf{n}(\mathbf{r},t) &= \frac{1}{c(\mathbf{r},t)} \sum_i \mathbf{n}_i(t)\delta(\mathbf{r}-\mathbf{r}_i(t))
\end{aligned}
\tag{1.2}
$$

where $\mathbf{r}_i$ and $\mathbf{n}_i$ are the position and orientation of the ith filament, respectively. Myosin can bind and unbind from the actin filament; the bound myosin density ρ comes into the equation. Finally, the entire actomyosin system is embedded in the cytoskeletal fluid, high viscous Stokesian fluid with viscosity η. Hydrodynamic

velocity can be ignored due to the damping coming from the local friction $\gamma = \frac{\eta}{\xi_l^2}$, through the cytoskeletal meshwork, with mesh size ξ_l. At time scale shorter than the filament turnover the actin concentration is conserved quantity and we can write,

$$\begin{aligned} \frac{\partial c}{\partial t} &= -\vec{\nabla} \cdot \mathbf{J}_f \\ \mathbf{J}_f &= -D_f(c,\rho)\vec{\nabla}c + v_f(c,\rho)c\mathbf{n} + c\mathbf{v} \end{aligned} \tag{1.3}$$

where filament current J_f can be written as a as the sum of three terms: a diffusive contribution $-D_f(c,\rho)\vec{\nabla}c$, a advective contribution $v_f(c,\rho)c\mathbf{n}$ and the advection with the fluid $c\mathbf{v}$. The diffusion has both thermal and active contribution which makes $D_f(\rho = 0) > 0$ in absence of myosin ($\rho = 0$). Minifilament cross-link the dynamic actin filaments to each other and to the mesh work. The advection term arise from the walking of myosin minifilaments on actin filament. In absence of myosin ($\rho = 0$) due to pure active contribution $v_f(\rho = 0) = 0$. Around the mean actin and myosin density $v_f(c_0, \rho_0) = v_0$.
The dynamics of myosin motor filaments bound to the actin can be described as:

$$\begin{aligned} \frac{\partial \rho}{\partial t} &= -\vec{\nabla} \cdot \mathbf{J}_m + k_{bind}(c) - k_u\rho \\ \mathbf{J}_m &= -D_m(\rho,c)\vec{\nabla}\rho + v_m(\rho,c)\rho\mathbf{n} + \rho\mathbf{v} \end{aligned} \tag{1.4}$$

where myosin current J_m has similar three terms as actin current: a diffusive contribution $-D_m(\rho,c)\vec{\nabla}\rho$, a advective contribution $v_m(\rho,c)\rho\mathbf{n}$ and the advection with the fluid $\rho\mathbf{v}$. The rate of myosin binding depends monotonically on local actin concentration with $k_{bind}(c = 0) = 0$ and assumption of unlimited bath of unbound myosin, we use saturating form $k_{bind}(c) = k_b(\frac{c}{c+c_h})$. The myosin turn over term can be written as $k_b(\frac{c}{c+c_h}) - k_u\rho$.

The equation for the orientation of actin filament can be written as an extension of nematohydrodynamics and Toner-Tu equation. The time derivative of the local orientation is given by

$$\frac{\partial \mathbf{n}}{\partial t} + \lambda(\mathbf{n}\cdot\vec{\nabla})\mathbf{n} = K\nabla^2\mathbf{n} + K_2\vec{\nabla}(\vec{\nabla}\cdot\mathbf{n}) - \xi_0\vec{\nabla}c + M(\rho)\vec{\nabla}\cdot\sigma^a + (\alpha(c) - \beta(c)n^2)\mathbf{n} \tag{1.5}$$

The non-linear convection term $\lambda(\mathbf{n}\cdot\vec{\nabla})\mathbf{n}$ arises from the advection of filament due to active stress. In 2D, there are two types of deformation splay and bend. The terms corresponding to these deformations are respectively $K\nabla^2\mathbf{n}$ and $K_2\vec{\nabla}(\vec{\nabla}\cdot\mathbf{n})$. A compressible term $\xi_0\vec{\nabla}c$, with positive compressibility ($\xi_0 > 0$), arises from the orientation of self-propelled filaments during their flow. The active contractile stress from the myosin is given by $M(\rho)\vec{\nabla}\cdot\bar{\sigma}^a$ [48, 49]. The contractile drive coming from the myosin can be expressed in a simple linear form $\bar{\sigma}^a = -W\rho\bar{I}$ with $W < 0$. The filaments at low density are expected to be orientationally isotropic, while at high concentration they are orientationally ordered. The term $(\alpha(c)-\beta(c)n^2)\mathbf{n}$ favours a non-zero director when the local filament density is greater than the Onsager value c_*. In order to ensure $|\mathbf{n}|^{\mathbf{2}} \to \mathbf{1}$ when $c \gg c_*$, we choose the form $\alpha(c) = \nu(c/c_* - 1)$ and $\beta(c) = \nu(1 + c/c_*)$.

From force balance the active stress term follows,

$$\Gamma\mathbf{v} = \vec{\nabla}\cdot\sigma^a \tag{1.6}$$

Then we insert $\mathbf{v} \propto \vec{\nabla}\rho$ in the filament and motor current. The simplified final equations are then

$$\begin{aligned}
\frac{\partial c}{\partial t} &= -\vec{\nabla}\cdot(-D_f\vec{\nabla}c + v_0 c\mathbf{n} - Wc\vec{\nabla}\rho)\\
\frac{\partial \rho}{\partial t} &= -\vec{\nabla}\cdot(-D_m\vec{\nabla}\rho + v_0\rho\mathbf{n}) + k_{bind}(c) - k_u\rho\\
\frac{\partial \mathbf{n}}{\partial t} &+ \lambda(\mathbf{n}\cdot\vec{\nabla})\mathbf{n} = K\nabla^2\mathbf{n} + K_2\vec{\nabla}(\vec{\nabla}\cdot\mathbf{n}) - \xi_0\vec{\nabla}c + \xi\vec{\nabla}\rho + (\alpha(c) - \beta(c)n^2)\mathbf{n}
\end{aligned} \tag{1.7}$$

The results of this hydrodynamic description of polar fluid with motor activity are summarised in the phase diagram in Figure 1.10. To distinguish between these structures and construct the phase diagram the quantities have been measured are following: polarity ($|\langle c\mathbf{n}\rangle|$), divergence ($\langle c\vec{\nabla}\cdot\mathbf{n}\rangle$), curl ($\langle c\vec{\nabla}\cdot\mathbf{n}\rangle$), and filament current (J_f). The following phases: mobile virtual defects, rotating spiral defects, or stationary asters, emerge spontaneously from an interplay between elastic, and active stresses.

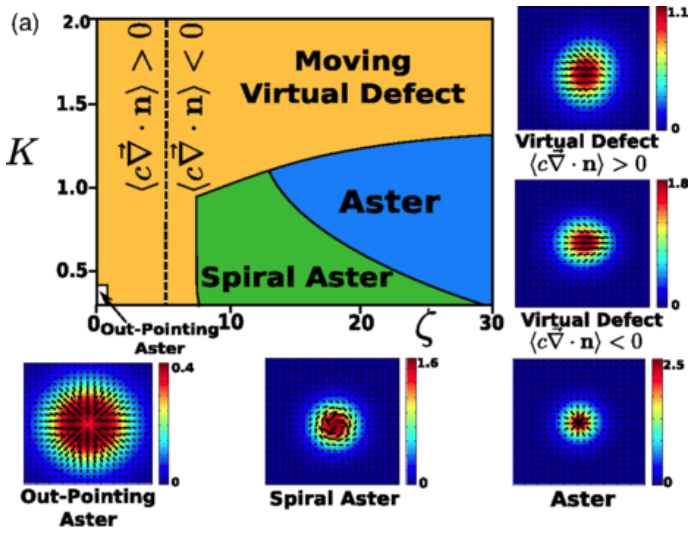

Figure 1.10 (a) The spontaneously emerging patterns in the elastic constant (K) and active contractility (ξ) plane for a fixed concentration of filaments. The filament orientation pattern shows virtual defects, aster, spiral aster, out-pointing aster patterns. The heat map represents filament density (c) and the arrows represent $c\mathbf{n}$ (Image courtesy: [46]).

In the active composite model, the coupling of the membrane to actin configurations is expected to affect the dynamics and organization of the membrane components. Let us now consider a membrane species described, in a coarse-grained sense, by a scalar density field $\rho_s(\mathbf{r}, t)$. In the case of a passive advective scalar, we can write [21]:

$$\frac{\partial \rho_s}{\partial t} = -\vec{\nabla} \cdot (-(1-\phi) D \vec{\nabla} \rho_s + \phi \rho_s \mathbf{v}_0) \tag{1.8}$$

where membrane molecules stochastically bind (unbind) onto the dynamic actin filaments with rates $k_{on}(k_{off})$, respectively. This stochastic binding-unbinding is characterized by a multiplicative noise ϕ with the duty ratio (mean bound time) $K_d = k_{on}c/k_{on}c + k_{off}$ and a switching time $t_{sw} = 2/(k_{on}c + k_{off})$, in which c is the local concentration and v_0 velocity of actin filaments, and D is the diffusion coefficient of the membrane molecules.

This continuum model predicts the clustering of molecules, actively driven by their binding to the polar filaments. The number fluctuations for membrane molecules are enormous; this anomalous fluctuation scales as $\Delta N \sim N^{0.8} > N^{0.5}$. The number

density probability distribution shows a non-Gaussian, slowly decaying exponential tail. This predictions has been verified by fluorescence based experiments in cell [12, 21, 22]. Much of these behaviours were recapitulated in an *in vitro* experiment [44].

1.4 In-vitro realization

A minimal *in vitro* system [44] comprising a thin layer of short actin filaments and Myosin-II minifilaments, ATP on a supported bilayer recapitulate the behaviour predicted by the continuum hydrodynamics model. The orientational patterns of the filaments goes from bundle to apolar to polar aster as one reduce the filament density. In the apolar aster configuration, all the filaments are oriented with their

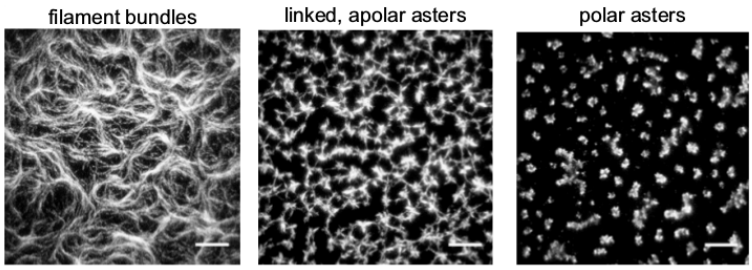

Figure 1.11 The images of actin filaments due to myosin activity. As one reduce filament density the orientational patterns of the filaments goes from bundle to apolar to polar aster (Image courtesy: [44]).

plus (barbed) ends facing inward, toward the core of the aster, while (minus) pointed ends face outward. The localization of fluorescently labelled capping protein(CP) demonstrated this polar nature of the actin asters because capping protein binds only at the plus end of the actin filament. Myosin density is also concentrated in the central region. The rings of capping protein in the central region is the hallmark of myosin-driven polarity sorting and filament organization.

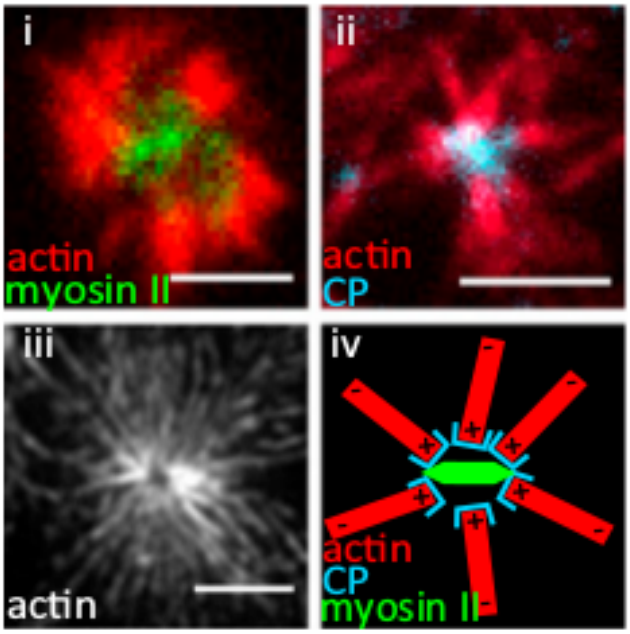

Figure 1.12 High concentration of fluorescently labeled myosin (shown in green) and capping protein (shown in cyan) in the central region of the aster has been shown. Radial array like distribution of actin filament is shown in red (Image courtesy: [44]).

These orientational patterns appear due to contractile flows generated by the myosin minifil [44]ament once ATP is added in the system. With time as the ATP hydrolyses and runs out, the configurations get jammed. But in the cell, the system is in an active steady-state, the configurations form transiently, breakup. The continuum theory predicts in order to get a nonequilibrium steady state where the asters will break up and reform, one needs to allow turnover of filaments. This nonequilibrium steady state is obtained in an in-vitro system with a continuous supply of ATP. The theory prediction for non-gaussian density distribution and anomalous number fluctuation of molecules that can bind to actin is recapitulated in the in-vitro experiment. An active steady-state and recapitulation of theoretical predictions can only happen if the actomyosin in the system is allowed to turnover. The mechanism of the turnover in the system is still not clearly known.

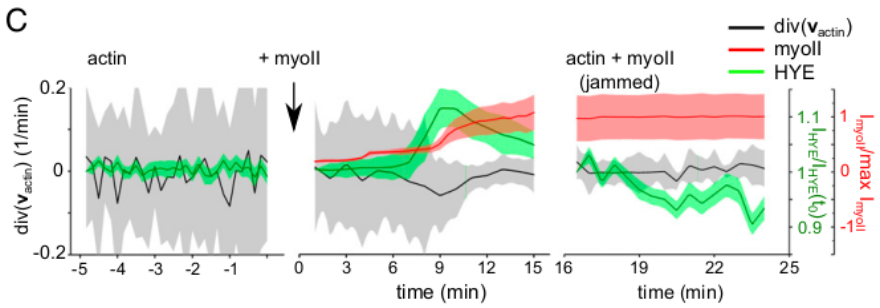

Figure 1.13 Divergence calculation of the velocity filed (black) of filaments shows the system gets jammed after few minute of myosin activity when the ATP in the system runs out (Image courtesy: [44]).

1.5 What this thesis is about

In this thesis, we have studied the effect of nonequilibrium dynamics of the actomyosin cortex on the actin-binding membrane molecules. The Actomyosin cortex can be thought of as an active fluid or elastic meshwork depending on actin type, size, density, crosslinkers density and turnover rate. The formin nucleated dynamic filament in the dilute or semi-dilute limit behaves like a fluid. This fluid description could be valid when the crosslinker density is low, and the turnover of crosslinkers is fast. The continuum hydrodynamics description of this active fluid correctly predicts anomalous statistics of nanoclusters and density correlations, and these behaviours are recapitulated in in-vitro experiments. It is apparent from the observation of experiments and simulations that in order to maintain an active steady-state activity and turnover in the actomyosin cortex must be taken into account. It is also clear that multiple actin binding site of myosin minifilament allows them to drive many dynamic actin filaments towards formation of different orientational patterns. However, this myosin minifilament is a big structure consisting of 30-50 myosin heads. If minifilaments were to drive the observed active nanoclustering of membrane proteins, then one might worry whether steric constraints imposed by these bulky structures could frustrate clustering? A recent study involving agent-based simulations and in vitro reconstitution experiments showed that stratification of the components of the cortical machinery, with Myosin-II, layered atop a layer of dynamic actin which in turn adjoins the membrane, resolves this potential conflict. Stratifi-

cation can overcome the steric frustration due to the Myosin-II minifilaments. This stratified organisation could allow myosin minifilament, which has multiple actin-binding sites, to drive contractile flows that draw in the dynamic actin filaments together in an aster like pattern.

In chapter 2, we develop a coarse-grained agent-based Brownian dynamics simulation techniques that incorporates the effects of stratification, the binding of myosin minifilaments to multiple actin filaments and their turnover. The orientational patterns generated by the actin filaments driven by myosin-II minifilament are isotropic, polar bundle, polar aster, aster, spiral aster.

In chapter 3, we have studied the effect of isotropic phase on the dynamics of membrane molecules. In the dilute limit when the overlap of filament is negligible the multivalency effect of minifilament is negligible. This gives rise to the isotropic pattering of dynamic actin filaments. We have found anomalous transport properties of membrane molecule coupled to this isotropic active fluid.

In chapter 4, we have studied the effect of aster phase on the dynamics of membrane molecules. In the semi dilute limit, we have shown that activity, stratification, multivalency and turnover - are crucial to the attainment of a nonequilibrium steady state characterised by contractile flows and dynamic orientational patterning. This active, steady-state enabled by the aforementioned features of the cortex can facilitate multi-particle encounters of membrane proteins that profoundly influence the kinetics of bimolecular reactions at the cell surface.

On the other hand, ARP2/3 nucleated branched actin filament form elastic meshwork at high actin filament density and crosslinkers density. In chapter 5, we have studied the effect of actin meshwork on the dynamics of membrane molecules. High-speed single-particle tracking experiments with 25 μs time resolution camera shows membrane molecules undergo short-term confined diffusion within a compartment and long-term hop-diffusion between compartments[31, 32, 33, 34, 35]. The diffusion constant of membrane molecules in the cell is $20 - 50$ folds lesser than that seen in an artificial membrane [31]. These observations from the single-particle tracking of molecules on the cell membrane reveal a cage-hopping behaviour due to cortical actin meshwork. A similar cage-hopping dynamics is observed in particle transport studies of a dense fluid approaching glass transition. These resemblance has motivated us to study the underlying physics of cage-hopping transport in the

vicinity of a random field-glass induced by the quenched random disposition of the cortical actin meshwork. We study the transport and approach to a new kind of glass using a agent-based Brownian dynamics simulations. Here we show that the actin mesh adjoining the cell membrane acts as a random line pinning that drives it towards a dynamically arrested state at physiological temperatures. This novel random pinning model on molecular transport is quite distinct from the random pinning potentials studied in the glass literature. Here, the effects of topological confinement become significant, which is captured in the different two point correlation functions and dynamical heterogeneity. We have studied the influence of actin meshwork on the phase segregation of a binary glassy mixture.

References

[1] J. T. Hancock, Cell Signalling (2nd Ed.), Oxford University Press, New York (2005).

[2] J. F. Hancock, Nature reviews Molecular cell biology **4**, 373 (2003).

[3] B. N. Kholodenko, W. Kolch, Cell **4**, 133 (2008).

[4] B.N. Kholodenko, Nat. Rev. Mol. Cell Biol. **7**, 165-176 (2006).

[5] S. J. Singer, Garth L. Nicolson, Science, **175**, (1972).

[6] K. Simons and E. Ikonen, Nature, **387**, 6633, (1997).

[7] Ipsen, J. H., Karlström, G., Mouritsen, O. G., Wennerström, H., and Zuckermann, M. J., Biochim. Biophys. Acta 905, 162–172 (1987).

[8] T. Baumgart, A. T. Hammond, P. Sengupta, S. T. Hess, D. A. Holowka, B. A. Baird,and W. W. Webb, Proceedings of the National Academy of Sciences **104**, 3165 (2007).

[9] Veatch, S. L., Cicuta, P., Sengupta, P., Honerkamp-Smith, A., Holowka, D., and Baird, B., ACS Chem. Biol. **3**, 287–293 (2008).

[10] J. Zhao, J. Wu, F.A. Heberle, T.T. Mills, P. Klawitter, G. Huang, G. Costanza, G.W. Feigenson, Biochim. Biophys. Acta, **1768** (2007).

[11] R. Varma, and S. Mayor, Nature **394**, 798–801, (1998).

[12] P. Sharma, R. Varma, R. Sarasij, K. Gousset, G. Krishnamoorthy, M. Rao, S. Mayor, et al., Cell **116**, 577 (2004).

[13] M. Rao and S. Mayor, Current opinion in cell biology **29**, 126 (2014).

[14] T. S. van Zanten, A. Cambi, M. Koopman, B. Joosten, C. G. Figdor and M. F. G. Parajo, **106** (2009).

[15] P. Sengupta, T. Jovanovic-Talisman, D. Skoko, M. Renz, S. L. Veatch and J. Lippincott-Schwartz, Nature, **8**, 969 (2011).

[16] Eggeling, C., Ringemann, C., Medda, R., Schwarzmann, G., Sandhoff, K., Polyakova, S., Belov, V. N., Hein, B., von Middendorff, C., Schönle, A. et al. Nature **457**, 1159-1162 (2009).

[17] W. W. Schamel and B. Alarcon, Immunol. Rev. **251**, 13–20 (2013).

[18] Cebecauer, M., Spitaler, M., Sergé, A. and Magee, A. I., J. Cell Sci. **123**, 309-320 (2010.)

[19] Murakoshi, H., Iino, R., Kobayashi, T., Fujiwara, T., Ohshima, C., Yoshimura, A. and Kusumi, A., Proc. Natl. Acad. Sci. USA 101, 7317-7322 (2004).

[20] D. Goswami, K. Gowrishankar, S. Bilgrami, S. Ghosh, R. Raghupathy, R. Chadda, R. Vishwakarma, M. Rao, and S. Mayor, Cell **135**, 1085 (2008).

[21] K. Gowrishankar, S. Ghosh, S. Saha, C. Rumamol, S. Mayor, and M. Rao, Cell **149**, 1353 (2012).

[22] S. Saha, I.-H. Lee, A. Polley, J. T. Groves, M. Rao, and S. Mayor, Molecular biology of the cell **26**, 4033 (2015).

[23] S. J. Plowman, C. Muncke, R. G. Parton, and J. F. Hancock, Proceedings of the National Academy of Sciences **102**, 15500 (2005).

[24] D. Lingwood and K. Simons, science **327**, 46 (2010).

[25] K. Gowrishankar and M. Rao, Soft Matter **12**, 2040-2046 (2016).

[26] P. Chugh, A. G. Clark, M. B. Smith, D. A. Cassani, K. Dierkes, A. Ragab, P. P. Roux, G. Charras, G. Salbreux, and E. K. Paluch, Nature cell biology **19**, 689 (2017).

[27] B. Alberts, A. Johnson, J. Lewis, M. Raff, K. Roberts and P. Walter, 'Molecular Biology of the Cell', 5 th edition (2007).

[28] C. P. Broedersz and F. C. MacKintosh, Reviews of Modern Physics, **86**, (2014).

[29] G Salbreux,G Charras, E Paluch, Trends Cell Biol,**22**, 536-545 (2012).

[30] Kasza, K. E., G. H. Koenderink, Y. C. Lin, C. P. Broedersz, W. Messner, F. Nakamura, T. P. Stossel, F. C. MacKintosh, and D. A. Weitz, Phys. Rev. E **79**, (2009).

[31] T. Fujiwara, K. Ritchie, H. Murakoshi, K. Jacobson and A. Kusumi, J. Cell Biol. **157**, 904 (2002).

[32] Murase, K., T. Fujiwara, Y. Umemura, K. Suzuki, R. Iino, H. Yamashita, M. Saito, H. Murakoshi, K. Ritchie and A. Kusumi, Biophys. J. **86** 4075 (2004).

[33] Y. M. Umemura, M Vrljic, S. Y. Nishimura, T. K. Fujiwara, K. G. N. Suzuki and Akihiro Kusumi, Biophysical Journal **95**, 435 (2008).

[34] A. Kusumi, T. K. Fujiwara, R. Chadda, M. Xie, T. A. Tsunoyama, Z. Kalay, R. S. Kasai, K. G. N. Suzuki, Annu. Rev. Cell Dev. Biol. **28** 215-50 (2012).

[35] Kusumi A, Tsunoyama T A, Hirosawa K M, Kasai R S and Fujiwara T K, Nature Chemical Biology **10**, 524–32 (2014).

[36] N. Morone, T. Fujiwara, K. Murase, R. S. Kasai, H. Ike, S. Yuasa, J. Usukura, and A. Kusumi, The Journal of cell biology **174**, 851 (2006).

[37] MBINFO lecture.

[38] G. H. Koenderink and E. K. Paluch, Current opinion in cell biology **50**, 79 (2018).

[39] S. L. Freedman, S. Banerjee, G. M. Hocky and A. R. Dinner, Biophys. J. 113, 448-460 (2017).

[40] M. Lenz, T. Thoresen, M. L. Gardel and A. R. Dinner, Phys. Rev. Lett. 108, 238107 (2012).

[41] M. P. Murrell and M. L. Gardel, Proc. Natl. Acad. Sci. USA 109, 20820-20825 (2012).

[42] K. Kruse and F. Jülicher, Phys. Rev. Lett. 85, 1778-1781 (2000).

[43] A. Zumdieck, K. Kruse, H. Bringmann,A. A. Hyman and F. Jülicher, PLoS ONE 2, e696 (2007).

[44] D. V. Köster, K. Husain, E. Iljazi, A. Bhat, P. Bieling, R. D. Mullins, M. Rao, and S. Mayor, Proceedings of the National Academy of Sciences **113**, E1645 (2016).

[45] W. Luo, C.-H. Yu, Z. Z. Lieu, J. Allard, A. Mogilner, M. P. Sheetz and A. D. Bershadsky, J. Cell Biol. 202, 1057-1073 (2013).

[46] K. Husain and M. Rao, Physical review letters **118**, 078104 (2017).

[47] K. Husain, *The Mechanics of Cell Surface Clusters and their role in Signalling*, Ph.D Thesis, National Centre for Biological Sciences (Tata Institute of Fundamental Research, November 2017).

[48] M. C. Marchetti, J. F. Joanny, S. Ramaswamy, T. B. Liverpool, J. Prost, M. Rao and R. A. Simha, Rev. Mod. Phys. **85**, 1143 (2013).

[49] S. Ramaswamy, Annu. Rev. Condens. Matter Phys. bf 1, 323–345 (2010).

End of Chapter

Chapter 2

Stratified organization of the actomyosin cortex and steady active contractile flows

2.1 Introduction

Actomyosin cortex plays pivotal role in different dynamic processes in cell such as cell division, migration, shape change etc.. This thin layer beneath the membrane is primarily built from two ingredients: the actin cytoskeleton and myosin motors. The actin cytoskeleton is composed simultaneously of dynamic linear polar filaments, nucleated by Formin [1, 2, 3] and an extensively branched, relatively static meshwork nucleated by Arp2/3 [4, 5, 6]. Importantly, this thin structure can generate active stresses at the membrane which affact local composition and membrane shape [7]. This active stress emerges from the interaction of the myosin motor with the actin filament. Myosin motors use the energy of ATP hydrolysis in this process. These motors assemble into bipolar filaments with motor-heads on the two ends and work together as a team, known as myosin minifilament. This minifilament interact with the actin filament in different ways. Due to this bipolar nature, myosin filaments can slide anti-parallel actin filaments in opposing directions. The directional movement of motors along actin leads to this polarity sorting. This process generates flow in the actomyosin cortex and eventually, it contracts.

Thus membrane proteins that bind to cortical actin are driven by this actomyosin contractility[1, 8, 9, 10, 11]. The major component of Myosin motors, is nonmuscle myosin-II, which assemble as large minifilaments consisting of $\sim 30 - 50$ myosin heads [12, 13]. If myosin-II minifilaments are to drive the observed active nanoclus-

tering of membrane proteins [1, 8, 9, 10, 11, 14], then one might worry whether steric constraints imposed by these bulky structures could frustrate clustering? A recent study, involving agent-based simulations and *in vitro* reconstitution experiments, showed that *stratification* of the components of the cortical machinery, with myosin-II layered atop a layer of dynamic actin which in turn adjoins the membrane, resolves this potential conflict [15, 16]. Stratification can circumvent the steric frustration due to myosin-II minifilaments and can drive contractile flows that draw in the dynamic actin filaments together to form a variety of orientational patterns including asters [16].

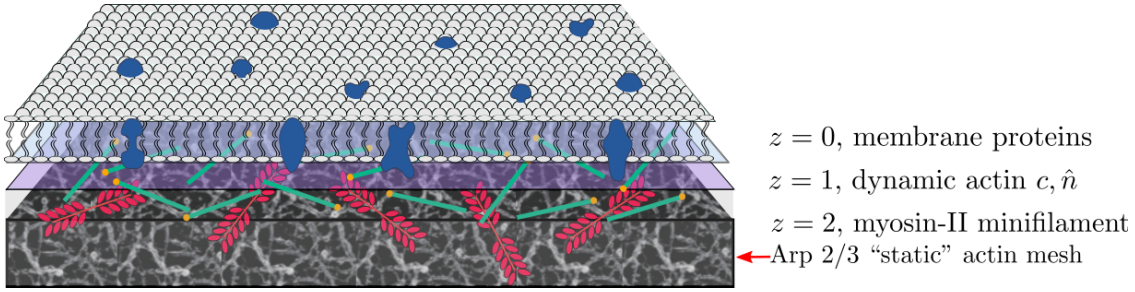

Figure 2.1 Schematic of the cell surface as a stratified active composite of the multicomponent bilayer membrane ($z = 0$), the thin layer of dynamic linear actin filaments ($z = 1$) and a layer of myosin-II minifilaments ($z = 2$) atop a dense Arp2/3 crosslinked actin mesh (image of actin mesh modified from [17]). The myosin-II minifilaments (red) bind to actin filaments (green) in $z = 1$ and apply active forces and torques. In turn, the actin filaments bind to transmembrane proteins (blue) in $z = 0$ and drive contractile flows leading to dynamic clustering of the proteins. The + end of actin filaments is depicted by orange dots.

The aster-like orientational patterning of actin filaments and nanoclustering of membrane proteins are dynamic in the *in vivo* situation, and are maintained in a nonequilibrium steady state by steady active contractile flows [14, 8, 1, 19, 30, 18, 20]. This is in contrast to most *in vitro* reconstitution system, in which the contractile actomyosin's orientation patterns get jammed and consequently the protein clusters, once formed, disperse and diffuse away [15, 23, 21, 22]. In order to *maintain* a nonequilibrium steady state characterised by steady active contractile flows, dynamic orientational patterning and dynamic protein clustering, one needs in addition to the stratification of the active machinery, a constant *turnover* of active components [18, 25, 24, 26], that give rise to a dynamic force patterning. This has been

realised in two recent *in vitro* studies that employ a continuous ATP regenerating system [15, 25, 26]. The multivalency and turnover of active components give rise to an activation and inhibition of local stresses, a crucial ingredient for the attainment of the nonequilibrium steady state [28, 19, 30, 27, 24, 26, 25, 29].

Here we have done agent-based computer simulation of autonomous agents (individual molecules or collective molecular ensembles) and their activities and interactions. The actin filaments are modelled as stiff rods composed of beads. We have not explicitly included the myosin minifilament in our simulation. The active force and torque induced by minifilament on the actin filament have been realised through the interaction between the actin filament. In a simple coarse-grained agent based simulation, we bring together all the ingredients necessary for observing the nonequilibrium steady state, viz., stratification, turnover and multivalency of force generators. We do this without having to explicitly include a structural model for the molecular force generators. It would have made simulation exceedingly difficult to monitor long time dynamics. Thus our coarse grained simulation method while not explicitly incorporating myosin minifilaments, it takes into account its effect on *currents*, *forces* and *torques* applied to single and multiple actin filaments. Indeed we show that inhibition of any one of the three ingredients, leads to a loss of the desired phenotype. The multivalency and turnover of active components give rise to an activation and inhibition of local stresses, a crucial ingredient for the attainment of the nonequilibrium steady state [28, 19, 30, 27, 24, 26, 25, 29]. The nonequilibrium steady states observed both *in vivo* and in properly designed reconstitution experiments are recapitulated by this simple coarse grained model, which incorporates the fluctuating active forces and torques in a stratified geometry. We observe different orientational patterns by altering the active stresses.

2.2 Dynamics of actin filaments in a stratified cortex

Our coarse-grained simulation incorporates the three ingredients crucial to the active composite - stratification of the actomyosin cortex suggested by [16], multivalency of myosin-II minifilaments and turnover of the active components, and the way they

influence the dynamics of proteins that reside on the plasma membrane. To this end, we describe coarse-grained agents (see Fig. 2.1) along three different two-dimensional layers (strata) labelled $z = 0$ (membrane), $z = 1$ (dynamic formin-nucleated actin filament layer), and $z = 2$ (myosin minifilament layer). The multivalent myosin minifilaments at $z = 2$, stochastically bind and unbind onto (possibly multiple) dynamic actin filaments at $z = 1$; when bound they generate active forces and torques on the filaments.

The dynamics of the actin filaments take place in the layer $z = 1$. Since the linear formin-nucleated actin filaments are much shorter than the persistence length ℓ_p, we will treat them as rigid rods of length l and diameter b, with $l \gg b$. Our agent based update rules for the dynamics of actin filaments are motivated by the following - in the limit of *dilute* concentration of actin filaments, we can define $c(\mathbf{r}, \hat{\mathbf{n}}, t)$ as the single filament distribution function of actin filaments of centre-of-mass position $\mathbf{r} = (x, y)$ and polar orientation $\hat{\mathbf{n}} = (\cos\theta, \sin\theta)$, which obeys the Smoluchowski equation [31, 32],

$$\partial_t c(\mathbf{r}, \hat{\mathbf{n}}, t) = -\nabla \cdot \mathbf{J} - \mathcal{R} \cdot \mathcal{J} \tag{2.1}$$

where $\mathcal{R} = \hat{\mathbf{n}} \times \partial_{\hat{\mathbf{n}}}$ is the rotational operator.

The translational and rotational currents $\mathbf{J}$ and $\mathcal{J}$, respectively, have contributions from interactions primarily excluded volume, thermal diffusion, and myosin activity, and are proportional to the translational and rotational velocities of the rigid filaments.

To implement this idea in the agent based simulation, we need to relate the centre of mass velocity of the filament $\mathbf{v}_i$ and the rotational velocity ω_i of the corresponding forces and torques acting on the filament.

Decomposing the centre-of-mass velocity of the filament i as, $\mathbf{v}_i = v_{\parallel,i}\hat{\mathbf{n}}_i + v_{\perp,i}\hat{\mathbf{m}}_i$, where $\hat{\mathbf{m}}_i$ is perpendicular to $\hat{\mathbf{n}}_i$, we have,

$$\begin{aligned}
v_{i,\parallel}(t) &= \frac{1}{\gamma_\parallel}\left(\sum_{j\neq i}\mathbf{F}^a_{ij,\parallel} + \xi_\parallel\hat{\mathbf{n}}_i + \mathbf{F}_1 + \mathbf{F}_{2,\parallel} + \mathbf{F}_{3,\parallel}\right)\\
v_{i,\perp}(t) &= \frac{1}{\gamma_\perp}\left(\sum_{j\neq i}\mathbf{F}^a_{ij,\perp} + \xi_\perp\hat{\mathbf{m}}_i + \mathbf{F}_{2,\perp} + \mathbf{F}_{3,\perp}\right)\\
\omega_i(t) &= \frac{1}{\gamma_r}\left(\sum_{j\neq i}\mathbf{M}^a_{ij,r} + \xi_r + \mathbf{M}_2 + \mathbf{M}_3\right)
\end{aligned} \tag{2.2}$$

where $\mathbf{F}_{ij}$ and $\mathbf{M}_{ij}$ are the passive contributions to the force and torque on the actin filament i from filament j, $\xi_\parallel$, $\xi_\perp$ and ξ_r are the corresponding contributions from thermal noise [33], and $\mathbf{F}_1, \ldots, \mathbf{M}_3$ are the purely active contributions induced by myosin-II minifilaments. The friction coefficients are given by $\gamma_\parallel = \gamma_a l$, $\gamma_\perp = 2\gamma_\parallel$ and $\gamma_r = \gamma_\parallel l^2/6$ [34, 35]. All noises are drawn from independent Gaussian distributions with zero mean and variance $= 2k_BT\gamma_k/\Delta t$, where $k \equiv \parallel, \perp$ or r. We use Eq. 2.2 to update the centre-of-mass position and orientation of the i-th filament in our Brownian dynamics simulation [33].

The actin filaments are modeled using beads, the passive contributions to the forces and torques on filament i from filament j, $\mathbf{F}^a_{ij}$ and $\mathbf{M}^a_{ij}$, are calculated from the bead-bead interaction potential,

$$\begin{aligned} V_{ij}(r) &= \sum_{m,m'=1}^{N_b} 4\epsilon_a \left(\frac{b^2}{|\mathbf{r}_{im} - \mathbf{r}_{jm'}|^2 + \delta^2} \right)^6 + V_0' + V_2' \, |\mathbf{r}_{im} - \mathbf{r}_{jm'}|^2 \qquad \text{for } |\mathbf{r}_{im} - \mathbf{r}_{jm'}| \le b \\ &= 0 \qquad \text{for } |\mathbf{r}_{im} - \mathbf{r}_{jm'}| > b \end{aligned} \tag{2.3}$$

where $|\mathbf{r}_{im} - \mathbf{r}_{jm'}|$ is the distance between the m-th bead of i-th filament and m'-th bead of j-th filament and values of constants V_0' and V_2', are chosen so that the potential and force are continuous at cutoff $r = b$. Here we set the filament bead size $b = 1.6\sigma$, and the potential parameters $\epsilon_a = 1$ and $\delta = 0.8$, in units of ϵ and σ, respectively. With this choice of parameters, an actin filament composed of $N_b = 15$ beads, has a mean equilibrium length $l = 24\sigma$.

Finally, we describe the form of the active contributions to the forces and torques that arise from the interaction of Myosin-II minifilaments in $z = 2$ with actin filaments in $z = 1$. These active forces and torques can only be propagated if some of the myosin heads of the multivalent myosin filament bind and hold on to the dense Arp 2/3 static meshwork below it (Fig. 2.1). Now instead of explicitly including a structural model for the bulky Myosin-II minifilaments, we will simply incorporate the many-body contributions to the active forces and torques coming from Myosin-II minifilaments, using a carefully chosen system of extensional and torsional springs, Fig. 2.2. We list the contributions to the active translational and rotational currents that enter Eq. 2.2.

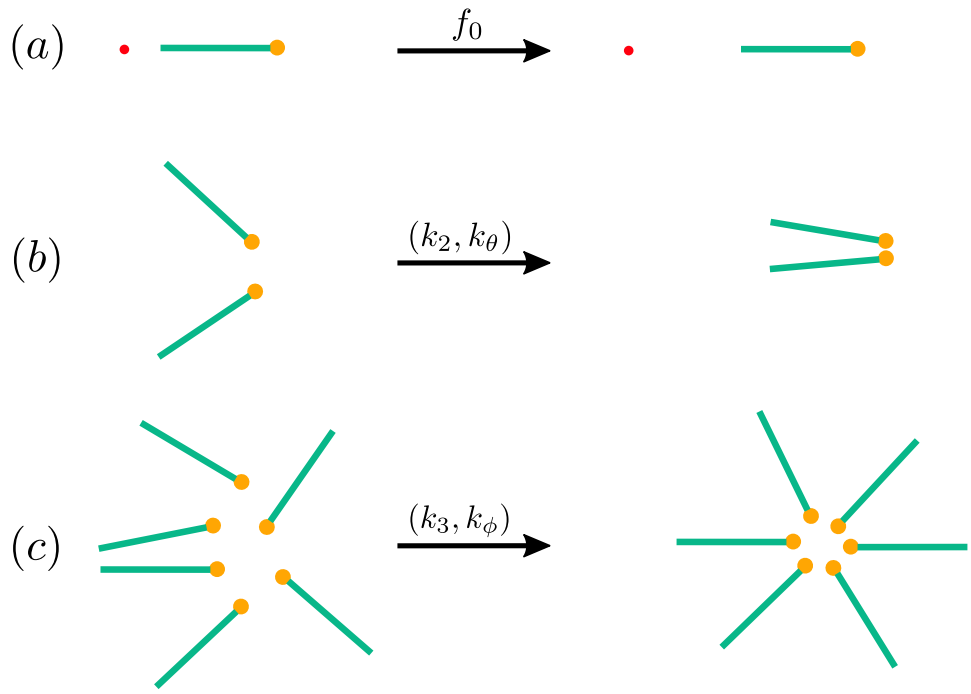

Figure 2.2 Schematic showing the consequences of the active forces and torques induced by Myo-II minifilament on dynamic actin filaments realised in terms of propulsion force and extensional and torsional springs. (a) Single filament contribution: Myosin driven active current $v_0\hat{\mathbf{n}}$ along the filament orientation pointing to the + end (orange dot), leading to propulsion away from the reference red dot. (b) Two filament contribution: Myosin driven forces and torques bring together and align two filaments leading to *bundling*. This is realised by having an extensional spring (k_2) and torsional spring (k_θ) between the filaments. (c) Multiple filament contribution: Myosin driven forces and torques bring together and reorient multiple filaments leading to the formation of an *aster*. This is realised by having extensional springs (k_3) and torsional springs (k_ϕ) between pairs of filaments.

1. Single filament contribution

   Referring to Eq. 2.2, $\mathbf{F}_1 = f_0\hat{\mathbf{n}}$ is the single filament contribution to the active force driven by a myosin minifilament, where a few myosin heads are attached to the filament and the heads at the other bipolar end of the myosin minifilament are attached to the static actin meshwork. This leads to an active translation current $\propto v_0\hat{\mathbf{n}}$, of magnitude $v_0 = f_0/\gamma_\parallel$ along its polar orientation $\hat{\mathbf{n}}$ (pointing towards the + end of the filament, see Fig. 2.2a). In principle, an isolated actin filament can also contribute to an active rotational current. We will however assume that the active orientational decorrelation time τ_a is

larger than the rotational diffusion time τ_r of thermal origin or collision time τ_c with other filaments. With the filament concentration and filament length under consideration, we have $\tau_c < \tau_r \ll \tau_a$, and thus the late-time diffusion coefficient of a single actin filament is set by $D_a = \frac{1}{2} v_0^2 \tau_c$.

2. Two filament contribution

   A myosin minifilament whose heads attach to two dynamic actin filaments at $z = 1$ at one end and to the static actin meshwork at the other end, induces contractile flows that lead to bundling and polar alignment (Fig. 2.2b). By a polarity sorting mechanism [15, 36], this brings the + ends of the dynamic actin filaments together (see Fig. 2.2b). This contributes to the 2-filament active forces and torques, $\mathbf{F}_2$ and $\mathbf{M}_2$, in Eq. 2.2, realised here by having an extensional spring (stiffness k_2) attached to the +ends of the filament pair and a torsional spring (stiffness k_θ), when the filaments are within a cutoff distance (here, taken to be $2l/3$). Since the extensional and torsional spring stiffneses have the same molecular origin, they must be related, dimensional considerations suggest $k_2 = 4k_\theta/l^2$ [31, 32].

3. Three and multiple filament contribution

   Myosin minifilaments whose heads attach to three or more dynamic actin filaments at $z = 1$ at one end and to the static actin meshwork at the other end, induces contractile flows that lead to the formation of bundles and orientational patterns such as asters (Fig. 2.2c). This also involves the polarity sorting mechanism that brings the + ends of the dynamic actin filaments together (Fig. 2.2c). This leads to $\mathbf{F}_3$ and $\mathbf{M}_3$, the 3 (or multiple)-filament contributions to the active forces and torques in Eq. 2.2. This is realised by extensional and torsional springs of stiffness k_3 and k_ϕ, respectively, that operate only when three filaments or more are within a cutoff distance $2l/3$ of each other. The torsional spring has a rest angle equal to π/n, where n is the number of actin filaments involved. As before, dimensional considerations suggest $k_3 = 4k_\phi/l^2$ [31, 32]. Note that the salient effects of multivalency of the Myo-II minifilaments appear via these multifilament contributions; thus in our simulations we can turn off the effects of multivalency by simply setting

$$k_3 = k_\phi = 0.$$

Turnover of dynamic actin filaments and myosin: Apart from stratification and multivalency, the other critical feature that we need to include is the turnover of the actomyosin machinery. The microscopic physics of turnover of myosin minifilaments and dynamic actin is subtle and involves many distinct molecular mechanisms, such as cooperative unbinding-rebinding of myosin heads and actin filaments, fragmentation of actin filaments by enzymes such as cofilin, depolymerisation, nucleation and recruitment [19, 30, 27, 24, 25, 37, 29]. Turnover releases the buildup of stresses generated by contractile flows and consequent jamming of actin and myosin minifilaments, and aspect that is necessary for the maintenance of the nonequilibrium steady state. In our coarse-grained simulation we simply implement turnover by removing actin filaments with a rate k_r, modelled as a Poisson process. We ensure that in the process, the mean number of actin filaments is held fixed, so that when a filament is removed, we introduce another in a random spatial location with random orientation. We have varied k_r over the range $10^{-4} - 10^{-1}$, in simulation units.

Before we end this section, we wish to emphasize the simplicity of our coarse-grained agent based simulation - it incorporates the minimal features necessary for observing the nonequilibrium steady state, viz., stratification, turnover and multivalency of active force generators, without explicitly including the structural aspects of the bulky myosin-II minifilaments. It does so by taking into account its effect on *currents*, *forces* and *torques* applied to single and multiple actin filaments; indeed we show that abrogation of any one of the three features, leads to a loss of the desired phenotype. This also opens the possibility of extending the study to different physical situations like clustering, chemical kinetics of membrane molecules as we discuss in chapter 4.

2.3 Simulation details

With the forces and torques in place, we numerically integrate the Brownian dynamics equations updating the position and orientation of actin filaments (Eq. 2.2) using a velocity Verlet integration scheme with an integration time step $\Delta t \sim 2 \times 10^{-3}$.

Total run time of the Brownian dynamics simulation is $t = 5 \times 10^4$. In our simulations runs we have taken number of filaments $N_a = 64$ and system size $L = 400$, so that we are in the dilute filament regime. We take single filament velocity $v_0 = 0.2$ coming from the active translation current. Our initial conditions are chosen from a thermal distribution at temperature $T = 1.0$, and all results presented here are averaged over 32 such independent initial realisations. Throughout our simulation, the units of length, time and energy are set by σ, γ_p and ϵ (Table 2.1). All other parameters expressed in natural units are listed in Table. 2.2 for convenience.

Table 2.1 Natural units - simulation units (S.U.) and real units (R.U.)

Natural Units	Symbol [Dimension]	S.U.	R.U.
Length (Actin monomer)	σ $[l]$	0.8	8 nm
Energy (Inter-actin filament interaction)	ϵ	1	4.11×10^{-21} J
Actin monomer friction coefficient	γ_a	1	0.08 $pN\mu m^{-1}s$
Time	$t = l^2\gamma_a/\epsilon$	1	2×10^{-3} s

Table 2.2 Other parameters expressed in natural units and their ranges

Parameters	Symbol [Dimension]	Value/Range
Physiological Temperature	T $[\epsilon]$	1
Actin filament length	l $[l]$	24
Single actin filament propulsion velocity	v_0 $[lt^{-1}]$	0.2
Torsional spring stiffness	k_θ, k_ϕ $[\epsilon]$	$10^{-1} - 10^3$
Extensional spring stiffness	k_2, k_3 $[\epsilon l^{-2}]$	$10^{-1} - 10^3$
Turnover rate of actin filaments	k_r $[t^{-1}]$	$10^{-1} - 10^{-4}$

2.4 Orientational patterns of actin and the nonequilibrium steady state

We first explore the orientational patterns displayed by the actin filaments in layer, $z = 1$ in the absence of the membrane proteins at $z = 0$ (Fig. 2.1). Recall that we are working in the regime where the overall concentration of the dynamic actin filaments is low, i.e., in the absence of activity, we are in the so-called dilute regime [34]. Despite this, active contractile stresses drive the filaments to form clusters with distinct orientation patterns, as in [15].

We define local coarse-grained fields, the actin filament density

$$c(\mathbf{r}, t) = \sum_i \delta(\mathbf{r} - \mathbf{r}_i(t)) \tag{2.4}$$

and actin filament polar orientation

$$\mathbf{n}(\mathbf{r}, t)\, c(\mathbf{r}, t) = \sum_i \hat{\mathbf{n}}_i(t)\, \delta(\mathbf{r} - \mathbf{r}_i(t)) \tag{2.5}$$

where $\mathbf{r}_i$ and $\hat{\mathbf{n}}_i$ are the centre-of-mass position and polar orientation of the ith filament, respectively. To characterise the orientational patterning, we first note that the contractile flows lead to strong concentration fluctuations which in turn influence the orientation correlations. Because of the strong concentration fluctuations, one cannot use a global orientation order parameter to describe the phases observed in the simulations. To do so, we first compute the coarse-grained filament concentration profile or the concentration correlation function, from which we extract a correlation length. This defines the spatial scale of a "cluster". We compute the net orientation of each cluster, by projecting the orientation of individual filaments belonging to the cluster onto the mean orientation for that cluster. The polar order parameter $\langle P \rangle$ is then defined as an average over all clusters (and a further average over time and independent realisations).

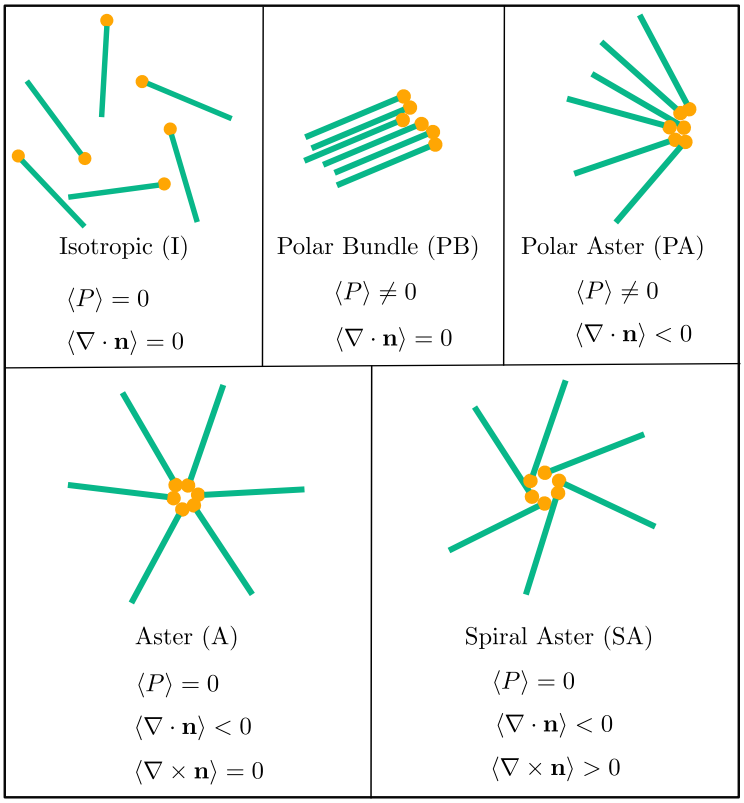

Figure 2.3 Schematic of the orientational patterns generated by the actin filaments driven by myosin-II minifilament are i) isotropic, ii) polar bundle, iii) polar aster, iv) aster, v) spiral aster. Polar order parameter ($\langle P \rangle$) and divergence ($\nabla \cdot \mathbf{n}$) and curl ($\nabla \times \mathbf{n}$) of the coarse-grained orientation has been measured to differentiate the patterns.

We find that the orientation patterns within each cluster, can be described as a polar bundle, an aster or a spiral. To characterise spatially varying orientation patterns, we need to compute the divergence and curl of the coarse-grained orientation field using the following procedure - (i) choose a coarse graining cell $\Omega(\mathbf{r})$ of linear dimension $2\,l$, around an arbitrary point $\mathbf{r}$, (ii) smear the centre of mass of each filament by an exponentially decaying function, an interpolation scheme that allows us to smoothen the vector fields within the cell $\Omega(\mathbf{r})$,

$$\mathbf{n}(\mathbf{r}) = \frac{\sum_{i \in \Omega(\mathbf{r})} \hat{\mathbf{n}} e^{-|\mathbf{r}-\mathbf{r}_i|/\lambda}}{\sum_{i \in \Omega(\mathbf{r})} e^{-|\mathbf{r}-\mathbf{r}_i|/\lambda}} \tag{2.6}$$

where we choose the decay length $\lambda = 3\sigma$. This allows us to cleanly compute the

divergence and the curl of the vector field.

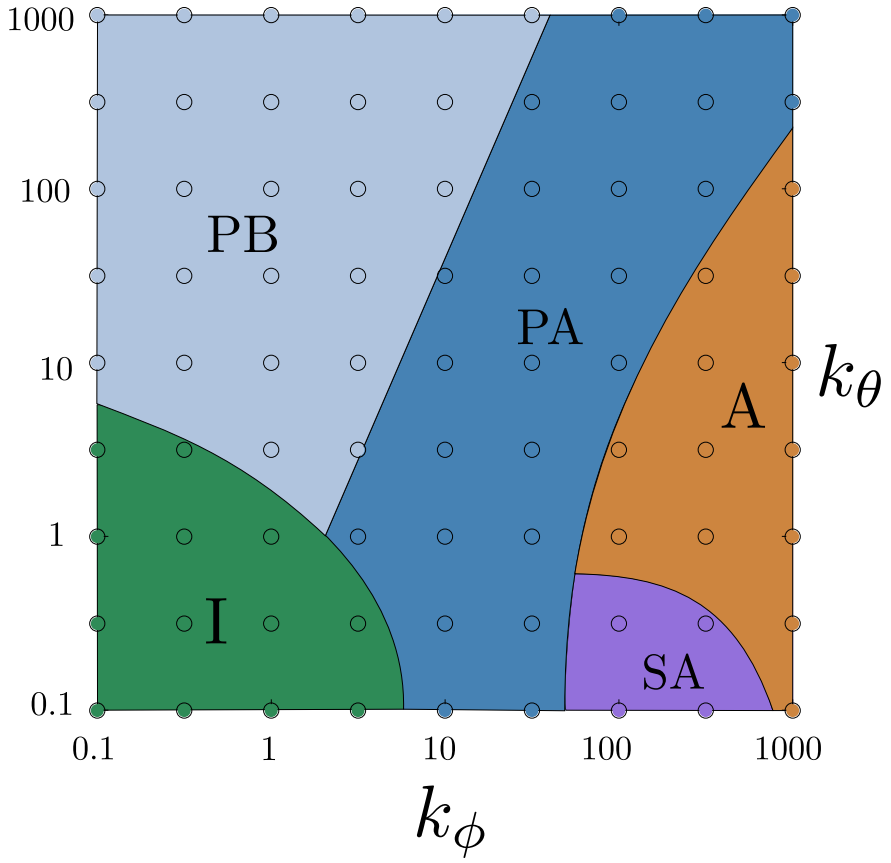

Figure 2.4 Orientational patterns exhibited by polar actin filaments using the Brownian dynamics simulation described in Sect. 2.3. Steady state diagram in the space of two-filament and multifilament contributions to the active torque, here realised as torsional springs, k_θ and k_ϕ shows orientational patterns - Isotropic (I), Polar Bundle (PB), Polar Aster (PA), Aster (A), and Spiral Aster (SA). The circles in the phase diagram depict the points where the simulations were done. The boundaries between the phases were obtained by a interpolation with exponential weights and subsequent smoothening using a cubic spline.

Keeping the overall filament concentration fixed, we vary the stiffness of the torsional springs (k_θ, k_ϕ), that in turn alter the relative contributions of the Myo-II induced active torques. As discussed in Sect. 2.3, since the extensional and torsional springs share a common molecular origin, they are related to each other in a simple manner. From our simulations, we identify five distinct orientational phases - isotropic (I), polar bundle (PB), polar aster (PA), aster (A) and spiral aster (SA) as shown and characterised in Fig. 2.4. The order parameters characterising these

phases are the polar order parameter $\langle P \rangle$, the divergence of the orientation or the splay $\langle \nabla \cdot \mathbf{n} \rangle$ and the curl of the orientation or the vorticity $\langle \nabla \times \mathbf{n} \rangle$. As shown in Fig. 2.4, increasing the 2-filament contribution to the active torque k_θ favours polar bundling, while increasing the multifilament contribution k_θ favours asters. This observation is consistent with our earlier theoretical study using a hydrodynamic approach [38, 39]. As expected, since these orientation patterns are a consequence of the active forces and torques, the polar bundle and polar asters move along the direction set by their mean orientation and the spiral asters rotate, consistent with the predictions of previous studies [40, 38, 39]. The patterns described here have been observed in several *in vitro* reconstitution studies [41, 21, 15, 25].

So far we have included only two ingredients of the active composite, namely stratification and multivalency. In this case, once steady state is reached, the orientational patterns described in Fig. 2.4 remain the same, although some will exhibit a mean translation (I, PB, PA) and others (SA) a mean rotation. Now when we introduce the third ingredient, namely steady turnover of the filaments, these patterns undergo dynamic remodelling. In our simulation, we invoke a stress dependent turnover of actin filaments, which relaxes the build up of local contractile active stress $\sigma_{act} \propto -c\,(\nabla \cdot \mathbf{n})$ [24, 26]. This is consistent with recent *in vitro* studies [15, 25], and with observations of turnover of actomyosin in the context of tissue remodelling [42].

The orientation patterns, such as asters, show intermittent fluctuations as seen in Fig. 2.5(a) - the time series of $\frac{c}{\rho_a}\nabla \cdot \mathbf{n}$ - where ρ_a is the mean number density of filaments, and ranges from -2 (a pure aster with $\mathbf{n} = -\hat{\mathbf{r}}$) to 0. This is reflected in the skewed probability distribution of the net divergence shown in Fig. 2.5(b). Intermittent dynamics of a statistical variable $X(t)$, here $\frac{c}{\rho_a}\nabla \cdot \mathbf{n}$, identified by alternating periods of quiescence and large changes over short times (Fig. 2.5(a)), shows up in the behaviour of the kurtosis, $\kappa(t) = S_4(t)/S_2^2(t)$, the ratio of the fourth central moment and fourth power of the standard deviation of the statistical quantity [43, 44]. Figure 2.5(c), a plot of the kurtosis $\kappa(t)$ versus time, scaled by the turnover rate k_r, shows a power-law divergence as $t \to 0$ - a signature of intermittency characterising the nonequilibrium steady state [44]. These results are entirely consistent with our earlier hydrodynamic theory [1, 38, 45], and recent *in vitro* studies [15, 25].

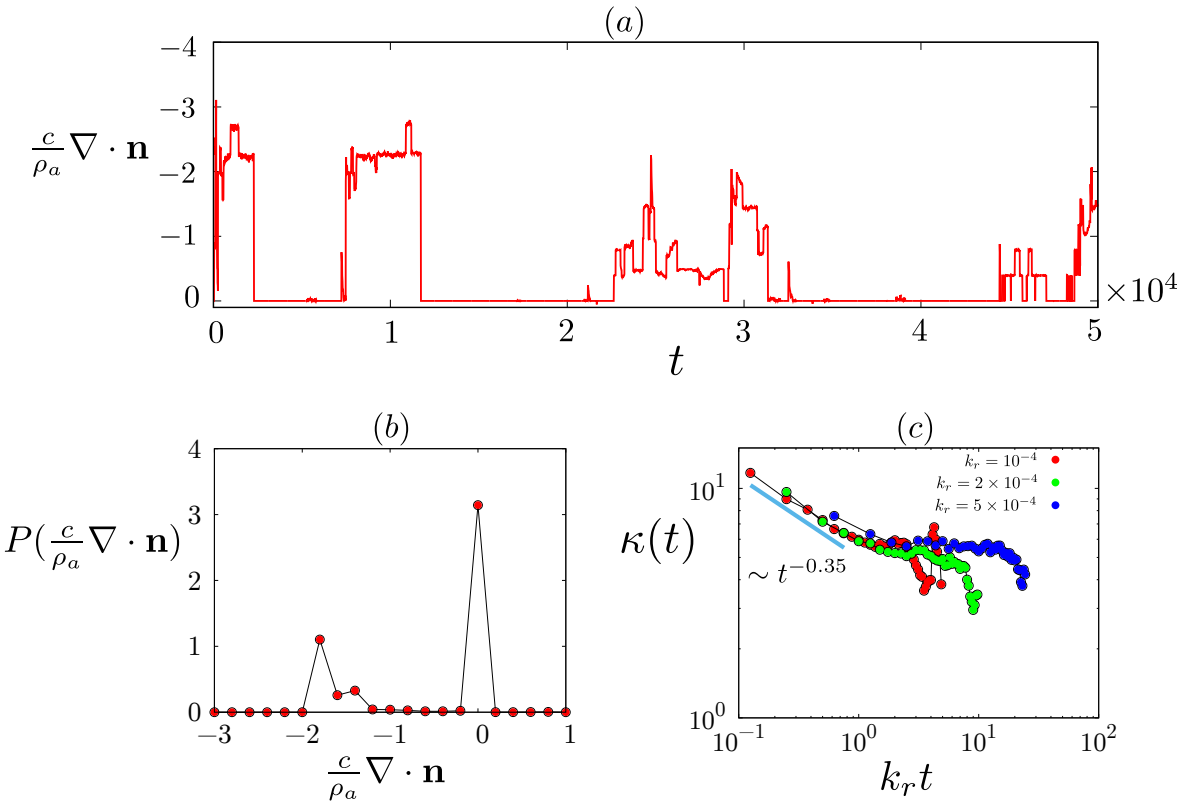

Figure 2.5 Nonequilibrium steady state characterised by intermittent orientational patterns as a result of contractile flows and turnover. (a) For instance, fixing parameters so as to be in the Aster phase of Fig. 2.4, we monitor the time series of the divergence $\frac{c}{\rho_a}\nabla\cdot\mathbf{n}$, averaged over an area of size $\frac{L}{4}\times\frac{L}{4}$. This shows large fluctuations ranging from a negative value (-2 for one pure aster, where $\mathbf{n}=-\hat{\mathbf{r}}$) to 0. (b) The corresponding probability distribution $P(\frac{c}{\rho_a}\nabla\cdot\mathbf{n})$ measured over 8 independent initial realisations and 100 time windows at steady state shows a spread of values from -2 to 0. Here, torsional spring stiffness $k_\theta = 5$, $k_\phi = 500$, and turnover rate $k_r = 2\times10^{-4}$. (c) Time dependent kurtosis $\kappa(t)$ of $\frac{c}{\rho_a}\nabla\cdot\mathbf{n}$ shows a power-law divergence as $k_rt\to 0$, where k_r is the turnover rate. This is characteristic of an intermittent nonequilibrim state. The corresponding $\kappa(t)$ for a Gaussian distributed variable would take a constant value equal to 3.

2.5 Discussion

Recent *in vitro* studies and computer simulations have shown that in order to *maintain* a nonequilibrium steady state characterised by steady active contractile flows, dynamic orientational patterning and dynamic protein clustering, one needs in addition to the stratification of the active machinery, a constant *turnover* of active

components, that give rise to a dynamic force patterning. Here we bring together, in a rather simple coarse-grained agent based simulation, all the ingredients necessary for observing the nonequilibrium steady state, viz., stratification, turnover and multivalency of force generators. Stratification relieves us of the obligation to include steric hindrance between molecular components that reside in different strata, though it is important to retain steric interactions between molecules that reside in the same layer. Even so such a computation would have been a daunting task, since including a representation of the essential structural features of Myo-II minifilaments in the cortical layer, would have made it exceedingly difficult to monitor long time dynamics. Thus, our coarse grained simulation method has intrinsic value, since it takes into account the effects of myosin minifilaments on currents, *forces* and *torques* applied to single and multiple actin filaments, without explicitly incorporating its structural details. Consistent with experimental observation, we we show that inhibition of any one of the three ingredients, leads to a loss of the desired phenotype.

We show that this simple coarse grained model, that incorporates the fluctuating active forces and torques in a stratified geometry, recapitulates the nonequilibrium steady states observed both *in vivo* [14, 8, 1, 19, 30, 18, 20] and in properly designed reconstitution experiments [15, 25, 26, 16].

References

[1] K. Gowrishankar, S. Ghosh, S. Saha, C. Rumamol, S. Mayor and M. Rao, Cell **149**, 1353 (2012).

[2] D. Pruyne, M. Evangelista, C. Yang, E. Bi, S. Zigmond, et al. Science **297** 612–15 (2002).

[3] I. Sagot, A. A. Rodal, J. Moseley, B. L. Goode and D. Pellman, Nat. Cell Biol. **4** 626–31 (2002).

[4] I Rouiller, XP Xu, KJ Amann, C Egile, S Nickell, et al., J. Cell Biol. **180** 887–95 (2008).

[5] E. D. Goley and M.D. Welch, Nat. Rev. Mol. Cell Biol. **7**, 713–726 (2006).

[6] N. Morone, T. Fujiwara, K. Murase, R. S. Kasai, H. Ike, S. Yuasa, J. Usukura and A. Kusumi, J. Cell Biol. **174**, 851 (2006).

[7] A. Maitra,P. Srivastava, Madan Rao and S. Ramaswamy, Phys. Rev. Lett. **112** 258101 (2014).

[8] D. Goswami, K. Gowrishankar, S. Bilgrami, S. Ghosh, R. Raghupathy, R. Chadda, R. Vishwakarma, M. Rao and S. Mayor, Cell **135**, 1085 (2008).

[9] S. J. Plowman, C. Muncke, R. G. Parton, and J. F. Hancock, Proc. Natl. Acad. Sci. USA **102**, 15500 (2005).

[10] D. Lingwood and K. Simons, Science **327**, 46 (2010).

[11] S. Saha, I.-H. Lee, A. Polley, J. T. Groves, M. Rao and S. Mayor, Mol. Biol. of the Cell **26**, 4033 (2015).

[12] N. Billington, A. Wang, J. Mao, R. S. Adelstein and J. R. Sellers, J. Biol. Chem. **288**, 33398–33410 (2013).

[13] R. Niederman and T. D. Pollard, J. Cell Biol. **67**, 72–92 (1975).

[14] M. Rao and S. Mayor, Curr. Opin. in Cell Biol. **29**, 126 (2014).

[15] D. V. Koster, K. Husain, E. Iljazi, A. Bhat, P. Bieling, R. D. Mullins, M. Rao and S. Mayor, Proc. Natl. Acad. Sci. USA **113**, E1645 (2016).

[16] A. Das, A. Bhat, R. Sknepnek, D. Koster, S. Mayor and M. Rao, Sci. Adv. **6**, 11, (2020).

[17] A. Kusumi, T. K. Fujiwara, R. Chadda, M. Xie, T. A. Tsunoyama, Z. Kalay, R. S. Kasai and K. G. N. Suzuki, Annu. Rev. Cell Dev. Biol. **28** 215-50 (2012).

[18] E. M. Reichl, Y. Ren, M. K. Morphew, M. Delannoy, J. C. Effler, K. D. Girard, D. Srikanth, A. I. Pablo, C Kuo Scot and N. R. Douglas, Curr. Biol. **18**, 471–480 (2008).

[19] M. Guha, M. Zhou, and Y. L. Wang, Curr. Biol. **15**, 732-736 (2005).

[20] Q. Yang, X. F. Zhang, T. D. Pollard and P. Forscher, J. Cell Biol. **197**, 939-956 (2012).

[21] M. P. Murrell and M. L. Gardel, Proc. Natl. Acad. Sci. USA **109**, 20820-20825 (2012).

[22] S. K. Vogel, Z. Petrasek, F. Heinemann and P. Schwille, eLife **2**, e00116 (2013).

[23] I. Linsmeier, S. Banerjee, P. W. Oakes, W. Jung, T. Kim and M. P. Murrell, Nat. Comm. **7**, 12615 (2016).

[24] G. Salbreux, G. Charras and E. Paluch, Trends Cell Biol. **22**, 536-545 (2012).

[25] Sonal, K. A. Ganzinger, S. K. Vogel, J. Mu cksch, P. Blumhardt and P. Schwille, Journal of Cell Science **132**, 219899 (2019).

[26] T. Han Tan, M. Malik-Garbi, E. Abu-Shah, J. Li, A. Sharma, F. C. MacKintosh, K. Keren, C. F. Schmidt, N. Fakhri, Science Advances **4**, 2847, (2018).

[27] L. Haviv, D. Gillo, F. Backouche. and A. Bernheim-Groswasser, J. Mol. Biol. **375**, 325-330, (2008).

[28] K. Murthy, and P. Wadsworth, Curr. Biol. **15**, 724–731 (2005).

[29] D. Raz-Ben Aroush, N. Ofer, E. Abu-Shah, J. Allard,O. Krichevsky, A. Mogilner and K. Keren, Curr. Biol. **27**, 2963-2973.e2914 (2017).

[30] N. A. Medeiros, D. T. Burnette and P. Forscher, Nat. Cell Biol. **8**, 216-226 (2006).

[31] T. B. Liverpool and M. C. Marchetti, Phys. Rev. Lett. **90**, 138102, (2003).

[32] A. Ahmadi, M. C. Marchetti and T. B. Liverpool, Phys. Rev. E **74**, 061913, (2006).

[33] Y. Yang, V. Marceau and G. Gompper, Phys. Rev. E **82**, 031904 (2010).

[34] M. Doi and S.F. Edwards, The Theory of Polymer Dynamics, Clarendon Press, Oxford (1986).

[35] J. Howard, Sinauer Associates, Sunderland (2001).

[36] G. H. Koenderink and E. K. Paluch, Curr. Opin. Cell Biol. **50**, 79-85 (2008).

[37] S. Mukhina, Y. l. Wang and M. Murata-Hori, Dev. Cell **13**, 554–565 (2007).

[38] K. Gowrishankar and M. Rao, Soft Matter **12**, 2040-2046 (2016).

[39] K. Husain and M. Rao, Phys. Rev. Lett. **118**, 078104 (2017).

[40] K. Kruse, J.F. Joanny, F. Jülicher, J. Prost and K. Sekimoto, Phys. Rev. Lett. **92**, 078101 (2004).

[41] F. Backouche, L. Haviv, D. Groswasser and A Bernheim-Groswasser, Phys. Biol. **3**, 264 (2006).

[42] D. S. Banerjee, A. Munjal, T. Lecuit and M. Rao, Nat. Commun. **8**, 1121 (2017).

[43] U. Frisch, Turbulence: The Legacy of A. N. Kolmogorov (Cambridge University Press, Cambridge, England, 1995).

[44] A. Das, A. Polley and M. Rao, Phys. Rev. Lett. **116**, 068306 (2016).

[45] A. Chaudhuri, B. Bhattacharya, K. Gowrishankar, S. Mayor and M. Rao, Proc. Natl. Acad. Sci. USA **108**, 14825 (2011).

End of Chapter

Chapter 3

Transport of passive advective scalars in a dilute active medium

3.1 Introduction

We have discussed in the introduction (chapter 1) that the spatial organization, clustering and dynamics of many cell surface molecules is influenced by interaction with the actomyosin cortex [1, 2, 3, 4, 5, 6]. A description of the cell surface as an *Active Composite* (Fig. 2.1), appears to consistently explain the anomalous dynamical features of these proteins [1, 3, 4]. Based on this *Active Composite* model, In chapter 2, we developed a coarse-grained agent-based Brownian dynamics simulation that incorporates the effects of stratification of actomyosin cortex agent, binding of *myosin minifilaments* to multiple actin filaments and their turnover. We have shown that these three features of the active cortical machinery - *stratification*, *multivalency* and *turnover* - are crucial to the attainment of a nonequilibrium steady state characterised by contractile flows and dynamic orientational patterning. The orientational patterns generated by the actin filaments driven by myosin minifilaments are isotropic, polar bundle, polar aster, aster and spiral aster (Fig. 2.4).

In this chapter, we have studied the effect of isotropic phase on the dynamics of membrane molecules in $z = 0$ plane in the stratified cortex picture of cell surface Fig. 2.1. In the dilute limit of actin filament when the overlap of filament is negligible the multivalency effect of minifilament is negligible. The only contributions to the active translational current $\mathbf{J}_a$, appearing in Eq. 2.1 come from the single actin filament translation ($\mathbf{F}_1 = f_0\hat{\mathbf{n}}$) driven by myosin minifilament. The other active

terms $\mathbf{F}_2, \mathbf{F}_3, \mathbf{M}_2, \mathbf{M}_3$ in the Eq. 2.2 that have their origin in the multivalency of myosin-II minifilaments in the stratified cortex do not contribute much to the active translational and rotational currents, $\mathbf{J}_a$ and $\mathcal{J}_a$ in this limit. This gives rise to the isotropic pattering of dynamic actin filaments.

Our present study is an agent-based Brownian dynamics simulation of a mixture of polar active filaments in isotropic phase and passive particles which interact with each other. Here we study the statistics of density fluctuations and dynamics of particles advected in an active *quasi*-two dimensional medium comprising of self-propelled filaments with no net orientational order, using a combination of agent-based Brownian dynamics simulations and analytical calculations. The particles interact with each other and with the self-propelled active filaments via steric interactions. Our choice of Brownian dynamics simulations is motivated by experiments on tagged particle diffusion both on the cell surface and in the *in vitro* reconstitution. Molecules that bind to dynamic actin (passive molecules) are affected by the active fluctuations of actomyosin - their diffusion shows anomalous behaviour strongly indicative of active driving. On the other hand, molecules that do not interact with actin (inert molecules), such as short chain lipids and proteins whose actin-binding domain has been mutated so as to abrogate their interaction with actin, do not show any influence of active fluctuations [3, 4, 7]. There appears to be no sign that the transport of these inert molecules is affected by potential hydrodynamic flows induced by active stresses coming from actomyosin [8, 9]. Our choice of Brownian dynamics simulations is justified science the dominant source of momentum dissipation is via friction associated with moving relative to the crosslinked cortical meshwork. We find that the particles show a tendency to cluster and their density fluctuations reflect their binding to and driving by the active filaments. The late-time dynamics of tagged particles is diffusive, with an *active diffusion* coefficient that is independent of (or at most weakly-dependent on) temperature at low temperatures. Our results are in qualitative agreement with the experiments mentioned above.

While our primary motivation are the experimental studies of the tagged particle dynamics on the cell surface [3, 4, 7], our work is also relevant to transport in other living and nonliving systems, as long as the effects of hydrodynamics are negligible, for instance, to the movement of multiple motor-driven cargo vesicles or synthetic

beads on the cytoskeletal network [10].

3.2 Brownian dynamics and characterization

3.2.1 Simulation details

We study the dynamics of a mixture of polar active filaments and passive particles using an agent-based Brownian dynamics simulation. The passive particles are modelled as mono-disperse soft spheres of diameter σ. A pair of passive particles separated by a distance r interact via a truncated Lennard Jones (LJ) pair potential of the form,

$$\begin{aligned} V_{pp}(r) &= 4\epsilon\left[\left(\frac{\sigma}{r}\right)^{12} - \left(\frac{\sigma}{r}\right)^{6}\right] + V_0 + V_2 r^2 \quad \text{for } r \leq r_c \\ &= 0 \quad \text{for } r > r_c \end{aligned} \tag{3.1}$$

where $r_c = 2.5\sigma$ and values of V_0 and V_2 are chosen so that the potential and force are continuous at the truncation point. We set $\sigma = 1$ and $\epsilon = 1$ to be the units of length and energy, respectively.

The polar filaments are modelled as semi-flexible bead-spring polymers, with both stretch and bend distortions [11, 12]. We implement excluded volume interaction between the beads of same filament, as well as between two different filaments through a truncated Lennard Jones pair potential of the form,

$$\begin{aligned} V_{bb}(r) &= 4\epsilon'\left[\left(\frac{\sigma'}{r}\right)^{12} - \left(\frac{\sigma'}{r}\right)^{6}\right] + V_0' + V_2' r^2 \quad \text{for } r \leq r_c' \\ &= 0 \quad \text{for } r > r_c' \end{aligned} \tag{3.2}$$

where r is the distance between the centres of the corresponding beads, $r_c' = 2^{1/6}\sigma'$ and V_0', V_2' are constants, chosen so that the potential and force are continuous at r_c'. We take $\sigma' = 2$ and $\epsilon' = 1$. Each filament is composed of 10 beads and therefore has an equilibrium length $l = 20$, in the units of σ.

Note that with our choice of cutoffs, the particle-particle interaction V_{pp} has both attractive and repulsive parts, whereas the bead-bead interaction V_{bb} is strictly re-

pulsive.

To make the filament semi-flexible, we impose additional spring forces on the beads. A harmonic stretching potential with extensile stiffness $K_c = 400$, in units of ϵ/σ^2, ensures that the length of the filament does not deviate significantly from its equilibrium value, $l = 20$. The bending energy of a triplet of connected beads is also harmonic in the angle, with a bending stiffness $K_b = 600$, in units of ϵ. This high K_b makes the filaments very stiff, with a typical persistence length much larger than l.

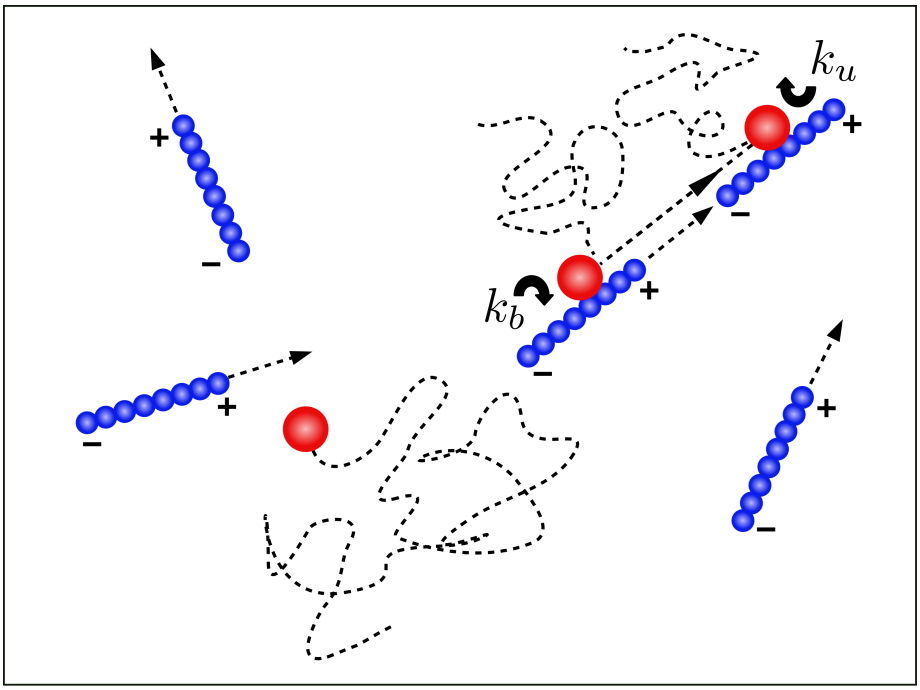

Figure 3.1 Schematic of the agent-based model, where the polar filaments (indicated by +/−) built from beads (blue) propel in a 2d background of passive particles (red). The passive particles can bind to the filaments with rate k_b and are advected with it. Upon unbinding with rate k_u , the passive particles undergo simple thermal diffusion.

A propulsion force $\mathbf{F}_1 = f_0\hat{\mathbf{n}}$ is imposed on each of the beads, along the average direction ($f_0\hat{\mathbf{n}}$) of all the bonds present in a filament. Note that we do not impose any filament alignment rule nor do we prescribe any activity decorrelation time. Instead, these originate from thermal fluctuations on the constituent monomers comprising each filament and collisions driven by thermal and active forces, an

emergent many-particle feature. As a consequence, both the local alignment and orientational de-correlation time are functions of temperature, density and activity.

On the other hand, the passive particles are subject to thermal noise and can bind and unbind to the beads of the filament. The interactions between the beads of the filament and the passive particles are modelled by a harmonic potential of spring constant $K_s = 50$ in units of ϵ/σ^2. The harmonic potential is truncated at a cutoff distance $r_0 = 1$ and set to zero beyond it. When a passive particle comes within a distance r_0 from the centre of a filament bead, it binds to the corresponding bead and gets advected along with the filament, under the application of propulsion force $f_0\hat{\mathbf{n}}$. The unbinding of the passive particle from the filament is facilitated by thermal noise. We will later characterise the binding/unbinding rates as a function of K_s and temperature. Note that we do not include any steric interaction between the passive particles on the membrane and the filaments in the cortex. A schematic showing the dynamic processes is displayed in Fig. 3.1(a).

Unless mentioned otherwise, all results presented here are for $N_p = 800$ passive particles and $N_r = 50$ self-propelled filaments in a two dimensional (2d) area of linear dimension $L = 396.4$ with periodic boundary conditions (PBC). For most of the study, we take the area fractions of the filaments (c) and particles (ρ) to be $c = 0.01$ and $\rho = 0.004$, respectively.

The Brownian dynamics equations involve an update of both the passive particle and the filament bead coordinates, for which we have used a simple Euler integration scheme with integration time step $\Delta t \sim 10^{-4}$. The dynamics of the position of the i-th passive particle is given by

$$\dot{\mathbf{r}}_i^p = \begin{cases} -\gamma_p^{-1}\boldsymbol{\nabla}_i V_p + \sqrt{2k_BT/\gamma_p}\boldsymbol{\xi}_i, & \text{(unbound)} \\ -\gamma_p^{-1}\boldsymbol{\nabla}_i V_p + \sqrt{2k_BT/\gamma_p}\boldsymbol{\xi}_i + \mathbf{f}_i/\gamma_p, & \text{(bound)} \end{cases} \tag{3.3}$$

where γ_p is the friction coefficient of the passive particle, V_p is the net potential felt by the i-th passive particle and includes contributions from Eq. 3.1 and the bead-particle spring interactions. The diffusion of the unbound particle is driven by a thermal noise $\boldsymbol{\xi}_i$ with zero mean and unit variance acting on i-th particle (k_B is the Boltzmann constant. On the other hand, the bound particles are subject to both the thermal noise and active driving.

The dynamics of the filament-bead displacements in our simulation is

$$\dot{\mathbf{r}}_j^b = -\gamma_b^{-1}\boldsymbol{\nabla}_j V_b + \sqrt{2k_BT/\gamma_b}\,\boldsymbol{\xi}_j + \mathbf{f}_j/\gamma_b \tag{3.4}$$

where γ_b is the friction coefficient of the bead, V_b is the net potential felt by the j-th bead and includes contributions from Eq. 3.2, harmonic stretching and bending interactions. The advection force $\mathbf{f}_j$ on j-th bead acts along the direction of the filament the bead is part of. Since our study is entirely in the isotropic phase of the filaments, we have ignored complications that would arise by considering anisotropies in *both* friction and thermal noise, as required by detailed balance.

We take $\gamma_p = 1$, which together with $\sigma = 1$ and $\epsilon = 1$, sets the units of space, time and energy. All other quantities can be written in terms of these units, so as to make Eqs. 5.3, 3.4 dimensionless. In all that follows below, except in Sec. V, we have taken $\gamma_b = \gamma_p$. A typical snapshot of the simulation is shown in Fig. 3.1(b).

Table 3.1 Conversion between simulation units (S.U.) and real units (R.U.)

$Parameter[Dimension]$	$S.U.$	$R.U.$
σ $[l]$	1	10 nm
ϵ $[ml^2t^{-2}]$	1	4.14×10^{-21} J
γ_p $[mt^{-1}]$	1	0.123 $pN\mu m^{-1}s$
T $[k]$	1	300 K
t $[t]$	1	3×10^{-3} s
k_u, k_b $[t^{-1}]$	1	333 s^{-1}
f_0 $[mlt^{-2}]$	1	0.41 pN
V_a $[lt^{-1}]$	1	3.3 μm s^{-1}
K_c $[mt^{-2}]$	1	41.4 $pN\mu m^{-1}$
K_b $[ml^2t^{-2}]$	1	4.14×10^{-21} J
K_s $[mt^{-2}]$	1	41.4 $pN\mu m^{-1}$
D $[l^2t^{-1}]$	1	3.3×10^{-2} $\mu m^2/s$

To be able to make contact with the *in vitro* reconstitution experiments [7], we

translate our simulation units (S.U.) to real units (R.U.). Setting $\sigma = 10\,\mathrm{nm}$, $\gamma_p = 0.123\,\mathrm{pN}\ \mu m^{-1}$ s [13] and $\epsilon = 4.14 \times 10^{-21}\,\mathrm{J}$, we can convert our simulation units to real units, as displayed in Table 1. Note however, that if we were to compare our simulation results with some other experimental system (e.g., an appropriately designed active colloidal suspension), then we would have to use a different conversion factor. To allow for this, we have varied the dimensionless temperature over the range $T = 0.25 - 10$ and the dimensionless propulsion force over the range $f_0 = 0 - 4.0$. We have typically run the Brownian dynamics simulation for a total time $t \sim 10^4$, ensuring that the system has reached steady state. Our initial conditions are chosen from a thermal distribution at temperature T and all results presented here are averaged over 16 such independent initial realisations. Throughout the paper (unless mentioned otherwise) we work at a filament density of $c = 0.01$, and temperatures $T \geq 0.5$; in this regime, the orientational correlation lengths are of the order of the filament length, l, and hence comfortably within the isotropic phase.

3.2.2 Statistics of filament orientation

We characterise the i-th filament by its centre of mass position $\mathbf{r}_i$ and a unit vector $\mathbf{n}_i = (\cos\theta_i, \sin\theta_i)$ along its long axis to describe its polar orientation (recall that the filaments are very stiff). We first ensure that the configuration of filaments is in the spatially homogeneous, orientationally isotropic state - this is demonstrated in the plots of the probability distribution of the polar $P(\theta)$ and nematic orientations $P(\tilde{\theta})$ (Fig. 3.2).

We then calculate the orientational correlation lengths, so as to ensure that this is much smaller than our system size and comparable to the size of the filaments. To do this, we calculate the spatial correlations of both the polar and nematic orientation,

$$C_P(r) = \left\langle \frac{1}{N^2} \sum_{i=1}^{N} \sum_{j=1}^{N} \cos(\theta_i - \theta_j) \right\rangle \tag{3.5}$$

$$C_N(r) = \left\langle \frac{1}{N^2} \sum_{i=1}^{N} \sum_{j=1}^{N} (2\cos^2(\theta_i - \theta_j) - 1) \right\rangle \tag{3.6}$$

where $r = |\mathbf{r}_i - \mathbf{r}_j|$ is the distance between the centre-of-mass of the i-th and j-th filaments. By fitting this to an exponential (Figs. 3.3 and 3.4), we extract the polar and nematic orientation correlation lengths, ζ_P and ζ_N, whose dependence on the area fraction of filaments c (we will henceforth refer to this as filament density) is shown in the inset.

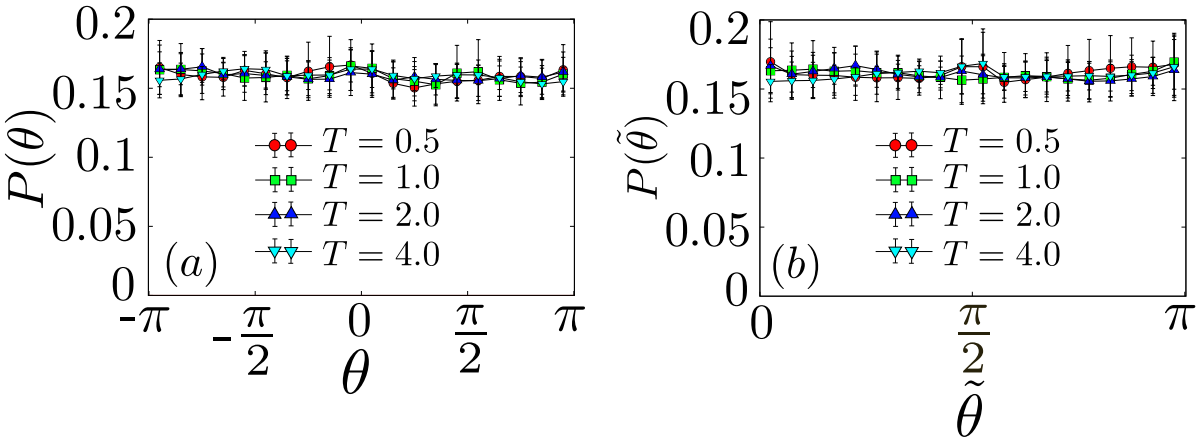

Figure 3.2 Normalised distribution of (a) polar orientation $P(\theta)$ and (b) nematic orientation $P(\tilde{\theta})$, of the filaments at different temperature T with activity $f_0 = 4.0$, showing that the system is in the isotropic phase for a representative set of parameters. Data displayed with standard deviations over 16 independent realisations.

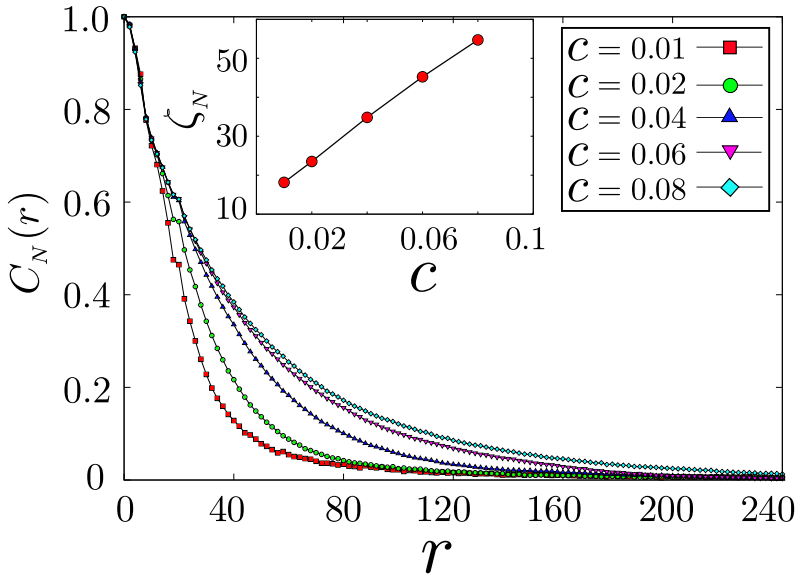

Figure 3.4 Spatial correlation of the nematic orientation, $C_N(r)$, of the filaments at different filament density c at $T = 0.5$ and $f_0 = 4$. Inset shows the corresponding correlation length ζ_N as a function of filament density c.

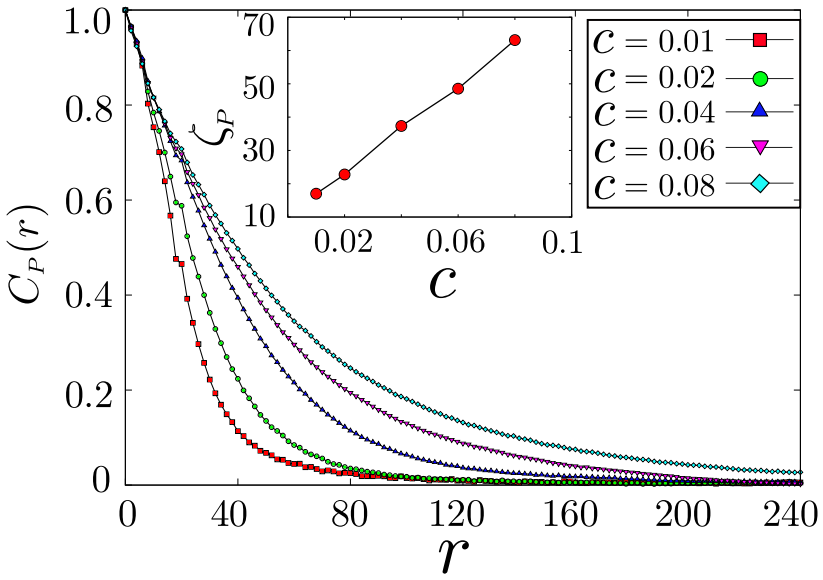

Figure 3.3 Spatial correlation of the polar orientation, $C_P(r)$, of the filaments at different filament densities c at $T = 0.5$ and active propulsion $f_0 = 4$. Inset shows the corresponding correlation length ζ_P as a function of filament density c.

3.2.3 Statistics of binding-unbinding of passive particles onto filaments

The dynamical equations (5.3) and (3.4) are written entirely in terms forces, either active or derived from a potential, and thermal noise. The particles experience a binding and unbinding onto the filaments which depend on this interplay between thermal noise and the attractive potentials. Thus for instance, the unbound passive particles diffuse in the two dimensional medium and ever so often come within the vicinity ($r \leq r_0 = 1$) of a moving filament-bead, whereupon they bind to the filament-bead. In the low density limit, we expect the binding rate k_b to be diffusion limited and so $k_b \propto T$ and independent of K_s where K_s is the strength of trapping harmonic interaction.

To study the unbinding of a particle bound from a filament-bead, we compute the rate of escape of a particle trapped in a truncated attractive harmonic potential [14], parametrised by K_s and r_0. This is given by

$$k_u = \frac{K_s^2 r_0^2}{\gamma_p k_B T} \exp\left(-\frac{K_s r_0^2}{2 k_B T}\right) \tag{3.7}$$

and should be a good description of the dynamics of unbinding of the passive particles in the limit of low particle density.

We compare these theoretical estimates with the results of simulations on a mixture of particles and filaments at equilibrium (no active propulsion), from which we extract the values of k_u and k_b in two different ways. In the first method, we represent the stochastic binding and unbinding by a telegraphic process [15], characterised by a mean duty ratio,

$$\langle \phi \rangle = \frac{k_b}{k_b + k_u}\,, \tag{3.8}$$

the fraction of time spent by the tagged particle in the bound state over the observation time, and a two-point correlator,

$$\langle \phi(t)\phi(t') \rangle = \langle \phi \rangle^2 + \langle \phi \rangle \left(1 - \langle \phi \rangle\right) e^{-2\frac{|t-t'|}{t_{sw}}} \tag{3.9}$$

where

$$t_{sw} = \frac{2}{k_b + k_u}\,, \tag{3.10}$$

is called the mean switching time and describes the mean time taken to switch from a bound to an unbound state. We calculate k_b and k_u, by fitting our simulation results to $\langle \phi \rangle$ and $\langle \phi(t)\phi(t') \rangle$. In the second method, we calculate k_u (k_b) directly, from the inverse mean time that the particle stays bound (unbound) on the filament.

Upto a scaling by a constant, the two numerical methods show identical variation as a function of temperature T and particle-filament binding potential K_s. These in turn agree with our analytical estimates, with no fit parameter (Fig. 3.5).

It is important that we do not *prescribe* the binding-unbinding rates, rather we derive them from the assigned potentials. The binding-unbinding rates thus depend nontrivially on temperature; they would also depend on the density of passive particles and filaments in the high density limit. This will be crucial to our estimation of the tagged particle diffusion coefficient and its comparison with experimental data (Sect. IV B).

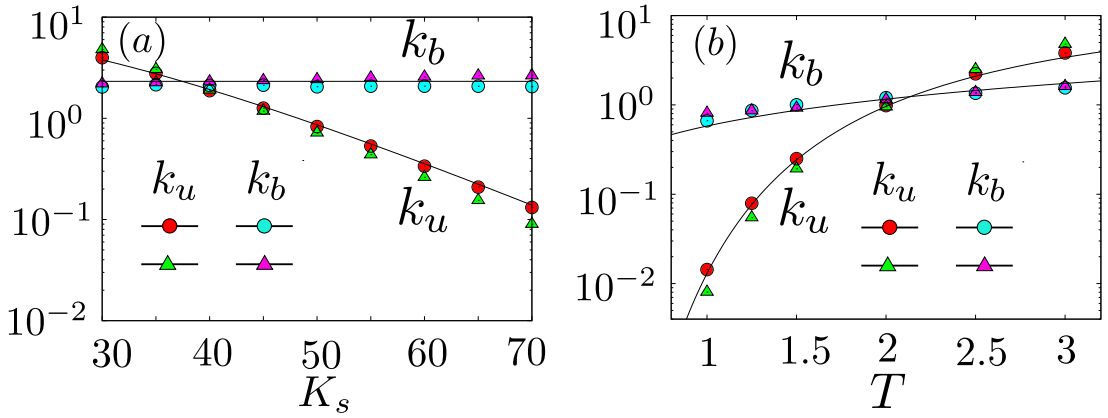

Figure 3.5 Dependence of binding (unbinding) rates k_b (k_u) on (a) the strength of the particle-filament binding potential, K_s, and (b) temperature, T, calculated using the two different numerical methods (filled symbols) discussed in the text. These can be fit, with no undetermined parameter, to the analytic forms (solid lines) discussed in the text (Eq. 3.7).

3.3 Density fluctuations of passive advective scalars in an active medium

We now study the statistics of density fluctuations and dynamics of the actively driven passive particles. We find that the active driving tends to cluster the passive particles; this shows up in the two point spatial density correlation function and the statistics of the density fluctuations.

3.3.1 Radial distribution function

We study the behaviour of the radial distribution function of the passive particles $g(r)$,

$$g(r) = \frac{1}{N_p \rho} \left\langle \sum_i \sum_{i \neq j} \delta(r - |\mathbf{r_i} - \mathbf{r_j}|) \right\rangle, \tag{3.11}$$

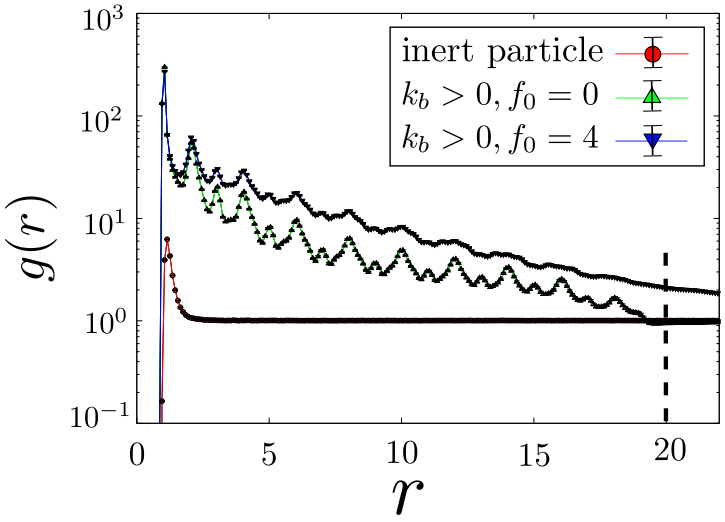

Figure 3.6 Radial distribution function $g(r)$ for (i) equilibrium system of inert particles ($k_b = 0$: red •), (ii) equilibrium system of psaaive particles which can bind to the filaments ($k_b > 0$, $f_0 = 0$: green △) and (iii) driven system of passive particles which can bind to the self-propelled filaments ($k_b > 0$, $f_0 = 4$: blue ▽). In the presence of activity the peak heights increase and $g(r)$ falls off more gradually, indicating a high degree of clustering of the bound particles, even at distances larger than the filament length. Data displayed with standard deviations over 16 independent realisations.

where N_p is the total number of passive particles and ρ the passive particle density. When $k_b = 0$ and $f_0 = 0$, i.e., when the particles do not bind to the filament (inert particles) and there is no propulsion force, $g(r)$ has the form of a dilute fluid (Fig. 3.6).

When we allow for particle binding, but in the absence of propulsion force, the $g(r)$ displays oscillations, which arise from particles binding to periodic locations on the filaments (Fig. 3.6) - note $r = 20$ coincides with the filament length. In this equilibrium situation, the particles not bound to the filaments do not show any clustering. We now consider the case when the filaments are driven by a propulsion force f_0. We see that the propulsion drives the clustering of the filaments, which in turn leads to an increase in correlation between bound particles, even at distances beyond the filament length (Fig. 3.6).

3.3.2 Probability distribution of local number density

This activity induced clustering of the passive particles should be reflected in the probability distribution of the excess number density. To compute this we divide the system into blocks of size $\Omega = 39.64$ and count the number of passive particles n in each block, to obtain the steady state distribution $P(n)$.

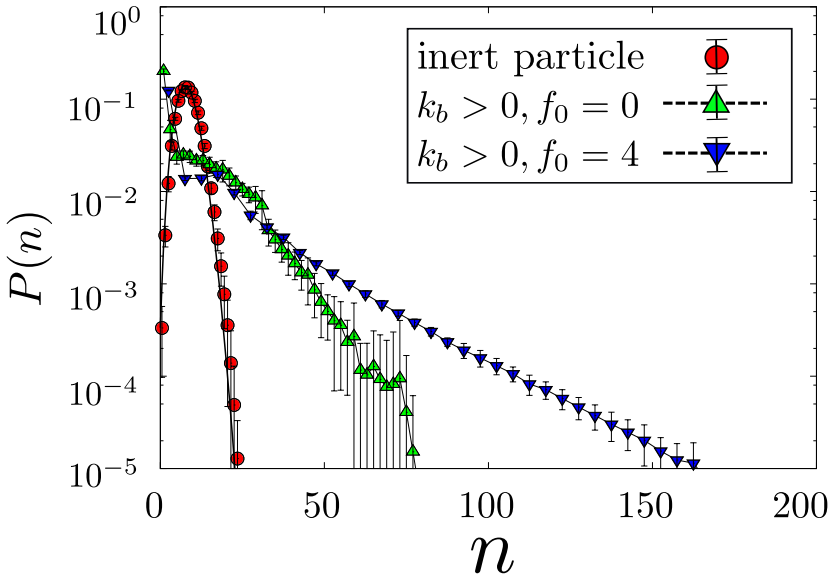

Figure 3.7 Probability distribution of number density $P(n)$ for (i) equilibrium system of inert particles ($k_b = 0$: red •), (ii) equilibrium system of psaaive particles which can bind to the filaments ($k_b > 0$, $f_0 = 0$: green △) and (iii) driven system of passive particles which can bind to the self-propelled filaments ($k_b > 0$, $f_0 = 4$: blue ▽). For inert particles, $P(n)$ fits with Poisson distribution Eq. 3.12 (dark line). $P(n)$ picks up an exponential tail for particles that bind and unbind onto the filaments, that moves towards the typical value as the active propulsion force gets larger. Data displayed with standard deviations over 16 independent realisations.

The statistics of density fluctuations of inert particles, in the dilute limit (Fig. 3.7), are described by a probability distribution that resembles a gas at temperature T and the average number of particle in the blocks $\bar{n}$, namely,

$$P(n) = \frac{\lambda^n exp(-\lambda)}{n!} \tag{3.12}$$

where mean number of particle in the blox is $\lambda = \bar{n} = \Omega\rho$.

On the other hand, the probability distribution for passive particles picks up an

exponential tail arising from the binding-unbinding statistics of the particles. This exponential tail gets more pronounced when the filaments are made active, and which moves towards the typical value as the active propulsion force gets larger (Fig. 3.7). This reflects the fact that for high driving, the typical particle is clustered. Both these results are consistent with the observed clustering of actin-binding proteins driven by actomyosin flows in the *in vitro* reconstitution system reported in Ref. [7].

3.3.3 Number fluctuations : crossover from anomalous to Brownian

Note that the active system of filaments is in the isotropic phase and we should not expect to see giant number fluctuations normally associated with active systems with global orientational order [16, 18, 17]. However when we compute the root mean square fluctuations $\triangle n$ and mean $\bar{n}$ of the number of passive particles over regions of ever increasing area, and plot them with respect to each other, we find that initially $\triangle n \propto \bar{n}^{\alpha}$ with $\alpha = 0.784$. Subsequently, as $\bar{n}$ increases, the variance scaling shows a cross over to $\alpha = 0.5$. This crossover occurs over a scale corresponding to the orientational correlation length, which can in principle be large, especially close to the isotropic-nematic transition or high f_0. This is especially apparent in the high particle density regime, see Fig. 3.8 for particle density $\rho = 0.05$ and filament density $c = 0.02$. This slow crossover explains the observed anomalous number fluctuations in the *in vitro* actomyosin reconstitution system [7]. In order to recover the crossover to the expected normal fluctuations at large n, one needs to probe over length scales larger than this crossover length [19].

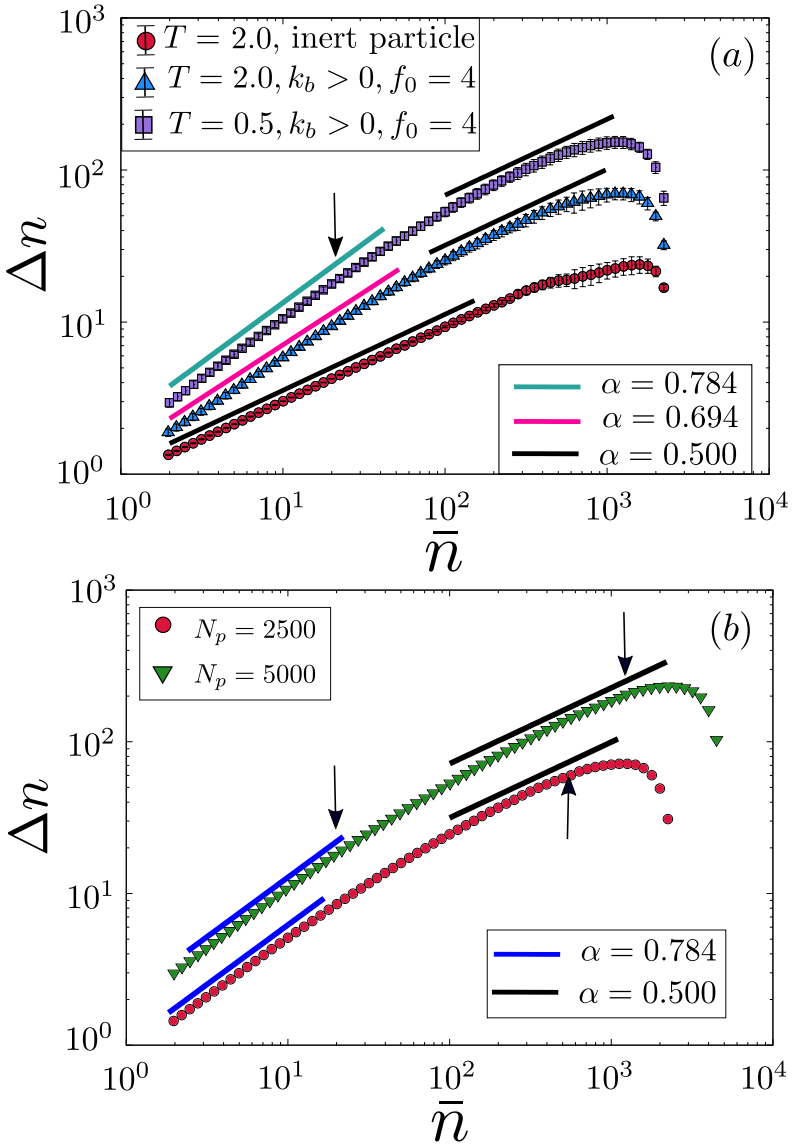

Figure 3.8 (a) Root mean square fluctuations of the number of passive particles Δn versus the mean $\bar{n}$ for inert (red •) and passive particles at two different temperatures, $T = 0.5$ (△) and $T = 2.0$ (□). Solid lines indicate the local slope α in this log-log plot of $\Delta n \propto \bar{n}^{\alpha}$. The values of α indicated in the legend, show that while inert particles exhibit normal fluctuations ($\alpha = 0.5$), passive particles show large fluctuations at small $\bar{n}$ (with α depending on T and f_0) that crosses over to normal fluctuations beyond a scale corresponding to the orientational correlation length (indicated by the arrow). Data displayed with standard deviations over 16 independent realisations. (b) To study the crossover behaviour, we plot Δn versus $\bar{n}$ for two different system sizes at $T = 0.5$. The crossover from $\alpha = 0.784$ to $\alpha = 0.5$ occurs at the orientational correlation length (arrow to the left), which being much smaller than system size, does not show any difference in the two system sizes. However, the eventual flattening and drop of the curve at large $\bar{n}$ is a system size effect, as seen by the arrows to the right. The $N_p = 2500$ data has been shifted along the y-axis for better visualisation.

3.4 Transport of passive advective scalars in an active medium

We now study the transport of passive particles moving in the active medium. Because the filaments are orientationally disordered, the long time dynamics of the particles is always diffusive. However the diffusion characteristics can change depending on the statistics of (un)binding to the active filaments.

3.4.1 Typical trajectories

The space-time trajectories of the passive particles show three qualitatively different behaviours. At very low temperatures compared to $\overline{U} = K_s r_0^2/4$, a passive particle once bound to a filament, rarely unbinds, and hence gets advected with the self-propelled filament (Fig. 3.9(a)). The direction of advection changes because of thermal fluctuations and collisions between filaments.

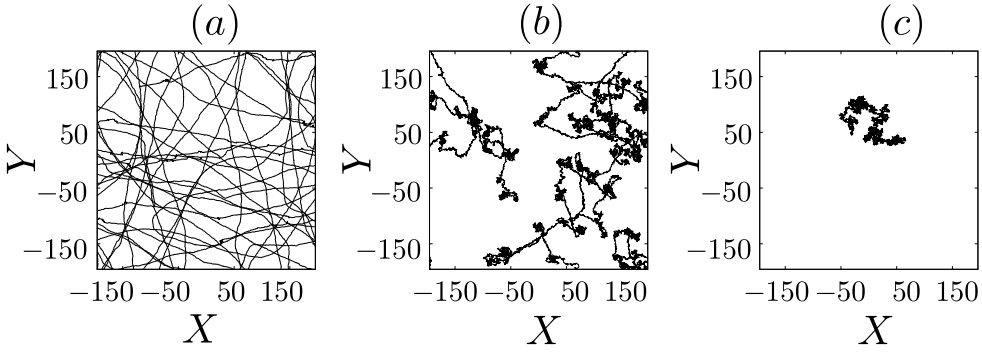

Figure 3.9 Typical trajectories of passive particles for a fixed propulsion force $f_0 = 4.0$ at different temperatures - (a) $T = 0.5$ (low : $k_B T/\overline{U} = 0.04$); (b) $T = 4.0$ (intermediate : $k_B T/\overline{U} = 0.32$) and (c) $T = 10.0$ (high : $k_B T/\overline{U} = 0.8$).

Increasing the temperature increases the probability of unbinding from the filament, whereupon the particle undergoes unrestricted thermal diffusion before binding again (Fig. 3.9(b)). At even higher temperatures, $k_B T/\overline{U} \approx 1$ the particles do not bind to the filaments and the motion is simple thermal diffusion (Fig. 3.9(c)).

3.4.2 Statistics of displacements

Propensity distribution. The distribution of displacements Δx (along the $\hat{\mathbf{x}}$ direction) evaluated over a time window t_w is called the *propensity distribution*. This will depend on the statistics of binding/unbinding, which in turn depends on the temperature T and f_0, densities of filaments and particles, and of course on the time window t_w, which we fix at $t_w = 10$. This can be obtained both from our Brownian dynamics simulation and, in the dilute limit, analytically.

In the dilute limit, one can obtain the form of this probability distribution from the stationary process describing the particle vector-displacements in a small time interval t_w,

$$\mathbf{r}(t_w) = \mathbf{r}(0) + \int_0^{t_w} \mathbf{V}(t')\, dt' \tag{3.13}$$

where $\mathbf{V}$ is the velocity of the tagged particle at time t, given by,

$$\mathbf{V}(t) = \phi(t)\, \frac{f_0}{\gamma}\, \hat{\mathbf{n}}(t) + (1 - \phi(t))\, \boldsymbol{\xi}(t), \tag{3.14}$$

where $\hat{\mathbf{n}}$ is the polar vector representing the orientation of the filament to which the particle is bound at time t, $\boldsymbol{\xi}$ is the thermal noise, and $\phi(t)$ is the telegraphic noise whose statistics is described in Sect. II D. The distribution of the particle displacements $\Delta x_{t_w} \equiv (\mathbf{r}(t_w) - \mathbf{r}(0)) \cdot \hat{\mathbf{x}}$, can be obtained by evaluating,

$$P(\Delta x) = \langle \delta\left(\Delta x - \Delta x_{t_w}\right) \rangle \tag{3.15}$$

where Δx_{t_w} is obtained from Eq. 3.13 and the angular bracket denotes an average over the joint distribution of $\boldsymbol{\xi}$ and ϕ. This can be evaluated by standard techniques of Fourier transformation and cumulant expansion [15],

$$\ln \tilde{P}(k) = \sum_{m=1}^{\infty} \frac{(ik)^m}{m!} \langle (\Delta x_{t_w})^m \rangle_c \tag{3.16}$$

where $\tilde{P}(k)$ is the Fourier transform of $P(\Delta x)$. The m-th cumulants $\langle (\Delta x_{t_w})^m \rangle_c$ can be evaluated from Eqs. 3.13, 3.14, knowing that ϕ and $\boldsymbol{\xi}$ are independent stochastic processes. The distribution $P(\Delta x)$ is then obtained by taking the inverse Fourier

transform of $\tilde{P}(k)$.

However, in practice, the inverse Fourier transform of $\tilde{P}(k)$, for the stationary process Eq. 3.13, has to be evaluated numerically. Rather than do this, we provide an alternate argument which gives more insight.

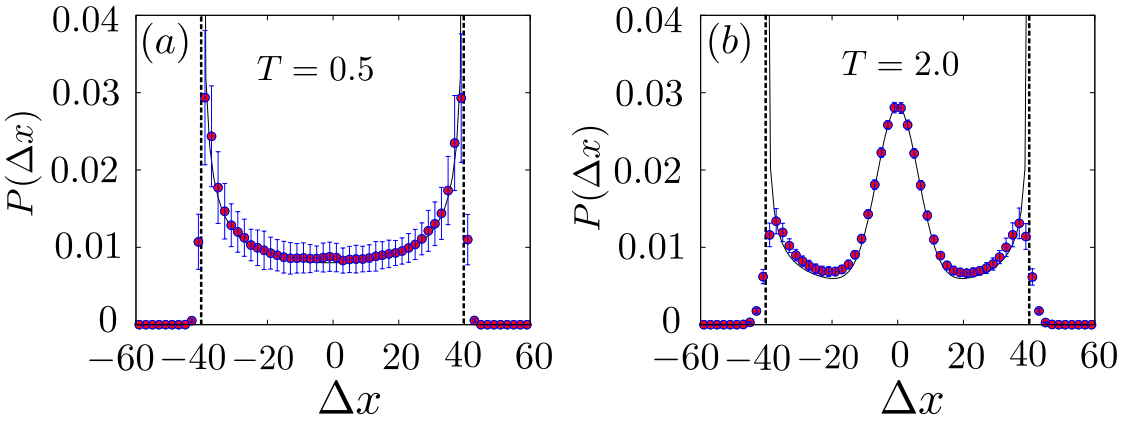

Figure 3.10 Probability distribution $P(\Delta x)$ of the displacements of passive particles, evaluated for fixed time interval $\triangle t = 10$, at a propulsion force $f_0 = 4.0$ and temperatures (a) $T = 0.5$ and (b) $T = 2.0$. The central peak comes from the fraction undergoing thermal diffusion, while the side peaks come from the bound fraction undergoing active motion. The black filled line shows parameter-free fits to the approximate analytical form (Eq. 3.17), where we have estimated the value of $\langle\phi\rangle = 0.9995$ at $T = 0.5$ (mainly bound) and $\langle\phi\rangle = 0.632$ at $T = 2.0$. Data displayed with standard deviations over 16 independent realisations.

At low enough T, the passive particles are completely bound to the self-propelled filaments, and so as long as $t_w < \tau$, the orientational correlation time of the filaments, the particles get displaced by $\Delta\mathbf{r} = \frac{f_0 t_w}{\gamma_p}\hat{\mathbf{n}}$, where γ_p is the friction coefficient and $\hat{\mathbf{n}}$ is the unit vector representing the average orientation of a filament during time interval t_w.

Since the filament orientation is uniformly distributed, the contribution to the step-size distribution from this process is $P(\Delta x) = \frac{\gamma_p}{\pi f_0 t_w}\frac{1}{\sqrt{1-(\frac{\gamma_p}{f_0}\frac{\Delta x}{t_w})^2}}$. On the other hand, at very high T, the particles are completely unbound and undergo thermal diffusion, for which the step-size distribution is $P(\Delta x) = \frac{1}{\sqrt{2\pi\sigma^2}}\exp\left[-\frac{(\Delta x)^2}{2\sigma^2}\right]$, where $\sigma^2 = \frac{2k_BT}{\gamma_p}t_w$. We propose that at an intermediate T, the propensity distribution

can be written as a linear combination, weighted by the duty ratio $\langle\phi\rangle$, i.e.,

$$P(\Delta x) = \frac{\gamma_p}{\pi f_0 t_w} \frac{\langle\phi\rangle}{\sqrt{1-\left(\frac{\gamma_p}{f_0}\frac{\Delta x}{t_w}\right)^2}} + \frac{1-\langle\phi\rangle}{\sqrt{2\pi\sigma^2}} \exp\left[-\frac{(\Delta x)^2}{2\sigma^2}\right]. \tag{3.17}$$

Considering that there are no undetermined parameters, the agreement of this approximate analytical form with the results of the Brownian simulation is quite reasonable, see Fig. 3.10.

3.4.3 Mean square displacement and diffusion coefficient

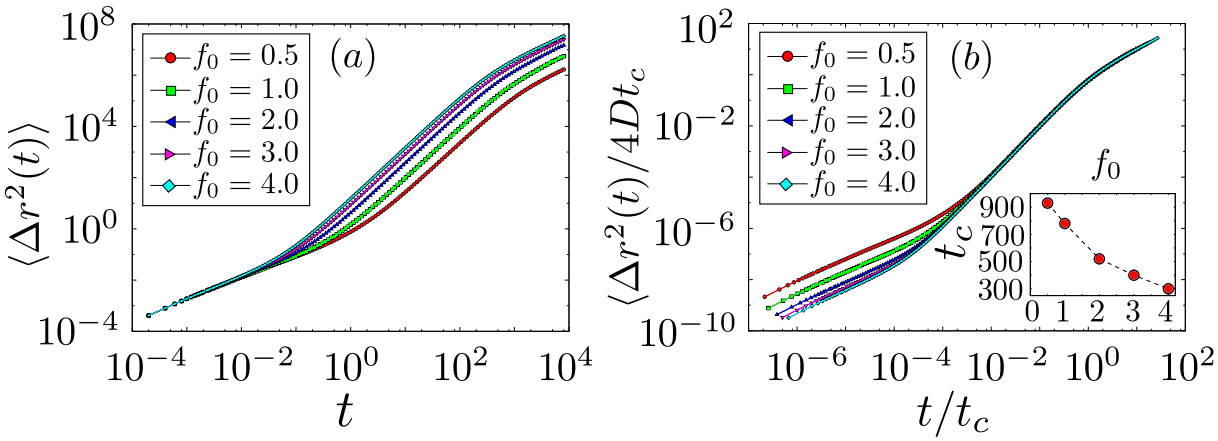

Figure 3.11 (a) MSD of passive particles as a function of time at $T = 0.5$ for different values of self-propulsion force (f_0) of the filaments. (b) Collapse of MSD using crossover time (t_c) and long time diffusion constant for the same case. Inset shows crossover time (t_c) as a function of self-propulsion force (f_0) of the active filaments for the same case.

From the statistics of the displacement we can compute the mean square displacement (MSD) as $\langle\Delta\mathbf{r}^2(t)\rangle = \langle\frac{1}{N_p}\sum_i |\mathbf{r}_i(t_0+t)-\mathbf{r}_i(t_0)|^2\rangle$, where $\mathbf{r_i}$ is the position of the i-th particle. This shows a change from a short time diffusive regime crossing over to a long time diffusive regime via an intermediate super-diffusive regime (Fig. 3.11(a)). We estimate the second crossover time $t_c(T, f_0)$ from the super-diffusive to late time

diffusion D, by fitting the simulation data to $\langle \Delta \mathbf{r}^2(t) \rangle = 4Dt\,[1 - \exp(-t/t_c)]$ [20], using which we can collapse the MSD data for different values of active propulsion f_0 (Fig. 3.11(b)). From this we see that t_c decreases with f_0 (Fig. 3.11(b) inset). This is because the filament orientation decorrelates on account of collisions, whose frequency increases with f_0. In experimental systems where hydrodynamics plays a crucial role [20], this dependence of t_c on f_0 may be different.

In situations where the crossover t_c is large, the apparent super-diffusion behaviour would last for many decades in time. We can then fit the MSD to $\langle \Delta \mathbf{r}^2(t) \rangle \sim t^\beta$ to obtain the super-diffusion exponent $\beta > 1$ - we find that $\beta = 1.95$ at $T = 0.5$ and $\beta = 1.77$ at $T = 2.0$, for a propulsion force $f_0 = 4.0$.

Temperature and activity dependence of MSD.

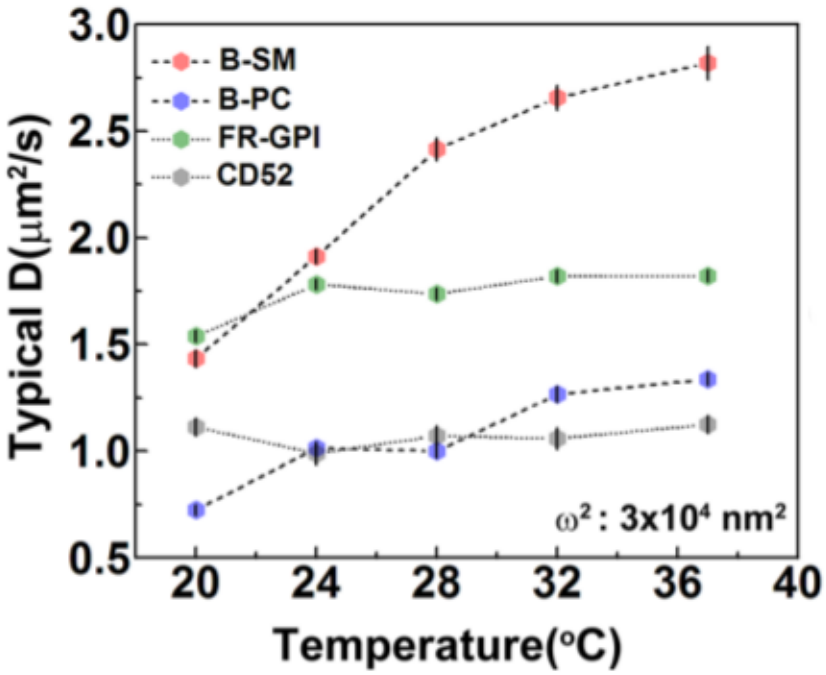

Figure 3.12 Diffusion of membrane proteins exhibit temperature insensitivity. Typical diffusion coefficient (D) has been extracted from FCS measurements for lipids and proteins in CHO cells across the temperature range $20 - 37°C$. The inert lipid probes (B-SM and B-PC) show distinct temperature dependence, whereas the GPI probes (FR-GPI and CD52) show temperature insensitivity (Image Courtesy: [4]).

We now compute the late time diffusion coefficient of the tagged particles, $D =$

$\lim_{t\to\infty}\langle\Delta\mathbf{r}^2(t)\rangle/4t$, for different T and f_0. For a fixed f_0, one might expect that at low temperatures D is weakly dependent on (or even independent of) temperature because a particle once bound to the filament remains so and undergoes *active diffusion* as it is transported by the filament (Fig. 3.13). As we increase the temperature, D decreases, since a particle spends less time, on an average, bound to the filament (recall we have set $\gamma_b = \gamma_p$).

At high temperatures, the particles are predominantly unbound, and hence D resembles that of an inert particle, which increases linearly with temperature. This is indeed what we see from a direct numerical simulation of the Brownian dynamics trajectories of a tagged particle (Fig. 3.13).

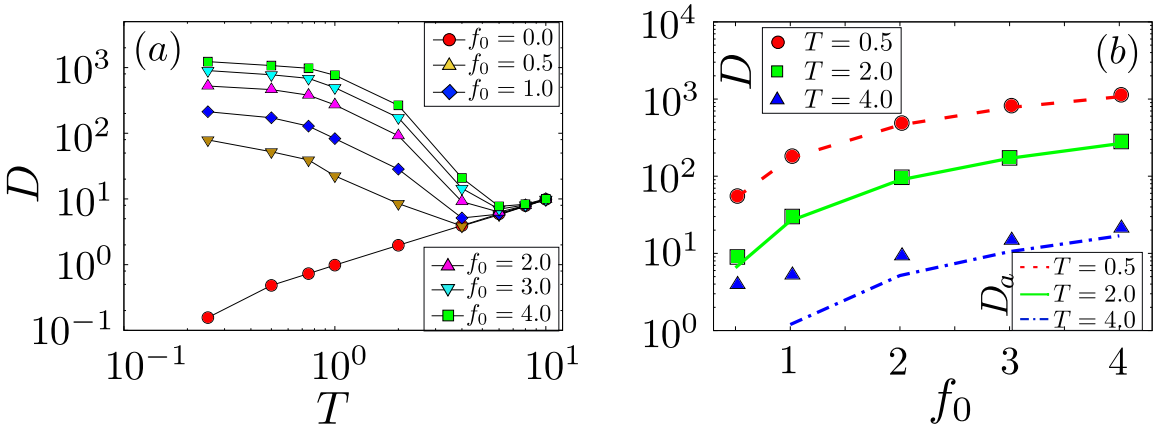

Figure 3.13 (a) Diffusion coefficient (D) of tagged passive particles has been plotted as a function of T for different values of f_0 of the filaments. At low temperature regime D is weakly dependent on T (signature of *'active diffusion'*). At intermediate regime D decreases then again increases at high temperature regime where thermal diffusion dominates. (b) We have plotted total diffusion coefficient D (with points) and *active diffusion coefficient* D_a (with line) with f_0 for different T. In the low temperature and high activity regime the difference between D and D_a is insignificant, as we increase T and decrease f_0 the difference becomes prominent.

From the stationary process, Eq. (3.13), the MSD of the tagged passive particle,

$$\langle\delta\mathbf{r}^2(t)\rangle = \int_0^t\int_0^t\langle\mathbf{V}(t')\cdot\mathbf{V}(t'')\rangle dt'dt'', \tag{3.18}$$

immediately gives the diffusion coefficient,

$$D = \frac{1}{2}\int_0^\infty \langle \mathbf{V}(t)\cdot\mathbf{V}(0)\rangle dt. \tag{3.19}$$

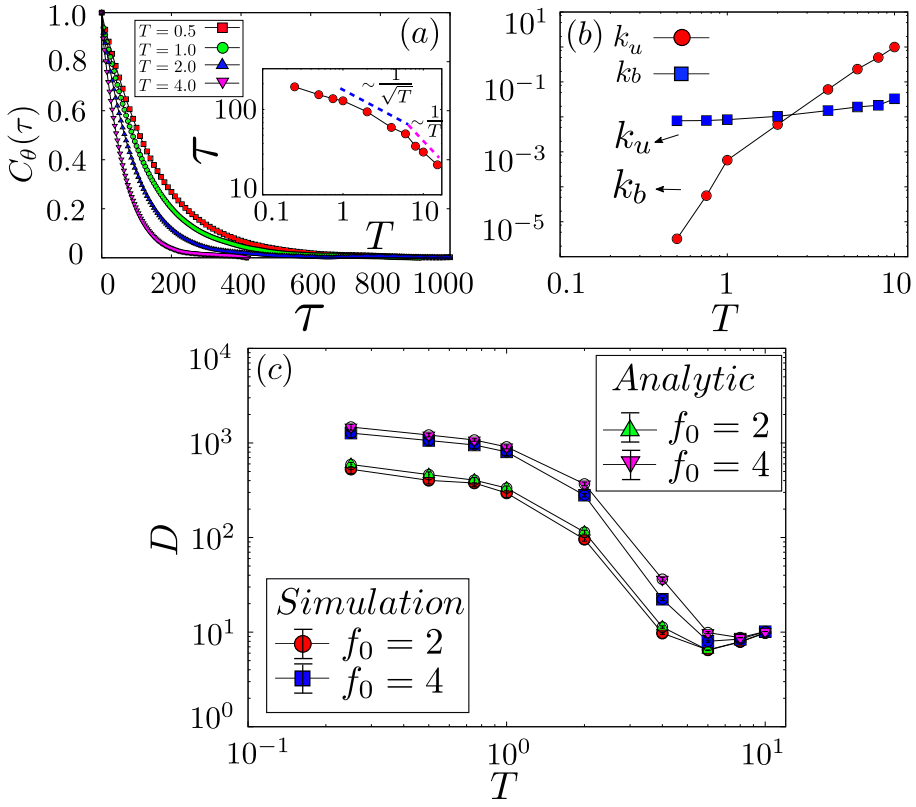

Figure 3.14 (a) Temporal correlation of the direction of persistent movement of the filaments, measured by the velocity orientation correlation function $C_\theta(t)$, at different temperatures, with the filament density $c = 0.01$ and propulsion force $f_0 = 4$. Inset shows the corresponding orientation correlation time τ as a function of T . (b) Temperature dependence of binding (k_b) and unbinding (k_u) rates calculated from the statistics of the telegraphic noise $\phi(t)$. (c) Both simulation and analytic calculation of diffusion coefficient (D) of tagged passive particles are plotted as a function of temperature (T) for two different activities ($f_0 = 2, 4$) for filament density $c = 0.01$. Data displayed with standard deviations over 16 independent realisations. Note that the standard deviation in the analytic graph is because we have used the values of τ, k_u and k_b from simulations.

Using Eq. (3.14), we see that the diffusion coefficient of the bound particle is given by the correlations of $\mathbf{V}_a$, which is given by (Fig. 3.14(a)),

$$\begin{aligned}\langle \mathbf{V}_a(t) \cdot \mathbf{V}_a(0) \rangle &= \frac{f_0^2}{\gamma_p^2} \langle \cos(\theta(t) - \theta(0)) \rangle \\ &= \frac{f_0^2}{\gamma_p^2} e^{-|t|/\tau} \end{aligned} \tag{3.20}$$

The diffusion coefficient can now be simply evaluated,

$$D = \frac{f_0^2 \tau k_b (\tau k_b + 1)}{2\gamma_p^2 (k_u + k_b)[(k_u + k_b)\tau + 1]} + \frac{k_B T k_u}{\gamma_p (k_u + k_b)} \tag{3.21}$$

To plot D versus T and f_0, we need to know the values of k_b, k_u (equivalently $\langle \phi \rangle$, t_{sw}) and τ, which depend on the temperature and density, and which we obtain from our simulations. We then compare this semi-analytical form to the direct numerical computation of the diffusion coefficient from the Brownian dynamics trajectories (Fig. 3.14). The agreement between the two is excellent. Our computations recapitulate *in vivo* observations (see Fig. 3.12) of the temperature insensitivity of diffusion coefficient of a variety of passive molecules driven by actomyosin flows at the cell surface, using fluorescence correlation spectroscopy (FCS) [4].

It might be objected that in our analysis we have treated the active propulsion as an independently tunable parameter, thus precluding the possibility that the activity itself may be temperature dependent. However, as we saw in [2], and as noted elsewhere [21, 22], the actomyosin contractile processes taken as a whole, appear to be independent of temperature in the physiological range, $24° - 37°$C.

Figure 3.15 shows the dependence of D on filament concentration c, both from direct simulations and from the analytical form using the values of k_b, k_u (equivalently $\langle \phi \rangle$, t_{sw}) and τ, from simulations. This shows optimal transport at a specific filament concentration; the orientational decorrelation time is smaller at higher filament concentration, due to higher collision frequency.

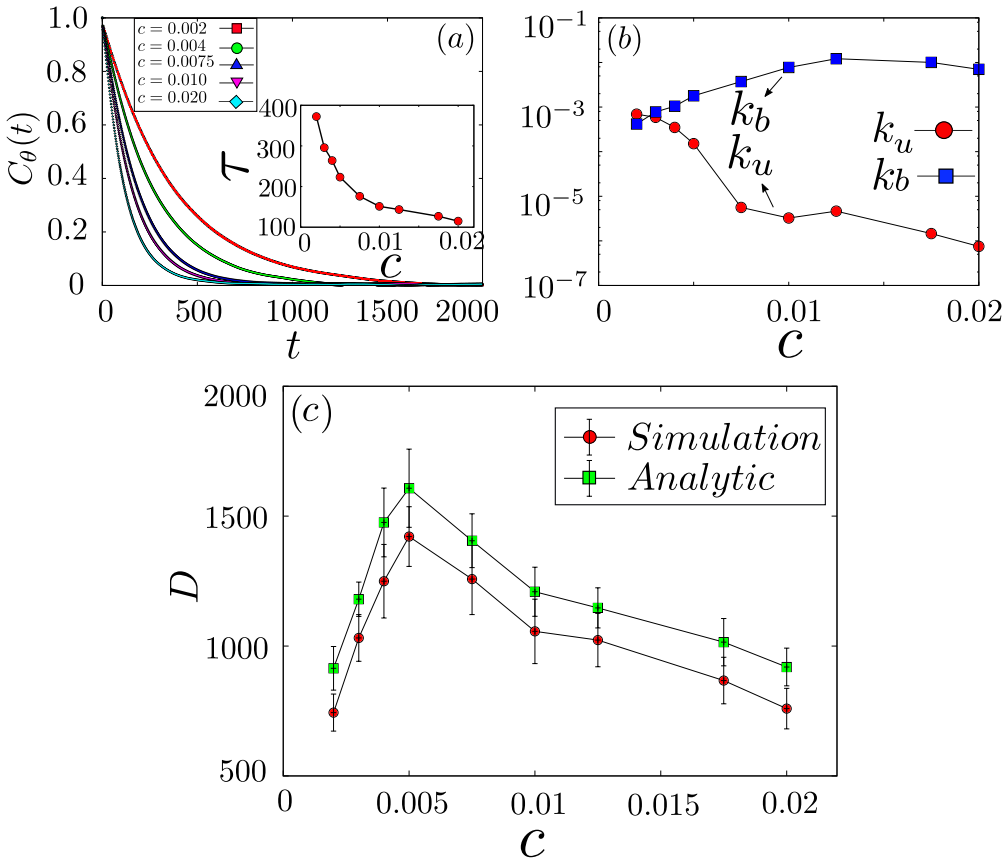

Figure 3.15 (a) Temporal correlation of the direction of persistent movement of the filaments, measured by the velocity orientation correlation function $C_\theta(t)$, with different filament density (c), at temperature $T = 0.5$ and propulsion force $f_0 = 4$. Inset shows the corresponding orientation correlation time τ as a function of c. (b) Dependence of binding (k_b) and unbinding (k_u) rates on filament density c, calculated from the statistics of the telegraphic noise $\phi(t)$. (c) Both, simulation and analytic calculation of diffusion coefficient (D) of tagged passive particles has been plotted as a function of filament density (c) at $T = 0.5$ and for $f_0 = 4$. Data displayed with standard deviations over 16 independent realisations. Note that the standard deviation in the analytic graph is because we have used the values of τ, k_u and k_b from simulations.

3.5 Viscosity stratification and its effect on membrane diffusion

So far, our study of transport of passive molecules in an active medium has been restricted to two dimensions. However as we discussed in Sect. I, the cell surface

is a composite of a bilayer membrane and a thin actomyosin cortex. Thus while the proteins move on the cell membrane, the actively driven actin moves in the actomyosin cortex. The viscosities of these two layers are significantly different, with the bilayer membrane having a viscosity which is an order of magnitude larger than the cortex ($\approx 0.86\,\mathrm{Pa\,s}$ [13]). Indeed the local viscosity of a multicomponent membrane can be quite heterogeneous - for instance the particle mobility within the so-called "membrane rafts" or liquid-ordered regions on the cell membrane can be very different from those within liquid-disordered regions. Moreover the local cortical viscosity depends on local actin, myosin and cross-linker concentrations. How does this viscosity mismatch affect the actively driven transport of passive molecules?

To address this important issue within our simulation, we vary the ratio of the friction coefficients $\Gamma = \gamma_p/\gamma_b$ in Eqs. 5.3, 3.4. We find that the mean fraction of passive particles bound to filaments $\langle n_b \rangle$ decreases with increasing Γ over a range of T and $f_0 = 4.0$ (Fig. 3.16(a)). This is an interesting observation, since one might have naively thought that $\langle n_b \rangle$ is solely governed by binding-unbinding, a purely equilibrium process and hence independent of relative viscosities. However, we see that the drag induced by the imposed viscosity stratification (a nonequilibrium feature), can "peel-off" particles from the filaments. It is not clear to us why we see a shoulder at intermediate values of Γ for low enough temperatures (Fig. 3.16(a)).

This is reflected in changes that we observe in the measured diffusion coefficient D, as it decreases with increasing Γ at different T (Fig. 3.16(b)). As can be seen, the active-diffusion regime at low temperatures becomes significantly more temperature dependent as the viscosity mismatch Γ increases.

The results of this section are not purely academic, on the contrary taken together they pose an interesting possibility that by tuning local viscosity mismatch, for instance by locally recruiting the so-called "membrane rafts" or liquid-ordered regions on the cell membrane or by locally regulating the concentrations of actin, myosin or cross-linkers, the living cell surface could control the clustering and transport of specific membrane proteins.

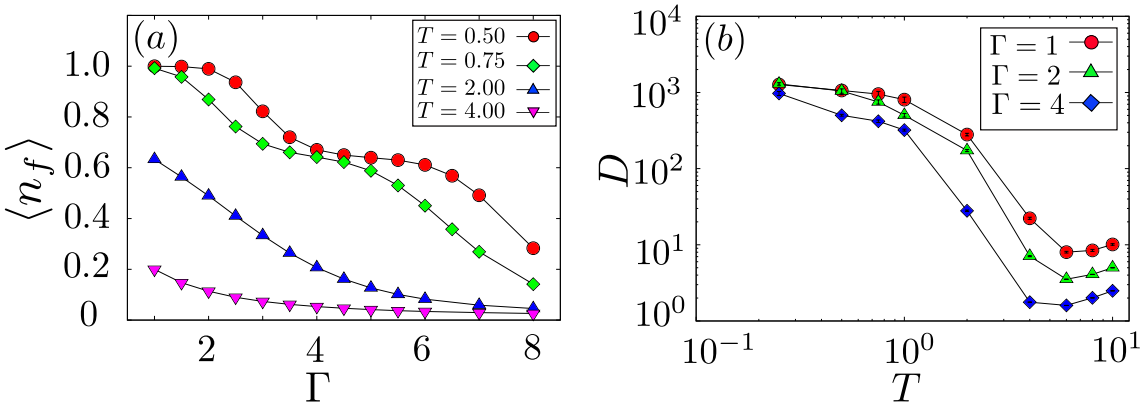

Figure 3.16 (a) Fraction of bound particles $\langle n_b \rangle$ decreases with $\Gamma = \gamma_p/\gamma_b$ over a range of temperatures. (b) Diffusion coefficient versus temperature at different values of viscosity mismatch parameter Γ. In both figures, the propulsion force has been fixed at $f_0 = 4.0$.

3.6 Discussion

We had earlier shown that a coarse grained active hydrodynamics description of the active composite cell surface, successfully explains the statistics of clustering of membrane proteins capable of binding to the cortical actomyosin in living cells [1, 3]. Such a description make predictions regarding the statistics of density fluctuations and transport of such actin-binding membrane proteins, which were verified in experiments [3, 4]. Following this we were able to recapitulate much of this behaviour in a minimal *in vitro* system comprising a thin layer of short actin filaments and Myosin-II minifilaments on a supported bilayer [7]. The success of this approach has motivated us to do an agent-based Brownian dynamics simulation using these minimal ingredients - that of a collection of passive molecules which bind/unbind to actin filaments and move in this active medium in two dimensions.

The results obtained here, based on simulations and analytical calculations, are in qualitative agreement with the experiments both *in vivo* and *in vitro*. For instance, the exponential tails appearing in the probability distribution of the number (Fig. 3.7) and the scaling of the variance of the number (Fig. 3.8) is precisely the behaviour seen in our earlier *in vitro* experiments. In addition, we show how activity induced clustering of passive particles (Fig. 3.6) arises naturally from such a minimal description.

We have also studied transport of passive particles moving in this active medium, and find that there is a crossover from an intermediate time super diffusive to late time diffusive behaviour as a consequence of active driving (Fig. 3.11(a)). The transport behaviour shows a striking dependence on temperature and active forcing - at low temperatures the diffusion coefficient is insensitive to temperature, and crosses over to a linear temperature dependence at higher temperatures, in qualitative agreement with experiments [4].

Finally, recognising that the viscosity of the cortical layer is different from that of the membrane, we show that a friction coefficient mismatch has a strong effect on the mean number of bound particles and the diffusion coefficient. This is a consequence of the drag induced by the imposed viscosity stratification, which results in a "peeling-off" of the particles from the filaments. This opens up the possibility of local tuning of viscosity mismatch, for instance by locally recruiting the so-called "membrane rafts" or liquid-ordered regions on the cell membrane or by locally regulating the concentrations of actin, myosin or cross-linkers. This could result in yet another mechanism by which the cell surface might locally control the clustering and transport of specific membrane proteins. We hope that some of these predictions can be tested in future experiments.

References

[1] M. Rao and S. Mayor, Curr. Op. Cell Biol. **29**, 126 (2014).

[2] D. Goswami et al., Cell **135**, 18085 (2008).

[3] K. Gowrishankar, S. Ghosh, S. Saha, S. Mayor and M. Rao, Cell **149**, 1353 (2012).

[4] S. Saha, I. Lee, A. Polley, J. T. Groves, M. Rao and S. Mayor, Mol. Biol. Cell **26**, 4033 (2015).

[5] S.J. Plowman, C. Muncke, R.G. Parton and J.F. Hancock, Proc. Natl. Acad. Sci. USA **102**, 15500 (2005).

[6] D. Lingwood and K. Simons, Science **327**, 46 (2010).

[7] D.V. Koster, K. Husain, E. Iljazi, A. Bhat, P. Bieling, R.D. Mullins, M. Rao and S. Mayor, Proc. Natl. Acad. Sci. USA **113**, E1645 (2016).

[8] Y. Hatwalne, S. Ramaswamy, M. Rao, and R. A. Simha, Phys. Rev. Lett. **92**, 118101 (2004).

[9] A. Basu, J. F. Joanny, F. Julicher, and J. Prost, New J. Phys. **14**, 115001 (2012).

[10] K. Chen, B. Wang, and S. Granick, Nat. Mater. **14**, 589 (2015).

[11] Y. Yang, V. Marceau and G. Gompper, Phys. Rev. E **82**, 031904 (2010).

[12] H. H. Wensink and H. Löwen, J. Phys.: Condens. Matter **24**, 464130 (2012). H. H. Wensink, J. Dunkel, S. Heidenreich, K. Drescher, R. E. Goldstein, H. Löwen and J. M. Yeomans, Proc. Natl. Acad. Sci. USA **109**, 14308 (2012).

[13] T. C. Bidone, W. Jung, D. Maruri, C. Borau, R. D. Kamm and T. Kim, PLoS Comput Biol **13**, 1005277 (2017).

[14] D. Grebenkov, J. Phys. A **48**, 013001 (2015).

[15] N.G. Van Kampen, *Stochastic Processes in Physics and Chemistry*, 3rd Edition, North-Holland, Amsterdam (2007).

[16] J. Toner and Y. Tu, Phys. Rev. Lett. **75**, 4326 (1995).

[17] V. Narayan, S. Ramaswamy and N. Menon, Science **317**, 105 (2007).

[18] R. A. Simha, J. Toner and S. Ramaswamy, EPL **62**, 2 (2003).

[19] K. Husain, *The Mechanics of Cell Surface Clusters and their role in Signalling*, Ph.D Thesis, National Centre for Biological Sciences (Tata Institute of Fundamental Research, November 2017).

[20] X. Wu and A. Libchaber, Phys. Rev. Lett. **84**, 3017 (2000).

[21] M. P. Sheetz, R. Chasan and J. A. Spudich, J. Cell Biol. **99**, 1867-1871 (1984).

[22] H.M. Levy, N. Sharon and D. E. Koshland Jr., Proc. Natl. Acad. Sci. USA **45**, 785-791 (1959).

End of Chapter

Chapter 4

Clustering and reaction kinetics of cell surface molecules in semi-dilute active medium

4.1 Introduction

As discussed in the introduction (chapter 1), many cell membrane proteins that bind to actin, form dynamic clusters driven by contractile flows arising from actomyosin at the cell cortex. Recent evidences suggest that a necessary condition for the generation of these protein clusters on the membrane is the stratified organization of the active agents - formin-nucleated actin, myosin-II minifilaments, and ARP2/3-nucleated actin mesh - within the cortex. Further, the observation that these clusters dynamically remodel, requires that the components of this active machinery undergo turnover. In chapter 2 we developed a coarse-grained agent-based Brownian dynamics simulation that incorporates the effects of stratification, binding of *myosin minifilaments* to multiple actin filaments and their turnover. We have shown that these three features of the active cortical machinery - *stratification*, *multivalency* and *turnover* - are crucial to the attainment of a nonequilibrium steady state characterised by contractile flows and dynamic orientational patterning. The orientational patterns generated by the actin filaments driven by myosin minifilaments are isotropic, polar bundle, polar aster, aster and spiral asterFig. 2.4.

In this chapter, coupling this actomyosin dynamics to the dynamics of molecules on the two dimensional cell surface, we find that this automatically drives *multiparticle* encounters and dynamical clustering. We have studied the effect of aster phase on the dynamics of membrane molecules. We show that this steady state

enabled by the above features of the cortex, can facilitate multi-particle encounters of membrane proteins that profoundly influences the kinetics of bimolecular reactions at the cell surface. Indeed we show that inhibition of any one of the three ingredients leads to a loss of the desired phenotype. This provides the motivation to study the influence of active stresses on the dynamics of generic bimolecular chemical reactions, $A + B \rightleftharpoons C$ on the cell surface, an issue of profound biological significance [1, 2, 3, 4, 5, 6].

4.2 Dynamics of cell surface molecules driven by stratified active actomyosin cortex

The dynamics of actin filaments in the $z = 1$ layer in a stratified cortex has been described in the chapter 2. This dynamic actin filaments drives the membrane proteins that bind to it.

Membrane proteins in the $z = 0$ layer are modelled as mono-disperse soft discs of diameter σ. The dynamics of membrane proteins are determined by protein-protein interactions, interactions with the dynamic actin filaments situated in the $z = 1$ layer and thermal noise. A pair of proteins separated by a distance $r_{\alpha\beta}$ interact via a purely repulsive potential, a truncated and shifted pair potential of the form,

$$\begin{aligned} V_p(r_{\alpha\beta}) &= 4\epsilon\left(\frac{\sigma}{r_{\alpha\beta}}\right)^{12} + V_0 + V_2\, r_{\alpha\beta}^2 + V_4\, r_{\alpha\beta}^4 \quad \text{for } r_{\alpha\beta} \leq \sigma \\ &= 0 \quad \text{for } r_{\alpha\beta} > \sigma \end{aligned} \tag{4.1}$$

where the values of V_0, V_2 and V_4 are chosen so that the potential and force are continuous at the truncation point. In what follows, we set $\sigma = 1$ and $\epsilon = 1$ to be the units of length and energy, respectively.

Actin filaments in the $z = 1$ layer are represented as a string of beads, the details of the inter-bead potential will be specified later in this section. Here, we focus on its influence on the dynamics of a membrane protein in the $z = 0$ layer, which is simply that when bound to a bead belonging to an actin filament, it moves with the velocity of that filament, in a "no-slip" manner. We implement this by prescribing the net force on the α-th membrane protein in the $z = 0$ layer as,

$$\mathbf{f}_\alpha(t) = \begin{cases} \sum_{\beta\neq\alpha} \mathbf{F}^p_{\alpha\beta}(t) + \boldsymbol{\xi}^p_\alpha(t) & \text{(always)} \\ -k\,|\mathbf{r}_\alpha - \mathbf{r}_{m,i}| & \text{(applicable when the protein is} \\ & \text{bound to any bead } m \text{ of filament } i) \end{cases} \tag{4.2}$$

where $\mathbf{F}^p_{\alpha\beta}$ is the force on the α-th membrane protein due to the β-th protein calculated from Eq. 4.1, $\boldsymbol{\xi}^p_\alpha$ is the thermal noise, drawn from a Gaussian distribution with zero mean and variance $= 2k_BT\gamma_p/\Delta t$, where γ_p is the friction coefficient of the proteins in the membrane, and finally, k is the attractive spring force between the the actin filament and the protein when it is bound to it. The binding-unbinding status of each membrane protein is determined by switching rates k_b and k_u, respectively, where binding to bead m is initiated when a distance criterion $|\mathbf{r}_\alpha - \mathbf{r}_{m,i}| \leq 1.6\sigma$ is met. We vary k_u over the range $10^{-5} - 10^{-1}$, where we use γ_p to set the unit of time (see, Table 1).

With this force, the position of the α-th membrane protein gets updated by $\mathbf{v}_\alpha(t) = \mathbf{f}_\alpha(t)/\gamma_p$ in a time Δt.

4.3 Simulation details

All results presented here are for $N_p = 300$ membrane proteins and $N_a = 64$ actin filaments in a two dimensional (2d) area of linear dimension $L = 400$ with periodic boundary conditions (PBC). In our Brownian dynamics simulations runs, the time update is $\Delta t \sim 2 \times 10^{-3}$, with total run time being $t = 5 \times 10^4$. Our initial conditions are chosen from a thermal distribution at temperature $T = 1.0$, and all results presented here are averaged over 32 such independent initial realisations. We take single filament velocity $v_0 = 0.2$ coming from the active translation current. Membrane protein number density is $\rho_p = 1.8 \times 10^{-3}$ and actin filament number density is $\rho_a = 4 \times 10^{-4}$. We studied the clustering of molecules with all same type of membrane proteins and while studying chemical kinetics we took two type of proteins with equal numbers where $N_A = N_B = 150$. The membrane proteins can bind and unbind to the beads of the filament with rate k_b and k_u, respectively. When a membrane protein comes within a distance $l_{bp} = 0.8\sigma_b$ from the centre of

a filament bead, it binds to the corresponding bead with rate k_b and gets advected along with the filament. The attractive interactions between the filament beads and the membrane protein are modelled by a harmonic potential with spring constant $k_{bp} = 100$. The bound particle unbinds from the filament with rate k_u.

We study the role of particle attachment to the filament (k_u) and filament turnover rate (k_r) on clustering and chemical kinetics. We take binding rate $k_b = 0.5$. We have varied unbinding rate k_u over the range $10^{-5} - 10^{-1}$ and turnover rate k_r over the range $10^{-4} - 10^{-1}$. In chemical kinetics study the association rate $k_a = 0.004$ and the dissociation rate $k_d = 10^{-4}$.

Throughout our simulation, the units of length, time and energy are set by σ, γ_p and ϵ (Table 4.1). All other parameters expressed in natural units are listed in Table. 4.2 for convenience.

Table 4.1 Natural units - simulation units (S.U.) and real units (R.U.)

Natural Units	Symbol [Dimension]	S.U.	R.U.
Length (Membrane protein diameter)	σ $[l]$	1	10 nm
Energy (Inter-protein interaction)	ϵ	1	4.11×10^{-21} J
Membrane protein friction coefficient	γ_p	10	0.8 $pN\mu m^{-1}s$
Time	$t = l^2\gamma_p/10\epsilon$	1	2×10^{-3} s

Table 4.2 Other parameters expressed in natural units and their ranges

Parameters	Symbol [Dimension]	Value/Range
Membrane protein diffusion constant	D $[l^2t^{-1}]$	0.1
Physiological Temperature	T $[\epsilon]$	1
Actin filament bead diameter	σ_b $[l]$	1.6
Actin filament length	l $[l]$	24
Single actin filament propulsion velocity	v_0 $[lt^{-1}]$	0.2
2-filament torsional spring stiffness	k_θ $[\epsilon]$	5
Multi-filament torsional spring stiffness	k_ϕ $[\epsilon]$	500
2-filament extensional spring stiffness	k_2 $[\epsilon l^{-2}]$	10
Multi-filament extensional spring stiffness	k_3 $[\epsilon l^{-2}]$	5
Turnover rate of actin filaments	k_r $[t^{-1}]$	$10^{-1} - 10^{-4}$
Binding rate of protein to actin filament	k_b $[l^2t^{-1}]$	0.5
Unbinding rate of protein from actin filament	k_u $[t^{-1}]$	$10^{-1} - 10^{-5}$
Association rate of bimolecular reaction	k_a $[l^2t^{-1}]$	0.004
Disassociation rate of bimolecular reaction	k_d $[t^{-1}]$	10^{-4}

4.4 Activity enhances multi-particle encounters

Having described the orientational patterning and nonequilibrium dynamics of actin filaments driven by Myo-II minifilaments, we ask how these might affect the dynamics of membrane proteins in the $z = 0$ layer of the stratified active composite surface. From the combined active dynamics of the actin filaments and membrane proteins interacting with actin (Eqs. 4.2, 2.2), we see that the contractile flows generated by the active forces and torques on single and multiple actin filaments, draw in the bound membrane proteins. Following this, the membrane proteins may unbind from the filaments, resulting locally in high concentrations of free proteins that can engage in multiple binary and multiparticle encounters with each other. This is best seen in the Aster phase of Fig. 2.4.

Results of Turnover and Multivalency of actin filaments:

To quantify the extent of multi-particle encounters, we compute both the number of clusters of size k and their lifetimes. Figure 4.1 shows the average number of clusters of size k, denoted as $\langle n_k \rangle$, that appear within a time window (here, we take it to be 10^3) at steady state. (Note that to define a cluster, we need a inter-particle distance cutoff, which we take to be $1.2\,\sigma$). In the equilibrium limit, obtained by setting the binding of membrane proteins to the active actin filaments to zero, we see that thermal motion alone leads to transient clusters that are predominantly dimers ($k = 2$) and rarely trimers or higher k-mers ($k \geq 3$). This is in striking contrast to the active steady state with turnover, which shows a significant fraction of large clusters (k up to 10, as seen in Fig. 4.1.

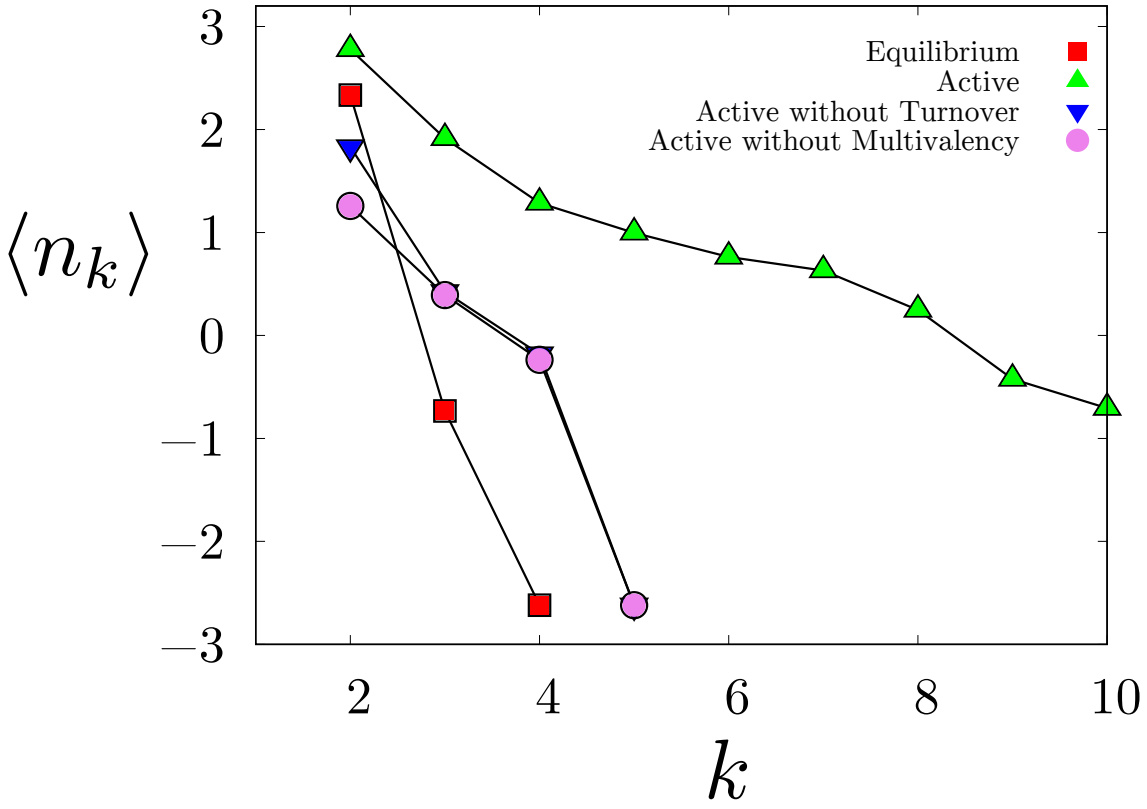

Figure 4.1 Activity and turnover enhance multiparticle encounters. (a) Mean number of k-clusters, $\langle n_k \rangle$ versus with cluster size k (y-axis in $\log_{10}$ scale). Observe the enhancement of the number of large clusters in the active case with both turnover and multivalency (green triangle), compared to the equilibrium limit (red square). Abrogation of turnover (blue triangle) or multivalency (purple circle) leads to a significant reduction in the number.

We emphasize that these multiparticle encounters are realised only in the active nonequilibrium steady state, which is contingent on stratification, turnover and multivalency of force generators. Significantly, when we abrogate either turnover ($k_r = 0$) or multivalency ($k_3 = k_\phi = 0$), we loose the larger clusters.

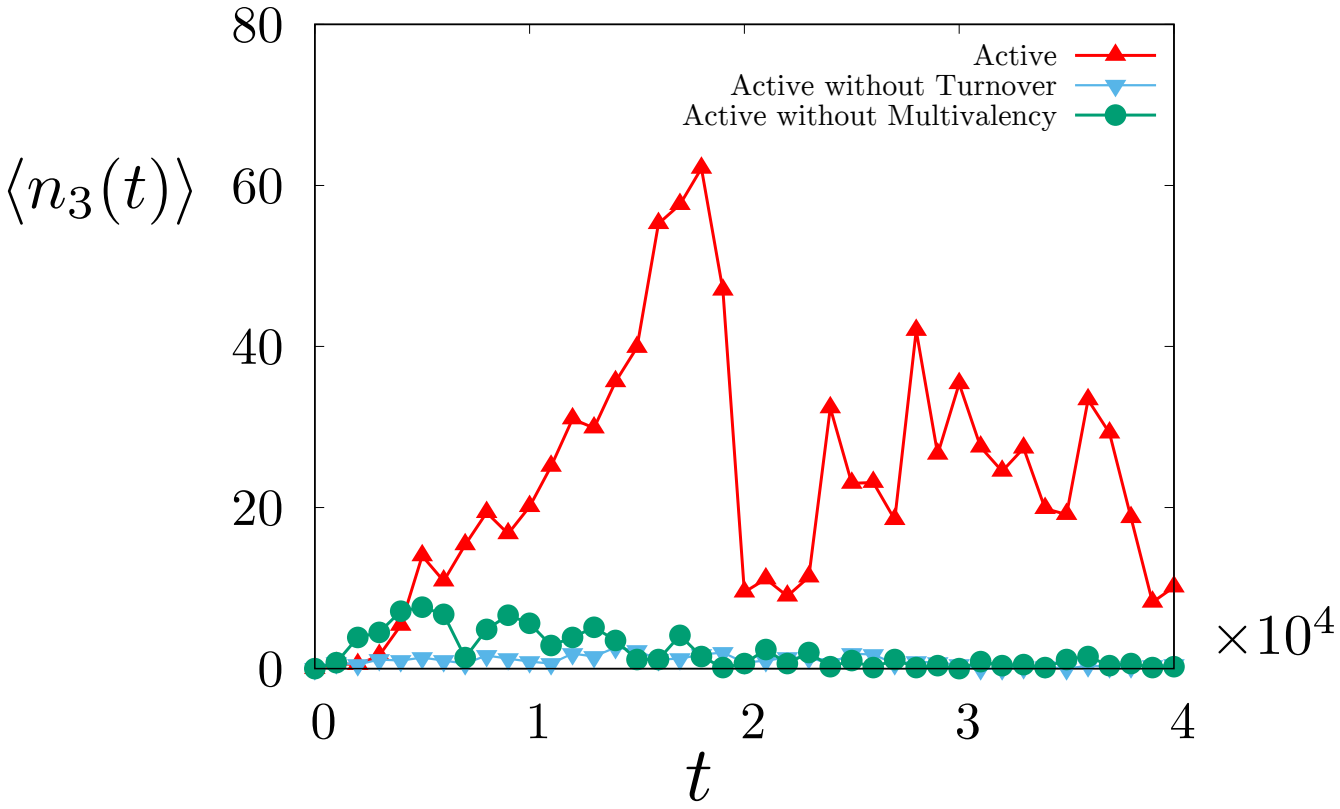

Figure 4.2 Time series of 3-particle clustering (mean number of 3-clusters, $\langle n_3 \rangle$) shows large intermittent fluctuations of $\langle n_3(t) \rangle$ in the active system with turnover and multivalency, which is dramatically suppressed in the absence of turnover or multivalency.

Figure 4.2 shows the time series of the number of 3-particle clusters $\langle n_3(t) \rangle$ (within a time window τ_r) in the nonequilibrium steady state (red). The large temporal fluctuations of $\langle n_3(t) \rangle$ are suppressed in the absence of turnover and multivalency of the active force generators. These results, namely the presence of large and transient clusters in the nonequilibrium steady state is contingent on stratification, turnover and multivalency and is in agreement with recent experiments on reconstituted actomyosin on a supported bilayer [7].

Variation with unbinding rate and turnover rate: In addition, we make sev-

eral qualitative predictions that can be tested in carefully engineered in-vitro experiments. For instance, in Fig. 4.2(a), we find that $\langle n_k \rangle$ increases upon reducing the unbinding rate associated with the interaction of the membrane protein with filamentous actin, keeping the turnover rate k_r fixed. Further, $\langle n_k \rangle$ shows a non-monotonic dependence on the turnover rate k_r, keeping the unbinding rate k_u fixed (Fig. 4.3.

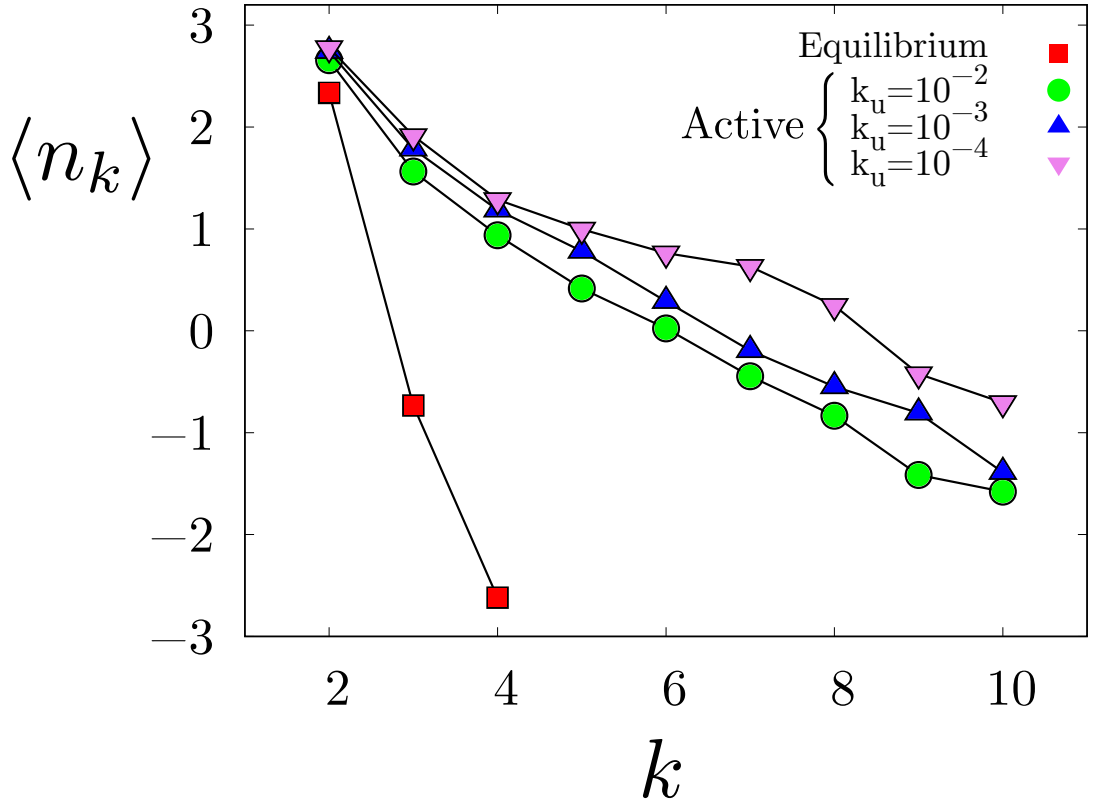

Figure 4.3 Mean number of k-clusters, $\langle n_k \rangle$ versus with cluster size k (y-axis in log10 scale). Observe the enhancement of the number of large clusters in the active case. Lower unbinding rate enhance multiparticle encounters.

In the nonequilibrium steady state, the number of $k-$clusters shows the same intermittent dynamics as mean aster density. Figure 4.2 shows the time series of the number of 3-clusters $\langle n_3(t) \rangle$ in the nonequilibrium steady state. The large temporal fluctuations of $\langle n_3(t) \rangle$ are suppressed in the absence of turnover and multivalency of the active force generators. Interestingly, $\langle n_k \rangle$ shows a non-monotonic dependence on the turnover rate k_r (Fig. 4.4 a prediction that can be tested in reconstitution experiments, such as [7].

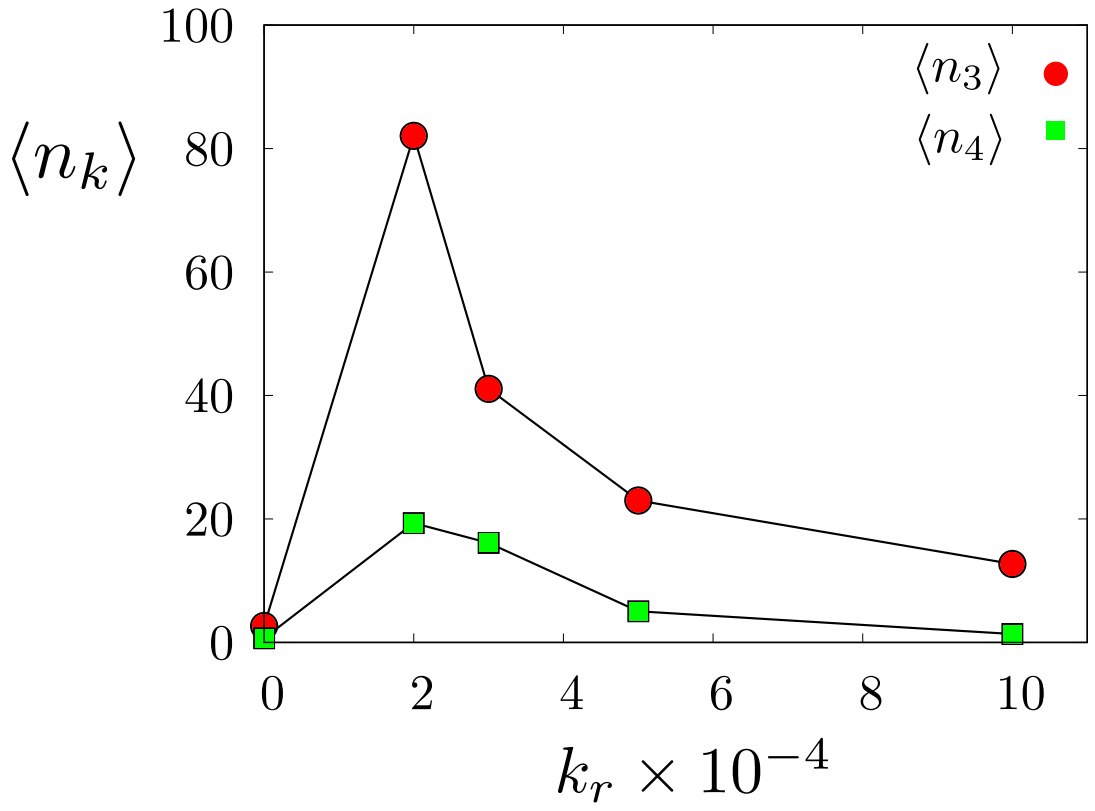

Figure 4.4 Mean number of k-clusters $\langle n_k \rangle$ for $k = 3$ (red circle) and $k = 4$ (green square) shows non-monotonic behaviour with filament turnover rate k_r.

To summarize, the formation of large and intermittent clusters in the nonequilibrium steady state is contingent on stratification, turnover and multivalency, in agreement with experiments on reconstituted actomyosin on a supported bilayer [7].

4.5 Activity influences chemical reaction kinetics at the cell surface

Since many signalling molecules at the cell surface interact with cortical actin, it is reasonable that most biochemical reactions on the cell membrane are strongly influenced by the actomyosin cortex. For instance, there have been proposals that trapping of membrane proteins by the cortical actin mesh underlying the cell membrane can lead to enhancement of reaction kinetics [3, 4, 5, 8, 9, 10, 11]. Since in these models there is no dynamical feedback between the chemical reactants and

the cortical mesh, there is no mechanism by which spatiotemporal control and regulation can be effected. Our observation that multi-particle encounters of membrane proteins are more frequent when they are driven by active forces and torques, together with turnover of the active machinery, suggests an additional mechanism for enhancement of chemical reaction kinetics along with its spatiotemporal regulation [6].

To fix ideas, let us consider a reversible bimolecular reaction between two membrane protein species A and B reacting to form a complex C, $A + B \underset{k_b}{\overset{k_f}{\rightleftharpoons}} C$, where k_f and k_b are the effective forward and backward reaction rates, respectively. For the forward reaction to be realised, the A and B proteins need to first diffuse towards each other, close enough (we take the scale of this reaction zone to be $1.2\,\sigma$), so as to engage in a chemical bonding, and then associate to form C with a rate k_a modelled as a Poisson process. The effective backward reaction, involves a chemical dissociation of the complex C with a rate k_d modelled as a Poisson process and a subsequent escape of the products A and B from the reaction zone. Note that the individual chemical reactions are equilibrium processes, the only role that activity plays in these chemical reactions is in creating situations where the local reactant density is high.

The fraction of C proteins $c(t) = 2N_C(t)/N$, starting from an equal number of A and B proteins, appears to grows as $c(t) = c^*\left(1 - e^{-\frac{t}{\tau}}\right)$, even in the nonequilibrium steady state, simulated for different values of k_u and turnover rate $k_r > 0$ (see, Fig. 4.5(a-d)). This form is exactly what one would expect for a mass action bimolecular reaction,

$$\frac{d\rho_C(t)}{dt} = k_f\ \rho_A(t)\rho_B(t) - k_b\ \rho_C(t) \tag{4.3}$$

where, $\rho_A(t)$, $\rho_B(t)$ and $\rho_C(t)$ are the number density of A, B and C molecules, respectively. This is reinforced by constructing a scaling plot over a range of values of k_u (Fig. 4.5(c)) using the extracted parametric dependence of c^* and τ with k_u (Fig. 4.5(b)).

From Fig. 4.5(a,b), we see that the reaction yield c^* is significantly larger in the nonequilibrium steady state with active driving and turnover compared to its value at equilibrium and shows a strong dependence on actin binding affinity k_u of the

reactants. Further, the reaction proceeds faster as seen in the plot of the reaction time τ (Fig. 4.5(b)).

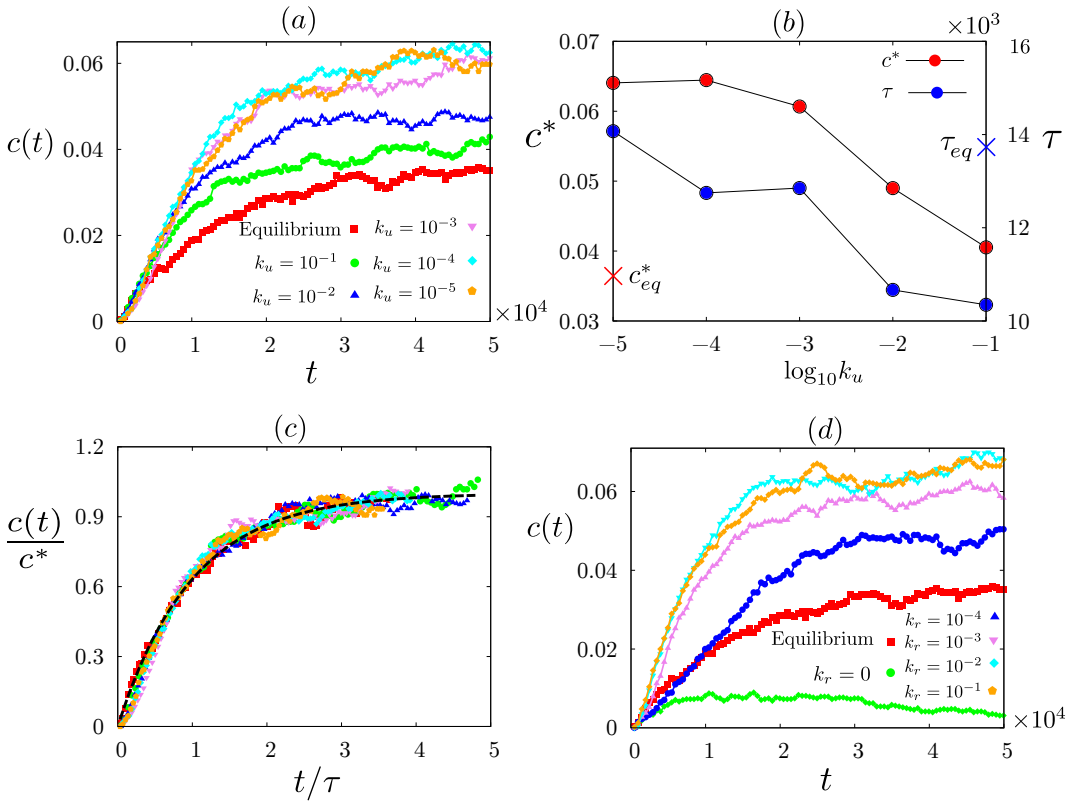

Figure 4.5 (a) The fraction of C proteins $c(t)$ increases with time as the bimolecular reaction proceeds; in the nonequilibrium steady state with contractile flows and turnover, both the reaction yield and net reaction speed, increase with increasing actin binding affinity (or decreasing unbinding rate k_u), keeping the turnover rate at $k_r = 5 \times 10^{-4}$. (b) Reaction yield c^*, obtained from the saturation concentration, and the net reaction time τ, obtained from the initial slope of the growth curve, decrease with unbinding rate. For reference, we display the value of c^* and τ for the equilibrium reaction. (c) Using the extracted values of c^* and τ, we display a scaling collapse of all the data with different values of k_u. The dashed line in (c) is the scaling curve $(1-e^{-\frac{t}{\tau}})$. (d) The fraction of C proteins $c(t)$ in the nonequilibrium steady state versus time for different turnover rates k_r keeping the protein unbinding rate fixed $k_u = 10^{-4}$. The reaction yield c^* increases with increasing turnover rate k_r, and is higher than the equilibrium reaction. One expects the reaction yield to start *decreasing* when $k_r \gg k_u$. Note that without turnover ($k_r = 0$), the reaction yield is extremely small. Throughout this panel, we have fixed the torsional spring stiffness $k_\theta = 5$, $k_\phi = 500$, binding rate $k_b = 0.5$, association rate $k_a = 4 \times 10^{-3}$ and disassociation rate $k_d = 10^{-4}$.

In general, this is due to a combination of faster advective transport and enhancement in the local concentration of reactants as a consequence of a larger binding affinity to actin and the active contractile flows. In Fig. 4.5, since the values of the reactin parameters are such that $k_a/D < 0.05$, the chemical reactions are largely association rate limited [12], and so the dominant mechanism for .

We see that fixing the binding affinity, the reaction yield increases with increasing turnover rate. This is due to the combination of stochastic active contractile flows and turnover in the nonequilibrium steady state, and can be thought of as contributing to both an enhanced (active) temperature and an increase in local concentration of reactants. Note that when the turnover is switched off and the actin asters are static, there is very little increase in the of the reaction yield Fig. 4.5(d).

In chapter 2 Fig. 2.5, the orientation patterns in the actomyosin cortex show intermittent behaviour characteristic of nonequilibrium dynamics. Here, we study the statistics of the reaction event of membrane molecules. In an active system, when the membrane molecules are coupled to the actomyosin cortex, we see intermittent behaviour in the time series of the number of reaction events (n_e) over a small time window inside a small area ($\frac{L}{5} \times \frac{L}{5}$) (see Figure. 4.6). This intermittent behaviour is not present in the equilibrium system. This kind of intermittent reaction event is referred to as 'burst reaction', which plays a role in cell signalling. Proteins in the cell membrane receive information from the environment and trigger signalling pathways inside the cell in the signalling process. A common mechanism to reduce the signal to noise ratio would be to digitalised the input signals. Clustering of receptor molecules and bursty reaction offer a general way to digitalised analogue input signals. The spike in the number of the same type of molecule provides a discrete switch-like output because of its short lifetime.

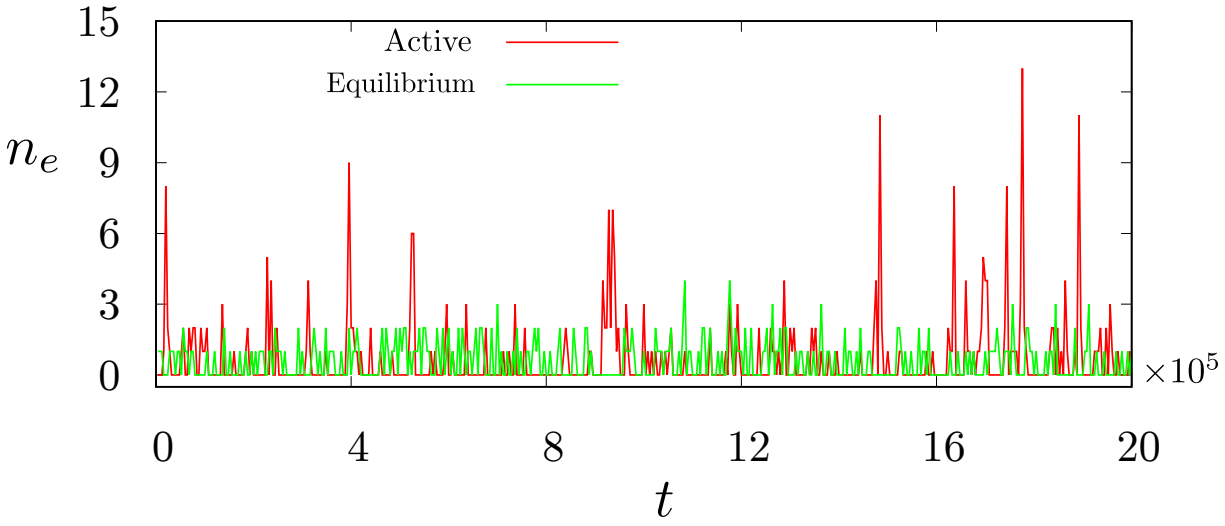

Figure 4.6 The time series of the number of reaction events (n_e) over a small time window inside a small area $\frac{L}{5} \times \frac{L}{5}$. This shows large fluctuations in active system compared to the equilibrium system. We have fixed the torsional spring stiffness $k_\theta = 5$, $k_\phi = 500$, binding rate $k_b = 0.5$, unbinding rate $k_u = 10^{-4}$, association rate $k_a = 10^{-2}$, disassociation rate $k_d = 10^{-4}$ and turnover rate $k_r = 2 \times 10^{-4}$.

we have seen nonequilibrium dynamics in the orientational patterns, such as asters, show intermittent fluctuations. Here, we show that due to the coupling of membrane molecules to the actomyosin cortex, the number of reaction events (n_e) over a small time window inside a small area ($\frac{L}{5} \times \frac{L}{5}$) shows bursty reaction Fig. 4.6.

4.6 Discussion

In this chapter, we have studied the dynamics of membrane molecules using the coarse grained agent based simulation model of a stratified active composite of a membrane, comprising lipids and proteins, juxtaposed with an active actomyosin layer developed in chapter 2. We show that this simple coarse grained model, that incorporates the fluctuating active forces and torques in a stratified geometry, recapitulates the nonequilibrium steady states observed both *in vivo* [13, 14, 15, 16, 17, 18, 19] and in properly designed reconstitution experiments [7, 20, 21, 22]. By coupling this actomyosin dynamics to the dynamics of molecules on the two dimensional membrane bilayer, we find that this automatically drives *multiparticle* encounters and

dynamical clustering. We show that these multiparticle encounters are realised only in the active nonequilibrium steady state, which is contingent on stratification, turnover and multivalency of force generators. Significantly, when we abrogate either turnover or multivalency , we loose the larger clusters. Mean number of multiparticle cluster shows non-monotonic behaviour with filament turnover rate. We have studied the dynamics of generic bimolecular chemical reactions, $A + B \rightleftharpoons C$ on the cell surface [6]. In the nonequilibrium steady state with contractile flows and turnover, both the reaction yield and net reaction speed, increase with increasing actin binding affinity. The model describe here, can be be easily extended to address a variety of relevant physical situations, such as an extension to multicomponent bilayer capable of phase segregation [23].

References

[1] B.N. Kholodenko, Nat. Rev. Mol. Cell Biol. **7**, 165-176 (2006).

[2] P. Rangamani and R. Iyengar, J Biosci **32**, 157 (2007).

[3] J. M. Haugh, D. A. Lauffenburger, Biophys. J. **72**, 2014–2031 (1997).

[4] C. Loverdo, O. Bénichou, M. Moreau and R. Voituriez, Nature Phys. **4**, 134 (2008).

[5] J. S. van Zon and P. R. ten Wolde, J. Chem. Phys., **123**, 234910 (2005).

[6] A. Chaudhuri, B. Bhattacharya, K. Gowrishankar, S. Mayor, and M. Rao, Proceedings of the National Academy of Sciences **108**, 14825 (2011).

[7] D. V. Köster, K. Husain, E. Iljazi, A. Bhat, P. Bieling, R. D. Mullins, M. Rao, and S. Mayor, Proceedings of the National Academy of Sciences **113**, E1645 (2016).

[8] O. Benichou, C. Loverdo, M. Moreau, and R. Voituriez, Rev. Mod. Phys. **83**, 81 (2011).

[9] Z. Kalay, Biotechnol. J. **7**, 745–752 (2012).

[10] Z. Kalay, T. K. Fujiwara and A. Kusumi, PLoS ONE **7** e32948 (2012).

[11] O. N. Yogurtcu and M. E. Johnson, J. Chem. Phys. **143**, 084117 (2015).

[12] N. Agmon and A. Szabo, The Journal of Chemical Physics **92**, 5270 (1990).

[13] M. Rao and S. Mayor, Curr. Opin. in Cell Biol. **29**, 126 (2014).

[14] D. Goswami, K. Gowrishankar, S. Bilgrami, S. Ghosh, R. Raghupathy, R. Chadda, R. Vishwakarma, M. Rao and S. Mayor, Cell **135**, 1085 (2008).

[15] K. Gowrishankar, S. Ghosh, S. Saha, C. Rumamol, S. Mayor and M. Rao, Cell **149**, 1353 (2012).

[16] M. Guha, M. Zhou, and Y. L. Wang, Curr. Biol. **15**, 732-736 (2005).

[17] N. A. Medeiros, D. T. Burnette and P. Forscher, Nat. Cell Biol. **8**, 216-226 (2006).

[18] E. M. Reichl, Y. Ren, M. K. Morphew, M. Delannoy, J. C. Effler, K. D. Girard, D. Srikanth, A. I. Pablo, C Kuo Scot and N. R. Douglas, Curr. Biol. **18**, 471–480 (2008).

[19] Q. Yang, X. F. Zhang, T. D. Pollard and P. Forscher, J. Cell Biol. **197**, 939-956 (2012).

[20] Sonal, K. A. Ganzinger, S. K. Vogel, J. Mu cksch, P. Blumhardt and P. Schwille, Journal of Cell Science **132**, 219899 (2019).

[21] T. Han Tan, M. Malik-Garbi, E. Abu-Shah, J. Li, A. Sharma, F. C. MacKintosh, K. Keren, C. F. Schmidt, N. Fakhri, Science Advances **4**, 2847, (2018).

[22] A. Das, A. Bhat, R. Sknepnek, D. Koster, S. Mayor and M. Rao, Sci. Adv. **6**, 11, (2020).

[23] S. Saha, A. Das, C. Patra, S. Mayor and M. Rao, in preparation (2021).

End of Chapter

Chapter 5

Membrane-Cortex composite as a Random Field Active Glass with line-disorder

5.1 Introduction and Motivation

In 1972, Singer and Nicholson [1] presented the classic fluid mosaic model. According to this model, the lipid bilayer is in a fluid state, and proteins freely diffuse in the membrane, presumably undergoing simple Brownian motion. Single particle tracking experiments at low frame rates (up to 65 Hz) that capture only the long time behaviour of the trajectory supports this simple Brownian motion dynamics of membrane molecules [2, 3].

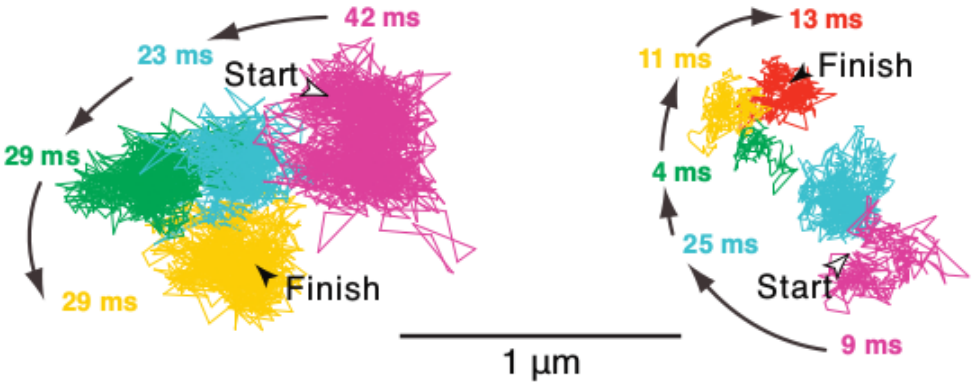

Figure 5.1 The trajectory of a transmembrane protein (left) and a lipid molecule (right) with 25 μs time resolution. The residency time in each compartment is indicated (Image Courtesy : [6]).

Recent studies of membrane molecules dynamics using high-speed single-particle

tracking (SPT) camera at 50 kHz (25 μs time resolution) have revealed that membrane molecules undergo short-term confined diffusion within a cage followed by long-term hop-diffusion(Figure. 5.1) between compartments [4, 5, 6, 7, 8]. This SPT experiments with 25 μs time resolution camera can capture the few millisecond residency time in a compartment before it hops to another. Also, the mean square displacement of the molecules shows anomalous sub-diffusion [6]. The diffusion constant of lipids in the cell is $20 - 50$ folds smaller than that seen in an artificial membrane, and this was a profound puzzle till these observations of confined diffusion in the cell came from the SPT experiments [4].

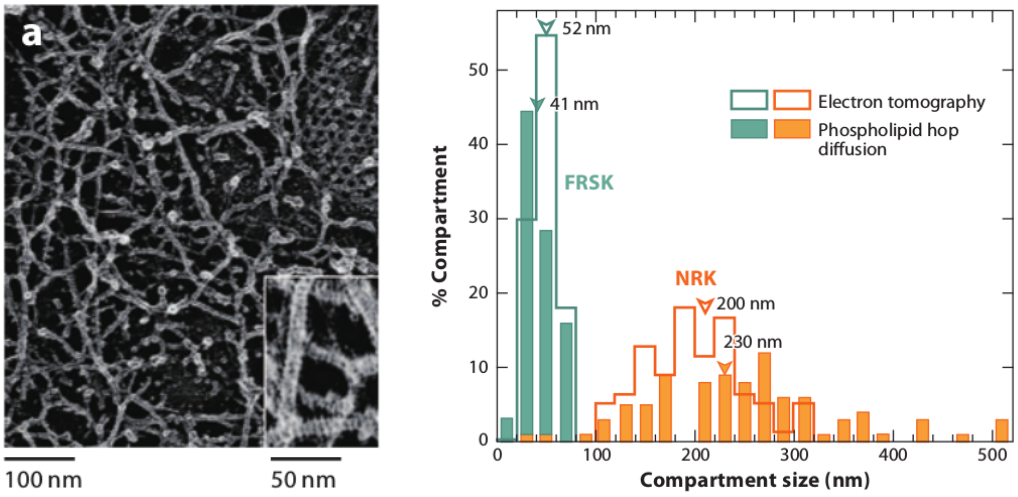

Figure 5.2 (a)Electron microscopic image of the membrane skeleton (MSK) of a fetal rat skin ketatinocyte (FRSK) cell. (b) A comparison of the distribution of the MSK mesh size measured by electron tomography (open bars) with that of the compartment size determined from phospholipid diffusion data (closed bars) for normal rat kidney (NRK, orange) and FRSK (green) cell lines. The MSK mesh size and the diffusion compartment size had identical distributions within the same cell type (compare the open and closed bars with the same colour)(Image Courtesy: [7]).

Recent experimental studies [4, 5, 6] have revealed that the lateral transport of a variety of membrane components (proteins and lipids) is strongly affected by the presence of the dense cortical actin meshwork. The actomyosin cortex is simultaneously built of dynamic filaments and a dense actin meshwork. So far, we have not explicitly studied the effect of the mesh, except for taking its effect on momentum dissipation. This chapter explicitly takes the dense meshwork into ac-

count in terms of its interactions with membrane components. These observations provide the motivation for models such as "membrane-skeleton fence" model for transmembrane protein diffusion and the "anchored-protein picket" model for lipid diffusion [4, 5, 6]. In these models, the plasma membrane is partitioned into compartments of size $20 - 200\ nm$ by the actin-based membrane skeleton(MSK) and MSK-anchored proteins.

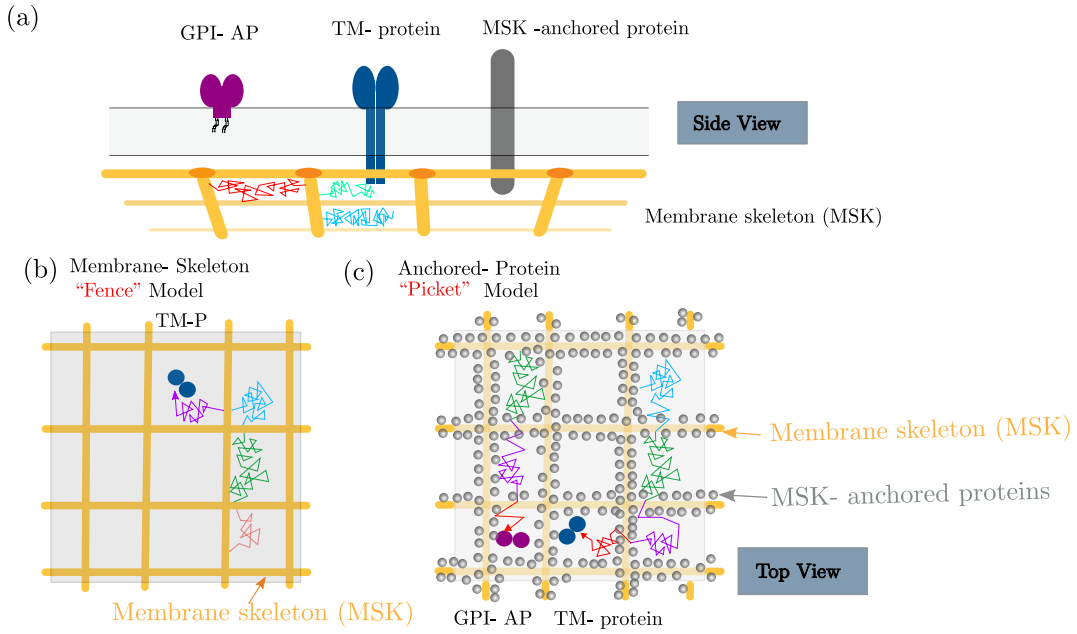

Figure 5.3 Membrane-skeleton "fences" and anchored-protein "pickets" models of the plasma membrane for lateral diffusion of transmembrane proteins and GPI-anchored proteins (GPI-AP). Short-time confined diffusion within a compartment and long time hop-diffusion between compartments are experienced by all membrane constituent molecules. (a) A schematic representation of transmembrane protein, GPI- anchored protein and an MSK-anchored protein from the side. The transmembrane protein interacts directly with the membrane skeleton and GPI-AP interacts via GPI-linkers. (b) The membrane-skeleton fence model shows that transmembrane proteins are confined in the mesh of the actin-based membrane skeleton. Meanwhile, lipids and GPI-anchored proteins in the membrane's outer leaflet have no clear interactions with the skeleton. (c) On the other hand, the anchored-protein picket model shows MSK-anchored proteins as immobile obstacles in the path of transmembrane proteins, lipids, and GPI-anchored proteins. [6]

In the membrane-skeleton fence model, the cytoplasmic domains of the transmembrane proteins interact with the membrane skeleton. This gives rise to the tempo-

rary confinement of the transmembrane proteins in the membrane-skeleton mesh compartments (Figure. 5.3 a and b). In the anchored-protein picket model, transmembrane proteins are anchored to and aligned along with the membrane skeleton. They effectively form rows of pickets. These pickets can create a barrier against the free diffusion of both lipids and transmembrane proteins (Figure. 5.3 a and c). Furthermore, the distribution of the membrane skeleton mesh size determined by Morone et al. [9] using electron tomography(Figure. 5.2) agrees well with the compartment sizes determined from the hop diffusion from a single-particle tracking experiment using a high-speed camera.

These observations from the single-particle tracking of molecules on the cell membrane reveal a cage-hopping behaviour due to cortical actin meshwork. A similar cage-hopping dynamics is observed in particle transport studies of a dense fluid approaching glass transition. This is the motivation to study the underlying physics of cage-hopping transport in the vicinity of a random field glass induced by the quenched random disposition of the cortical actin meshwork. Typically, a liquid upon slow cooling undergoes a first-order phase transition at the freezing point and forms a crystal. This crystallization can be avoided either by rapid cooling of the system or by introducing polydisperse disorder and the liquid enters a metastable liquid phase known as the supercooled liquid. With a further decrease in temperature, the viscosity and the relaxation time scale of this supercooled liquid continues to increase rapidly until it falls out-of-equilibrium (at $T = T_g$) [10]. The dynamics can be slowed down by 16 orders of magnitude but there is no signature of liquid to glass transition in static structural properties, such as radial distribution function ($g(r)$) or static structure factor ($S(q)$).

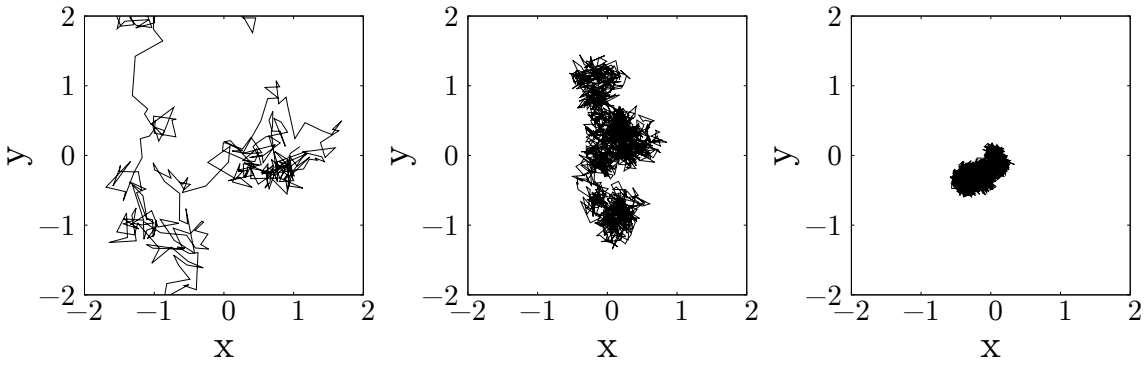

Figure 5.4 Trajectory of a single tagged particle in a model glass former (Kob-Andersen [11]) in 2-dimension at different temperature. (Left) The trajectory is diffusive at high temperature ($T = 5.0$). (Middle) The trajectory shows a strong signature of cage diffusion and hopping between cages at intermediate temperature ($T = 0.6$). (Right) The trajectory reveals that the particle is caged at a very low temperature ($T = 0.1$). Note, as the dynamics get slowed down by several orders of magnitude, the duration over which we plot the trajectories is progressively increased from left to right.

The dynamics of a tagged particle in a dense liquid at high temperature (i.e. far from the glass transition point) and at a long time limit can be described by Brownian motion. In Figure. 5.4 we have shown trajectory of tagged particle in Kob-Andersen glass [11], a popular simulation model for glass forming liquids. However, as the temperature of a liquid is decreased, a qualitatively new behaviour known as 'caging' occurs, in addition to the apparent slowing down of motion (see Figure. 5.4). It is evident from a particle's trajectory that the particle is confined for some time in a 'cage'-like structure created by its neighbours. It then escapes the cage (uncaging) and gets trapped inside another cage. This type of dynamic features, such as motion within a cage, cage hopping, and then again motion within another cage, results in a plateau in the mean squared displacement (MSD) and subsequent long time diffusion. Simultaneously, the two-point overlap correlation function ($Q(t)$), a measure of the dynamic slowing down, displays multi-step relaxation. When the system reaches the glassy phase at lower temperatures, this caging behaviour becomes stronger, and the corresponding plateau in MSD (see Figure. 5.5) becomes more prominent. The particle is confined in a cage at and below the glass transition, and the plateau extend to $t = \infty$. Consequently, this form of caging-uncaging

dynamics near the glassy phase and perpetual caging inside the glassy state is a measure of the liquid's dynamical arrest at the glass transition.

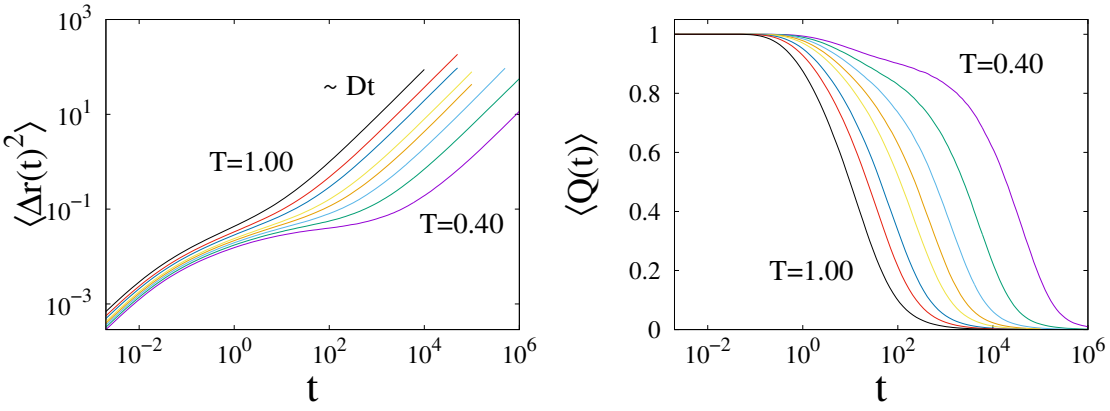

Figure 5.5 The mean squared displacement (MSD) at $T \gg T_0$ where T_0 is the glass transition temperature shows short time diffusive ($\sim t$) behaviour which crosses over to long time diffusive behaviour ($\sim t$) via sub-diffusion. Because of caging, as T decreases, the MSD starts to display a slight plateau at intermediate times. The width of the plateau increases as T decreases more, and at T_0 (not shown), MSD stays in the plateau region over the simulation time scales and does not exhibit late time diffusive behaviour, suggesting that the system has entered a glassy state.

One of the outstanding issues in the study of the glassy system is understanding the rapid growth in viscosity (η) or structural relaxation time (τ_α) of supercooled liquids while approaching the glass transition [10, 12, 13, 14]. Experimentally, the temperature at which the supercooled liquid's viscosity reaches the value 10^{12} Pa.s is defined as the glass transition (dynamic) temperature. The transition point can be extracted from both the diffusion constant (D) and the relaxation timescale (τ_α), extrapolating the supercooled liquid side data. An important question in the field is whether an "ideal" thermodynamic glass transition, characterised by the vanishing of configurational entropy, can occur at a temperature less than the experimentally defined operational glass transition temperature [15, 18, 16, 17]. The difficulty in observing this ideal glass transition is that the supercooled liquid goes out of equilibrium. Recently, it has been proposed that liquids in the presence of quenched disordered can bypass this difficulty [19]. These studies suggest a higher thermodynamic glass transition temperature in quenched disordered liquids when compared to

the transition temperature of the liquid without the disorder and that the transition temperature will increase with pinning density in the quenched disorder system.

However, a recent molecular dynamics simulation study finds no sign of increased transition temperature with increasing pinning concentration [20].

We now return to the problem of single particle transport in the plasma membrane of the cell. The cortical meshwork adjoining the plasma membrane provides a quenched random environment with correlated line disorder. The meshwork pins those cell membrane molecules that directly bind to it, giving rise to the suggested picket-fence model. These pinned MSK-anchored proteins, in turn, provides obstacles to other molecules, even small molecules such as upper leaflet lipids, with no direct interaction with the cortical meshwork. This novel random pinning model on molecular transport is quite distinct from the random pinning potentials studied in the glass literature. Here, the effects of topological confinement become significant. We study the transport and approach to a new kind of glass using a agent-based Brownian dynamics simulations. Using such descriptions, we are able to make several predictions that can be tested in future experiments.

5.2 Simulation details

We have studied a binary mixture of particles (α and β) in two dimensions ($2d$). A pair of particles of the same species interact via the following potential,

$$\begin{aligned} V_{ij}(r) &= 4\epsilon_{ij}\left[\left(\frac{a_{ij}}{r}\right)^{12} - \left(\frac{a_{ij}}{r}\right)^{6}\right] + v(r) \text{ for } r \leq 3a_{ij} \\ &= 0 \text{ for } r > 3a_{ij} \end{aligned} \tag{5.1}$$

where, r is the distance between the i-th and the j-th particle, $a_{ij} = (\sigma_i + \sigma_j)/2$ and σ_i is the diameter of the particle i. We have truncated and shifted the potential at the cutoff using quadratic function $v(r) = V_0 + V_2\, r^2$.

Particles of different species interact through the Weeks-ChandlerAndersen (WCA)

potential:

$$\begin{aligned} V_{ij}(r) &= 4\epsilon_{ij}\left[\left(\frac{a_{ij}}{r}\right)^{12} - \left(\frac{a_{ij}}{r}\right)^{6}\right] + v(r) \text{ for } r \leq 2^{1/6}a_{ij} \\ &= 0 \text{ for } r > 2^{1/6}a_{ij} \end{aligned} \tag{5.2}$$

Thus, in this model [21], particles have attractive interactions with other particles of the same species and repulsive interactions with those of different species. We introduce polydispersity in the particle size on top of the bi-dispersity in interaction energy to avoid crystallization. We choose particles diameter from uniform distribution between 0.8σ and 1.2σ for each component. The polydispersity index for this distribution of size is $\delta = 11.5$. The number of A and B particle is N_A and N_B respectively. The fraction of A particle is denoted as $x = N_A/N$. The total number of the particle is $N = 1500$. We mainly consider the "binary model" ($x = 0.5$) to study phase segregation and the "pure model" ($x = 1$) to study the glass behaviour of the system. We have done Brownian Dynamics simulation, for particle coordinate updates, using verlet integration scheme with integration time step $\Delta t \sim 2 \times 10^{-3}$. The dynamics of the position of the i-th particle is given by

$$\dot{\mathbf{r}}_i = -\gamma^{-1}\boldsymbol{\nabla}_i V_i + \sqrt{2k_BT/\gamma}\boldsymbol{\xi}_i \tag{5.3}$$

where γ is the friction coefficient of the particle, V_i is the net potential felt by the i-th particle and includes contributions from Eq. 5.2. The diffusion of the particle is driven by a thermal noise $\boldsymbol{\xi}_i$ with zero mean and unit variance acting on i-th particle (k_B is the Boltzmann constant).

All results presented here are for number density $\rho = 0.925$ in a two-dimensional (2d) area of linear dimension $L = 40.26$ with periodic boundary conditions (PBC). The system is well equilibrated at a high temperature ($T = 4$) in its liquid state and then quenched to a low temperature to prepare the initial configurations. Then the system is equilibrated at that temperature with a runtime one-tenth of the production run time to reach the steady-state of that temperature. Then, we perform the production runs at each target temperature. All data presented here have been averaged over 16 independent realisations. All the results are reported in Lennard-Jones

units: length in σ, energy in ϵ, temperature in ϵ/k_B, and time in $\sqrt{m\sigma^2/\epsilon}$.

Our choice of Brownian dynamics simulations is justified science the dominant source of momentum dissipation is via friction associated with moving relative to the crosslinked cortical meshwork.

Pinning Protocol

In our simulation, we have incorporated the effects of static actin mesh via an short range attractive line pinning potential. In doing so we ignore microscopic structural details of the actin mesh and the linking proteins. The effect of the cortical actin mesh has been modelled by introducing interaction between particles and a criss-cross array of attractive line potential in our system. The interaction of pinned particles with the lines is modelled by attractive Gaussian potential $-V_0 \exp(-r^2/\lambda)$ characterised by pinning strength V_0 and length scale λ. The whole system is divided into very fine grids, where we calculate the potential value at the grid points due to the attractive lines. This decaying potential with a small length scale (λ) ensures that the pinned particles will feel strong attractive potential only at grid points near the line-potential. This attractive interaction with the line-potential force pinned particles to arrange themselves in line. The lines built by the pinned particles are in the same plane as the membrane, and the stiffness of the attractive line potential is large enough to suppress thermal fluctuations. The lines are distributed along the x or y axis with randomness in their position parametrised by Δ to form random orthogonal rectangular grids. The probability distribution of the area of the resulting random mesh is parametrised by this randomness parameter Δ. This mesh is characterised by Δ, V_0 and number of lines n_l in a fixed system size.

Now we will discuss the results of the system. We have explored both the *physics of random field glass* and *phase segregation* in this system.

5.3 Glass Physics

We have discussed in section 5.1 that although the structural properties do not change much as the system approaches the glassy phase, the dynamic properties of the system show drastic variation. Here, we will look into different dynamic quan-

tities to understand the effect of line pinning in this dense system.

5.3.1 Caging dynamics

Simple glass without pinning shows qualitative changes in the particle trajectories as one approaches the glass transition. The trajectory of a tagged particle at high temperature ($T = 1.0$) is diffusive in the unpinned system and shows the signature of cage diffusion and hopping between cages at intermediate temperature ($T = 0.6$). However, the trajectory shows a very strong signature of caging dynamics at high temperature in the pinned system. Initially, particle trajectory shows hopping between cages formed by the neighbour particles, and at large time particle hops between the cages formed by the pinned particles. This strong caging dynamics signature is observed in the two-point correlation functions (such as MSD and $Q(t)$) with time, as discussed below.

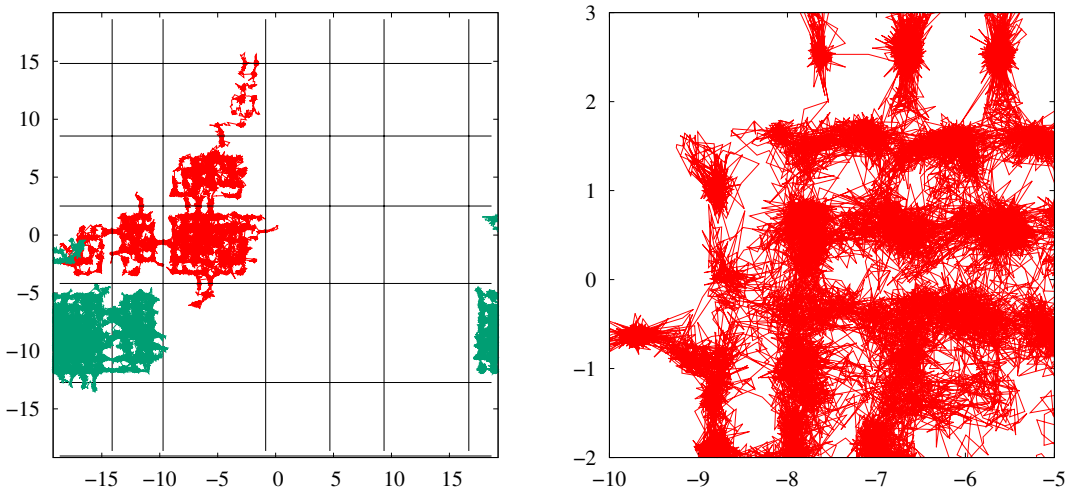

Figure 5.6 Trajectory of tagged particle at temperature $T = 1$ for pinning potential $V_0 = 8$ and number of lines $n_l = 6$. (a) Two sample trajectories has been shown in two different colour (red and green). Black lines are the pinning lines. (b) Zoomed in trajectory over a small area (5×5) clearly shows the cage-hopping of the particle inside the cage formed by the pinned particles.

5.3.2 Mean Square Displacement (MSD)

To study the system dynamics more quantitatively, we measure the mean-square-displacement (MSD) of tagged particles, $\langle \Delta r^2 \rangle$, as a function of time t. The time-dependent diffusion constant $D(t) = \frac{\langle \Delta r(t)^2 \rangle}{4t}$ shows diffusive behaviour at small time. The two sub-diffusion to diffusive crossover in the time-dependent diffusion constant (Figure. 5.7) is a signature of the two types of cage hopping dynamics we see in the trajectory Figure. 5.6. The first crossover is associated with the 'cage'-like structure created by its neighbours, and the second crossover associated with the cages formed by the pinned particles. As we lower the temperature, we are unable to capture the second crossover within our run time. The sub-diffusion follows the same $t^{-0.5}$ scaling for pinned system with different number of lines ($n_l = 4, 6$).

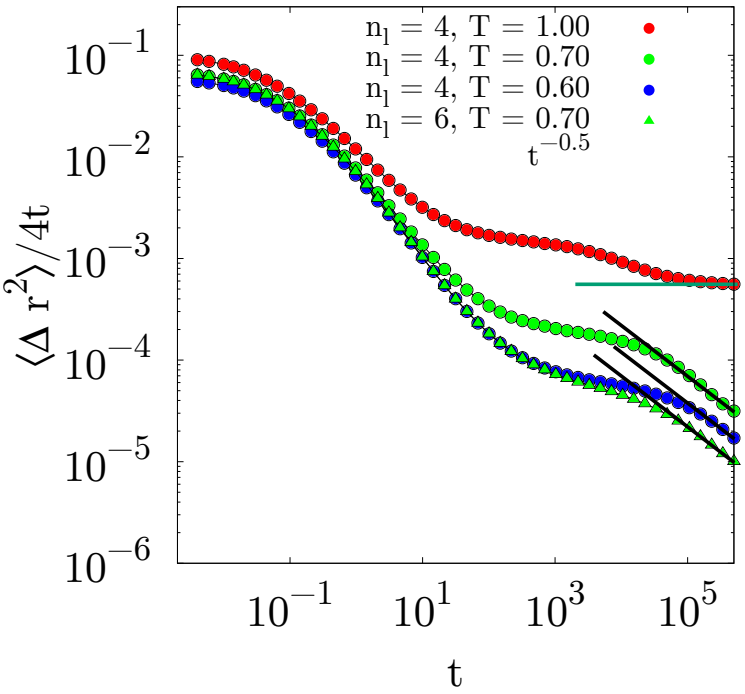

Figure 5.7 Mean squared displacement (MSD) divided by $4t$ has been plotted as a function of time (t) at three different temperature for line pinning potential $V_0 = 8$ and density $n_l = 4, 6$. In pinned system at $T = 1.0$ (red circle), we see two sub-diffusive to diffusive crossover before it saturates in the late time diffusive regime, where as in unpinned system we see only one sub-diffusive to diffusive crossover. As we lower the temperature, we are unable to capture the second crossover within our run time and the sub-diffusion follows $t^{-0.5}$ scaling.

We have studied the variation in MSD with temperature in the pinned system with line pinning potential $V_0 = 8$ and number of lines $n_l = 6$. Figure. 5.8 shows that at high temperature, the time-dependent diffusion constant saturates at a long time diffusion value (marked by the black line) with a single crossover. As we decrease the temperature, two sub-diffusive to diffusive crossover appears in the MSD. Finally, the system does not reach the long time saturation within our run time at low temperature.

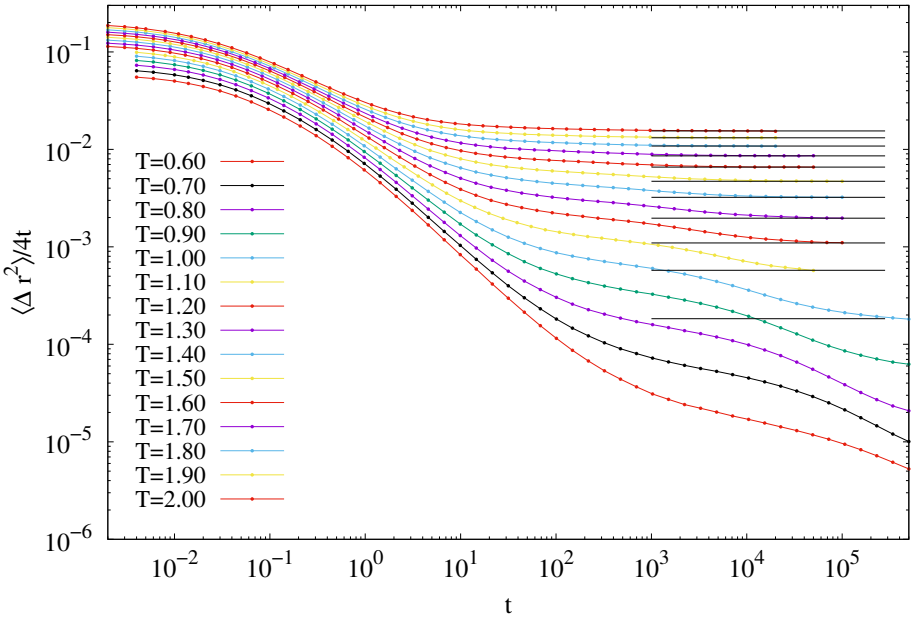

Figure 5.8 Mean squared displacement divided by $4t$ has been plotted as a function of time (t) at different temperature for line pinning potential $V_0 = 8$ and $n_l = 6$. The time-dependent diffusion constant ($D(t)$) shows one sub-diffusive to diffusive crossover at high temperature before it saturates in the late time diffusive regime. We find two sub-diffusive to diffusive crossover at intermediate temperature before it saturates in the late time diffusive regime. At low temperate, the system does not reach the late time saturation regime within our run time.

5.3.3 Two-point overlap correlation function (Q(t))

The two-point overlap correlation function ($Q(t)$) has been measured to study the system's dynamics. The decay of $Q(t)$ with time provides a measure of the dynamic slowing down in glass systems [16].

$$Q(t) = \frac{1}{N - N_p} \sum_i \langle w(|\mathbf{r}_i(t_0) - \mathbf{r}_i(t + t_0)|) \rangle \tag{5.4}$$

where,

$$w(r) = \begin{cases} 1 & \text{if r} \leq a_0 \\ 0 & \text{otherwise} \end{cases} \tag{5.5}$$

and $\langle ... \rangle$ indicates an average over the time origin t_0 and as well as different statistically independent simulation runs. The summation is over all unpinned particles $N - N_p$ and parameter a_0 is a short-distance cutoff chosen to be $a_0 = 0.3$ in Lennard-Jones unit.

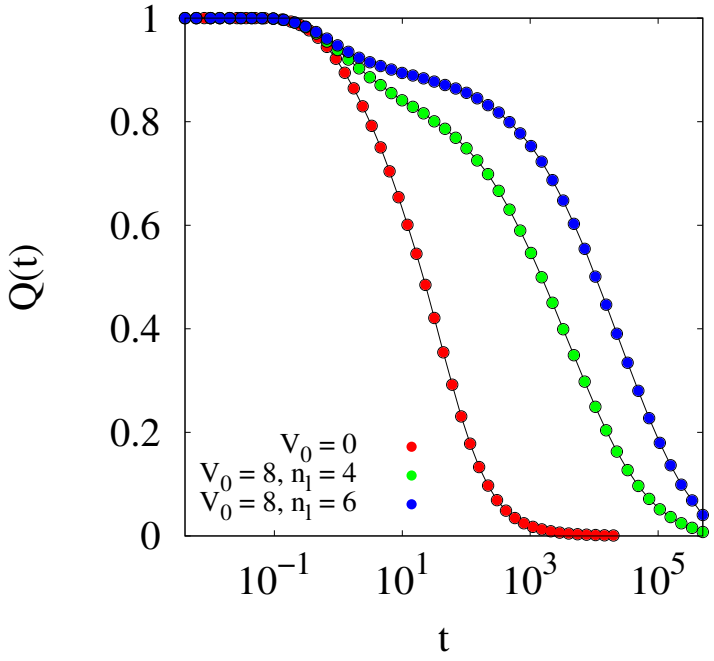

Figure 5.9 The decay of two-point self-correlation function $Q(t)$ has been shown for unpinned system ($V_0 = 0$) and two pinned system with $V_0 = 8$ and $n_l = 4, 6$ at $T = 0.7$. In unpinned system at $T = 0.7$ (red circle) the $Q(t)$ decays exponentially to zero, characteristic of a liquid. In pinned system $Q(t)$ starts exhibiting multi-step relaxation with stretched exponential behaviour, the signature of caging what we see at low temperature in unpinned system. It is worth noting that stretching in $Q(t)$ increases as we increase the number of lines from 4 to 6.

Figure. 5.9 shows the two-point self-correlation function $Q(t)$ decays exponentially in the unpinned system at $T = 0.7$ (high temperature). In the pinned system at the same temperature $T = 0.7$, the two-point self-correlation function $Q(t)$ decays slowly, and with increasing number of lines n_l, it decays more slowly. It shows multi-step relaxation in the pinned system, the signature of caging that we see at low temperature in the unpinned system. This multi-step relaxation can be described by stretched exponential function at long time.

5.3.4 Glass Transition

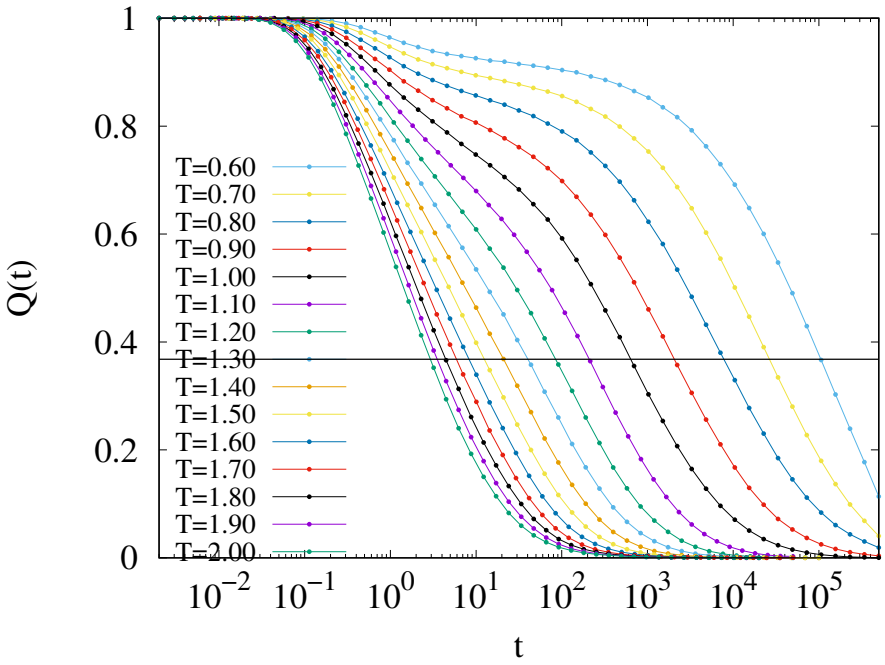

Figure 5.10 The decay of two-point self-correlation function $Q(t)$ has been shown at different temperature for the line pinning potential $V_0 = 8$ and number of lines $n_l = 6$. At high temperature $Q(t)$ decays exponentially to zero, characteristic of a liquid. Upon decreasing temperature $Q(t)$ starts exhibiting multi-step relaxation, the signature of caging.

In order to find out the glass transition temperature, the decay of the two-point self-correlation function $Q(t)$ has been studied for a set of temperature. We have done

this study for unpinned system ($V_0 = 0$) and pinned system with number of lines $n_l = 4, 6$. In Figure. 5.10, we have shown the decay of $Q(t)$ with time at different temperature for pinning potential $V_0 = 8$ and $n_l = 6$.

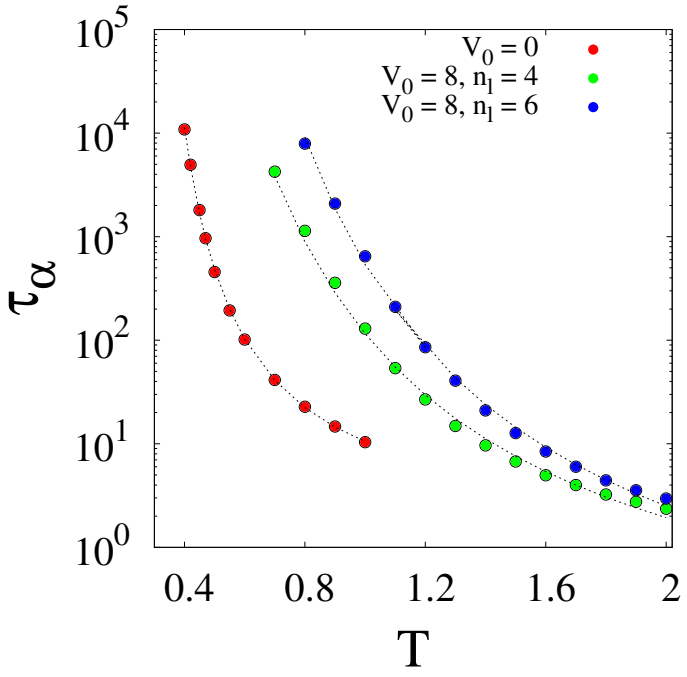

Figure 5.11 Relaxation timescale (τ_α) extracted from $Q(t)$ has been plotted with temperature (T) for unpinned system ($V_0 = 0$) and two pinned system with $V_0 = 8$ and $n_l = 4, 6$. The rapid rise in the relaxation time with decreasing T has been fitted with VFT exponential form. The black dotted line is fit to the data.

At high enough temperature, $T = 2.0$, $Q(t)$ decays exponentially to zero, characteristic of a liquid. On decreasing the temperature, $Q(t)$ starts exhibiting multi-step relaxation, described by a stretched exponential function at long times, a hallmark of supercooled liquid. The α-relaxation time scale τ_α has been extracted from the $Q(t)$ using the definition $Q(\tau_\alpha) = 1/e$. This α-relaxation time scale (τ_α) has been plotted against temperature (T)(Figure. 5.11). The relaxation time (τ_α) rises rapidly and exponential in nature as T is decreased close to the glass transition point. The black dotted line is a fit to the Vogel-Fulcher-Tammann exponential form

$$\tau_\alpha = \tau_\infty \exp\left[\frac{1}{\kappa(\frac{T}{T_0} - 1)}\right] \tag{5.6}$$

where τ_∞ is the relaxation time at very high temperature, T_0 is the glass transition temperature, κ is the kinetic fragility. Fragility is a quantitative measure of the speed in the increase of a supercooled liquid's relaxation timescale or viscosity when the glassy phase is approached. Depending on the rapidity of increase in the viscosity or the relaxation timescales glassy materials can be divided into two class: (a) fragile glass (b) strong glass. Kinetic fragility (κ) value is large in fragile glass than strong glass. Figure. 5.11 shows the increase of relaxation timescale τ_α as we decrease T. In the case of line pinning, we see a decrease in glass transition temperature T_0 and kinetic fragility (Figure. 5.12).

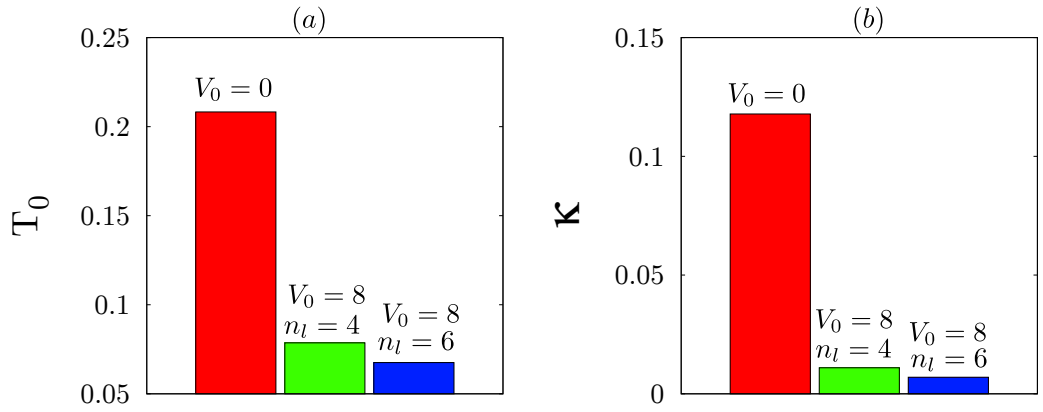

Figure 5.12 We have extracted the glass transition temperature (T_0) and kinetic fragility (κ) from the extrapolated behaviour of relaxation time scale (τ_α) by fitting data with VFT exponential form. (a) Glass transition temperature for the unpinned system is $T_0 = 0.208$ (red bar). In the pinned system the glass transition temperature decays to $T_0 = 0.078$ for $n_l = 4$. As we increase the number of line to $n_l = 6$ the transition temperature decays to $T_0 = 0.067$. (b) Kinetic fragility (κ) decays in a order of magnitude in pinned system from unpinned system. With higher number of lines the fragility value is small.

5.3.5 Dynamical heterogeneity

The dynamics of a tagged particle in liquid is mostly homogeneous in terms of tagged particle mobility. Now, as one decrease the temperature, particles form slow-moving and fast-moving correlated regions. This dynamical heterogeneity in the displacement field becomes prominent as one approaches the glassy phase. The dynamic susceptibility $\chi_4 = \frac{1}{(N-N_p)}\left[\langle Q(t)^2\rangle - \langle Q(t)\rangle^2\right]$, a 4-point correlation function is obtained from the fluctuation of $Q(t)$ [16].

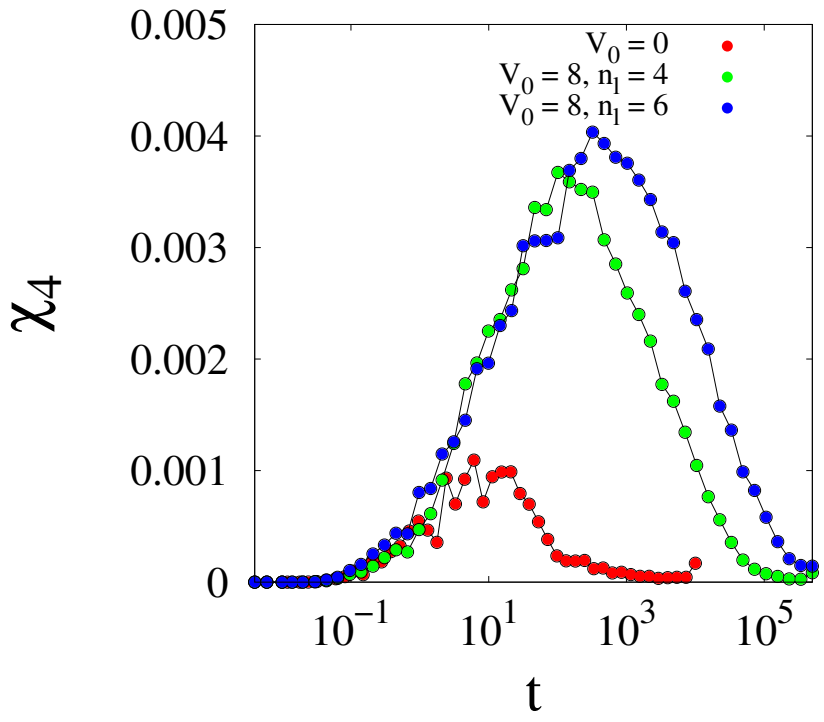

Figure 5.13 Dynamic susceptibility $\chi_4(t)$ has been plotted as a function of time for for unpinned system ($V_0 = 0$) and two pinned system with $V_0 = 8$ and $n_l = 4, 6$ at $T = 1.0$. We see a increase in peak position and peak height (χ_4^*) in pinned system compare to the unpinned system. The huge increase in peak height infers increase in dynamical heterogeneity in pinned system than the unpinned system at same temperature.

This four-point susceptibility function exhibits a maximum. The peak position $t = \tau_4$ is proportional to the structural relaxation time τ_α obtained from the temporal decay of $Q(t)$ and the peak height (χ_4^*) of this function is a measure of the dynamical heterogeneity in the system. We see a considerable increase in dynamical heterogeneity in the pinned system compared to the unpinned system (see Figure. 5.13). Peak height also increases with number of lines.

In order to see this dynamical heterogeneity, we colour plot the magnitude displacement within the α-relaxation time scale (τ_α) of all particles (all unpinned particles in the case of the pinned system) with their displacement vector in Figure. 5.14. Both unpinned and pinned system shows emergent collective large length scale correlated motion. However, in the pinned system, we notice that the displacement

of particles close to the line is smaller than the bulk particles displacement due to entropic reason. The motion of the unpinned particles near the line is constrained, which makes them slow. This slow unpinned particles in turn makes the next layer of particles slow. There is a length scale associated with this [31]. Statistically, we see less displacement of particles in smaller cages than big one.

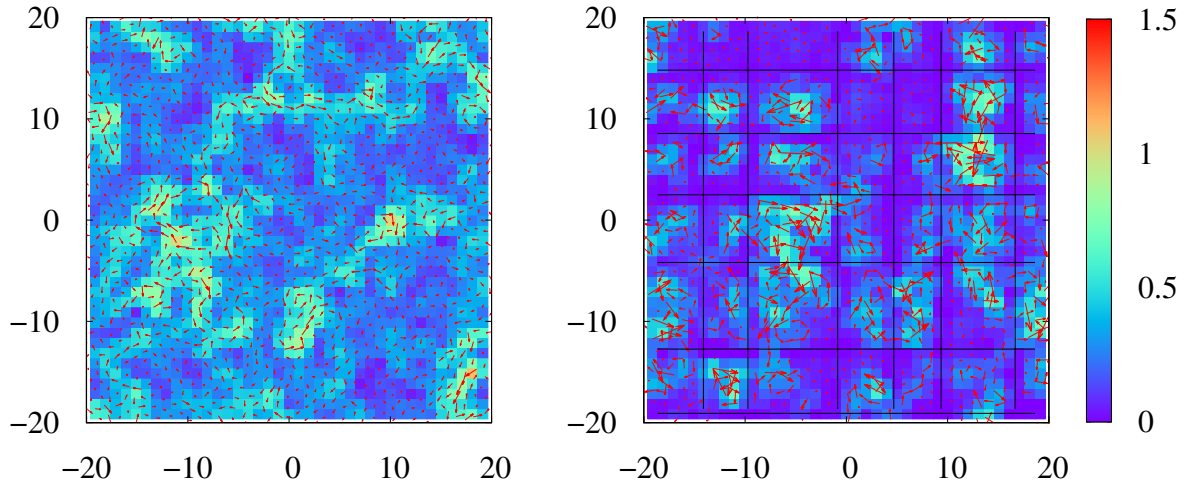

Figure 5.14 Displacement distribution of all unpinned the particles within the α-relaxation time scale (τ_α) has been plotted at $T = 1.0$ for (a) unpinned system and (b) pinned system with line pinning potential $V_0 = 8$ and density $n_l = 6$. Both displacement map shows collective large-scale correlated motion in region. Another feature in case of line pinned system is that the displacement of particles close to the line is smaller than the bulk particles.

This feature has been captured by the bi-modality in the displacement distribution of the particles (see Figure. 5.15) in the pinned system. The peak at small displacement in the distribution comes from the set of particles near the line and peak at large displacement comes from the bulk particles in the cage. In contrast, the unpinned system shows uni-modal behaviour.

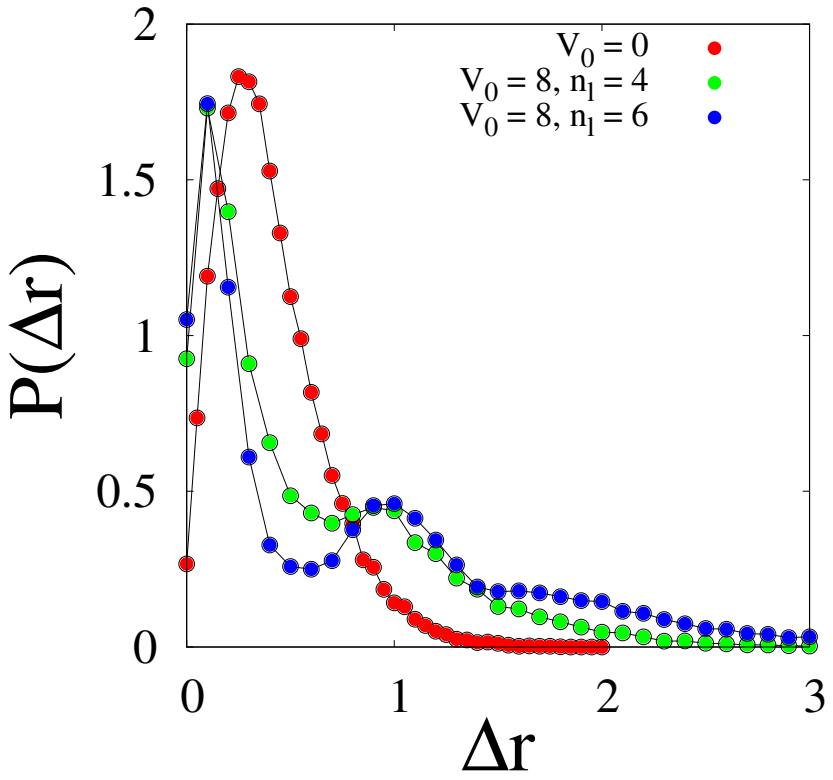

Figure 5.15 Distribution of root of mean square displacement (Δr) within the α-relaxation time scale (τ_α) for unpinned system ($V_0 = 0$) and two pinned system with $V_0 = 8$ and $n_l = 4, 6$ shows qualitatively different behaviour. The unpinned system shows uni-modal behaviour. On the other hand pinned system shows bi-modality; the peak at small displacement comes from the set of particles near the line and peak at large displacement comes from the bulk particles in the cage.

We have studied how the displacement of particles depends on the cage size. Figure. 5.16(a) shows mean square displacement of unpinned particles in a cage within a time window $t_w = 10^3$ increases with cage size. Probability distribution of mean square displacement ($(P(\langle \Delta r^2 \rangle))$) of particles in a cage becomes wide with cage size Figure. 5.16(b).

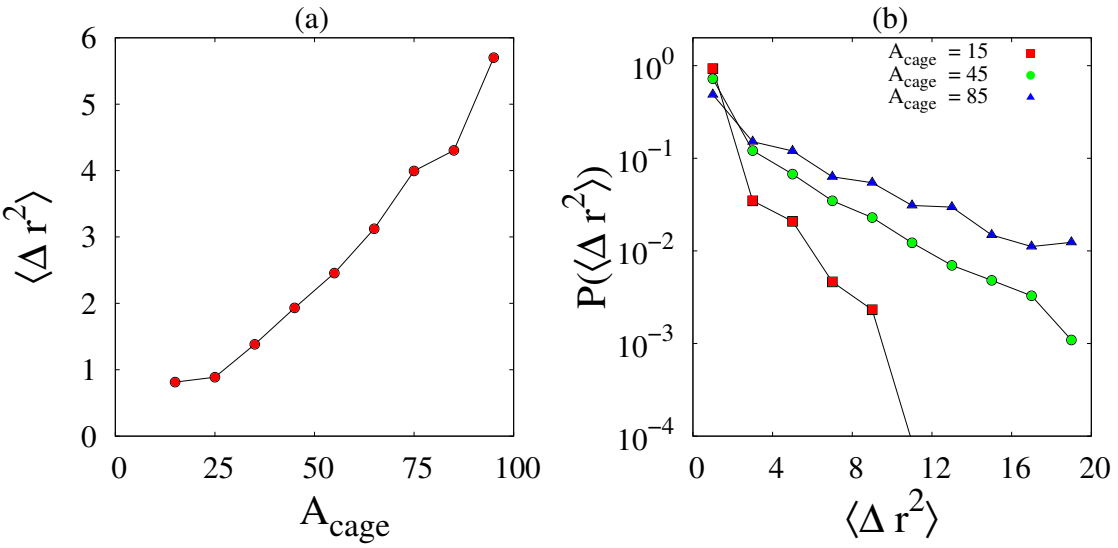

Figure 5.16 (a) Mean square displacement ($\langle \Delta r^2 \rangle$) of all unpinned the particles in a cage within a time window $t_w = 10^3$ has been plotted with cage area (A_{cage}) in a pinned system with line pinning potential $V = 8$ and $n_l = 6$ at $T = 1.0$. (b) Probability distribution of mean square displacement ($(P(\langle \Delta r^2 \rangle))$) of particles in a cage has been shown for three different cage area $A_{cage} = 15$ (red square), $A_{cage} = 45$ (green circle) and $A_{cage} = 85$ (blue triangle).

5.4 Phase Separation in the cell membrane

In the cell membrane, it has been frequently found that various species of molecules tend to stay segregated. These lateral heterogeneous organizations are essential for physiological functions. The size of these domains ranges from a few nanometers to few microns. For example, lipid-rafts that are a segregated region of highly ordered lipids effectively concentrate specific proteins in this domain and helps in molecular associating events, such as signalling. Recently, much attention has been given to the mechanism of formation and stabilization of these domains. The appearance of these domains in a multi-component lipid vesicle is considered a form of two-dimensional equilibrium phase separation that develops due to the interaction between lipid molecules. In this equilibrium phase separation, when a multi-component system is quenched from a homogeneous state into an unstable state below its phase separation temperature (T_c), domains form in the system and evolve with time until segregate. These domains coarsen and grow according to a power-law $l(t) \sim t^{\alpha}$, where $l(t)$ is the

characteristic size of the domains. Various experiments [27, 28], simulations [25, 26] and theoretical study [29, 30] has established the domain growth scaling in case of both diffusive and hydrodynamic coarsening. In the case of diffusive coarsening, the characteristic size of the domain grows as $\xi \sim t^{1/3}$ [24]. Here, we study the phase separation of binary mixtures as a model of phase segregation of membrane molecules. However, the cell must control this phase separation process to build functional segregation of molecules at the correct time and desired location. Recent studies have revealed that the interaction of membrane molecules with the dense actin meshwork and actomyosin activity influences the segregation of membrane molecules. This motivates us to study the effect of line pinning and activity on phase separation in a dense binary mixture (A and B) with agent-based Brownian dynamics simulation. In a binary mixture, the local fraction of the components $\phi = \frac{n_A - n_B}{n_A + n_B}$, where n_A and n_B are local number density of A and B, is the conserved order parameter to distinguish between homogeneous phase and segregated phase. Phase segregation of the passive unpinned system with a similar choice of the parameter has been studied by Ikeda et al. [21]. The phase separation temperature $T_c = 1.93$ is obtained by monitoring the probability distribution of the order parameter.

5.4.1 Phase separation in Line-Pinned system

We have studied the effect of line pinning on the phase separation in a dense binary mixture, described in section 5.2. This line pinning is a realisation of quenched disorder of membrane proteins formed by the dense actin meshwork, as discussed in section 5.1 and 5.2. The probability distribution of order parameter ($P(\phi)$) shows a peak at zero in the single-phase homogeneous state. On the other hand, in the segregated two-phase state, the PDF becomes bimodal, showing peaks at ± 1. The probability distribution of order parameter ($P(\phi)$) shows bi-modality when temperature is quenched below T_c ($T = 1.0$) without line-pinning ($V = 0$)(red circle in Figure. 5.17). As, the system get phase segregated below T_c, the probability distribution of order parameter shows peaks at ± 1. Note that the phase separation temperature of the binary mixture is $T_c = 1.93$. The probability distribution of order parameter ($P(\phi)$) shows peak at zero when temperature is quenched below T_c ($T = 1.0$) in the presence of line-pinning ($V = 12$)(blue square in Figure. 5.17.

Actin meshwork prevents the segregation from happening when the temperature is quenched below T_c.

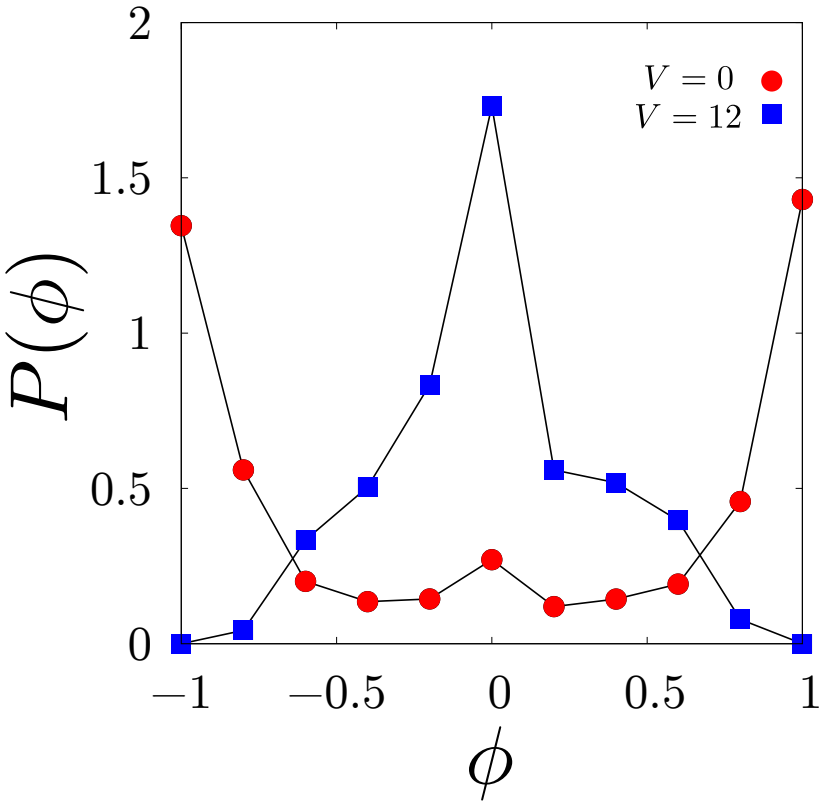

Figure 5.17 The probability distribution of order parameter ($P(\phi)$) is shown when the system is quenched into $T = 1.0$ without line-pinning ($V_0 = 0$, red circle) and in the presence of line pinning ($V_0 = 12$, blue square).

5.4.2 Phase separation in Active Glass

Membrane molecules that bind to cortical actin, are driven by contractile flows generated by active actomyosin stresses. We have modelled this active force on the molecule by a self propulsion force $f_0\hat{\mathbf{n}}$ along $\hat{\mathbf{n}}$ with a active orientational decorrelation time τ_a. We have studied the phase separation in this dense binary mixture in the presence of activity. The magnitude of order parameter plotted in the $T - f_0$ plane with colour shows three different regions (Figure. 5.18). At low f_0 and T, the system is dynamics arrested, and the order parameter value is small in this homogeneous glassy phase. As we increase T or f_0, the order parameter value increase, and the mixture gets phase segregated. At high temperature $T > T_c$

naturally the system goes into homogeneous phase (not shown in the Figure. 5.18). The increase of active force increases the effective temperature, which leads the system into a homogeneous liquid state.

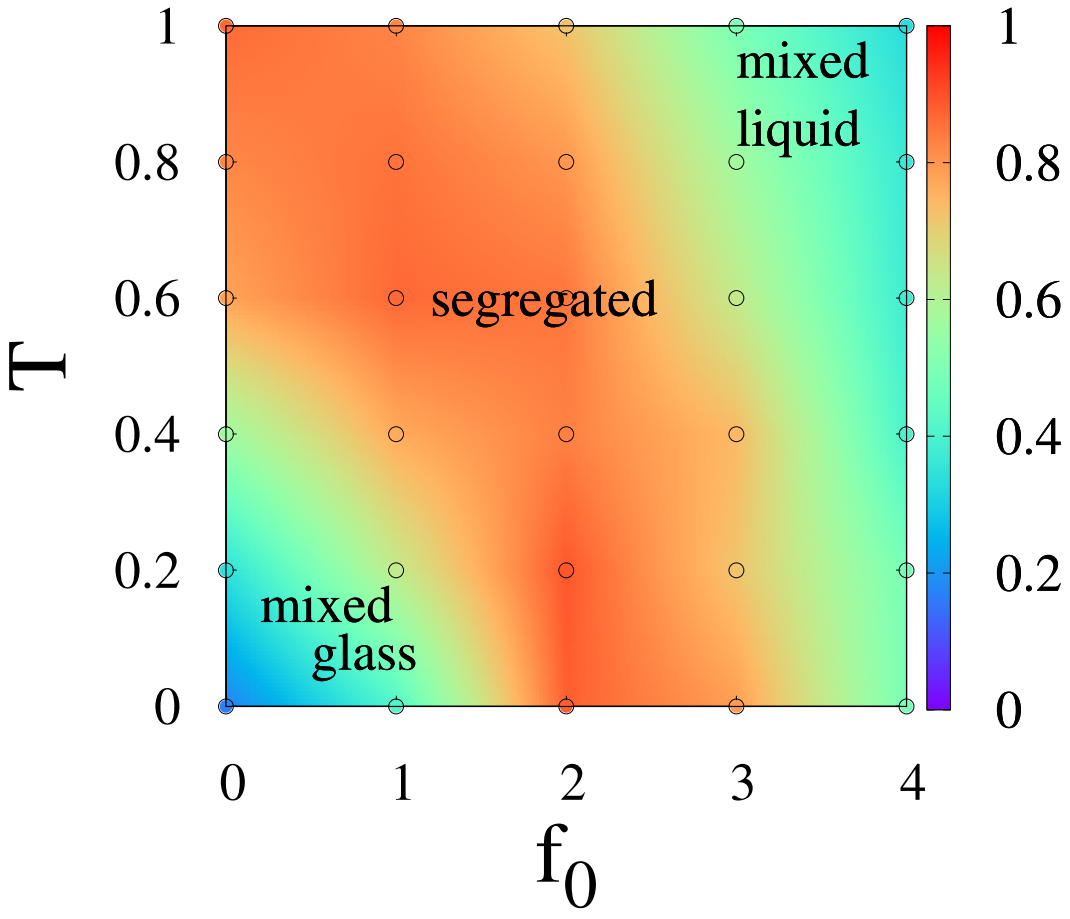

Figure 5.18 The phase diagram in the $T - f_0$ plane. The circles indicate the points at which simulations are performed. The magnitude of the order parameter is plotted in the $T - f_0$ plane with colour. The small value of the order parameter indicates a homogeneous phase. At a small T and f_0 value, the system is in the glassy phase. Due to very slow dynamics in this region, the phase separation process does not happen even the system is in $T < T_c$ in simulation run time. On the other extreme, when f_0 is high, or T is high, or both values are high, the system is also homogeneous. We see phase segregation in the middle region.

5.5 Discussion

The similarity between cage hopping behaviour of membrane molecule and particle dynamics in dense super-cooled liquid has motivated us to study the underlying physics of cage-hopping transport of membrane molecules. Here we show that the actin mesh adjoining the cell membrane acts as a random line pinning that drives it towards a dynamically arrested state at physiological temperatures. This perspective introduces the membrane-actin mesh composite as a novel example of a random pinning glass. It introduces the language of glassy physics to study the dynamical properties of the cell membrane.

Here we summarise the results presented in this chapter and discuss the possible scope for future developments. We have carried out a detailed numerical study of the dynamics of glass-forming liquid with a fraction of particles pinned on random lines. The trajectory of unpinned particles shows a strong indication of caging dynamics. This signature of caging dynamics is observed in two-point correlation functions. Mean square displacement shows two sub-diffusive to diffusive crossover even at high temperature. The two-point overlap function $Q(t)$ shows stretched exponential behaviour, and the structural relaxation time (τ_α) extracted from it has increased by few decades at high temperature. The temperature dependence of structural relaxation time (τ_α) is fitted to VFT exponential form, and glass transition temperature (T_0) is inferred. We see glass transition temperature decreases in the pinned system and a huge decrease in kinetic fragility (κ), making the pinned glass less fragile. As we increase the number of lines, both of these quantity decreases. We see a considerable increase χ_4 peak height signature of increasing dynamical heterogeneity in the pinned system. In pinned system, the displacement of the unpinned particles close to the lines is much smaller than the bulk particles. This is the reason behind the huge increase in dynamical heterogeneity and bi-modal displacement distribution in the pinned system.

In future, we would like to extend this work for more different line pinning densities line densities (n_L) and cage size distribution. To account for the fact that the actin mesh coupling to the membrane is dynamic and occurs at different spatial locations, we may allow pinning potential $V(x,t)$ to stochastically flash between 0 and V with a specific rate that depends on space. In future, we would like to study the effect

of this stochastic flashing on membrane component dynamics and organisation. We hope this perspective will provide insight into the study of localisation dynamics in the presence of line randomness.

Interaction with the actin meshwork and actomyosin activity can influence the phase segregation of membrane molecules. We have studied the influence of random line pinning and activity on the phase segregation of binary glassy mixture. Actin meshwork prevents segregation from happening when the temperature is quenched below T_c. This gives the cell control over the segregation process. In future, we would like to study the influence of actin meshwork and activity combinedly on the phase segregation process, the fluctuation of the interface and kinetics of domain growth.

References

[1] S. J. Singer, Garth L. Nicolson, Science, **175**, (1972).

[2] Vrljic, M., S. Y. Nishimura, S. Brasselet, W. E. Moerner, and H. M. McConnell, Biophys. J. **83** 2681 (2002).

[3] Vrljic, M., S. Y. Nishimura, W. E. Moerner, and H. M. McConnell, Biophys. J. **88**, 334 (2005).

[4] T. Fujiwara, K. Ritchie, H. Murakoshi, K. Jacobson and A. Kusumi, J. Cell Biol. **157**, 904 (2002).

[5] Murase, K., T. Fujiwara, Y. Umemura, K. Suzuki, R. Iino, H. Yamashita, M. Saito, H. Murakoshi, K. Ritchie and A. Kusumi, Biophys. J. **86** 4075 (2004).

[6] Y. M. Umemura, M Vrljic, S. Y. Nishimura, T. K. Fujiwara, K. G. N. Suzuki and Akihiro Kusumi, Biophysical Journal **95**, 435 (2008).

[7] A. Kusumi, T. K. Fujiwara, R. Chadda, M. Xie, T. A. Tsunoyama, Z. Kalay, R. S. Kasai, K. G. N. Suzuki, Annu. Rev. Cell Dev. Biol. **28** 215-50 (2012).

[8] Kusumi A, Tsunoyama T A, Hirosawa K M, Kasai R S and Fujiwara T K, Nature Chemical Biology **10**, 524–32 (2014).

[9] N. Morone, T. Fujiwara, K. Murase, R. S. Kasai, H. Ike, S. Yuasa, J. Usukura, and A. Kusumi, The Journal of cell biology **174**, 851 (2006).

[10] A. Cavagna, Phys. Rep. **476**, 51-124 (2009).

[11] W. Kob and H. C. Andersen, Phys. Rev. Lett. **73**, 1376 (1994).

[12] L. Berthier and G. Biroli, Rev. Mod. Phys. **83**, 587 (2011).

[13] T. R. Kirkpatrick, D. Thirumalai, and P. G. Wolynes, Phys. Rev. A, **40**, 1045 (1989).

[14] V. Lubchenko and P. G. Wolynes. Annu. Rev. Phys. Chem., **58**, 235, (2007).

[15] G. Biroli, and J. P. Bouchaud, The random first-order transition theory of glasses: a critical assessment. Structural Glasses and Supercooled Liquids: Theory, Experiment, and Applications 31–113 (2012).

[16] S. Karmakar, C. Dasgupta and S. Sastry, Proc. Nat. Acad. Sci. USA **106**, 3675 (2009).

[17] S. Karmakar, C. Dasgupta and S. Sastry, Annu. Rev. Condens. Matter Phys. **5**, 255-284 (2014).

[18] L. Berthier, G. Biroli, J.-P. Bouchaud, L. Cipelletti, D. El Masri, D. L'Hote, F. Ladieu, M. Pierno, Science **310**, 1797–1800 (2005).

[19] C. Cammarota, and G. Biroli, Proceedings of the National Academy of Sciences **109**, 8850–8855 (2012).

[20] S. Chakrabarty, S. Karmakar and C. Dasgupta, Sci. Rep. **5**, 12577 (2015).

[21] Y. Oku, K. Takae, and A. Ikeda, Preprint, arxiv 2004-02103 (2020).

[22] Y. Hatwalne, S. Ramaswamy, M. Rao, and R. A. Simha, Phys. Rev. Lett. **92**, 118101 (2004).]

[23] A. Basu, J. F. Joanny, F. Julicher, and J. Prost, New J. Phys. **14**, 115001 (2012).

[24] I.M. Lifshitz and V.Y. Slyozov, J. Phys.Chem. Solids, **19**, 1961.

[25] E. Velasco and S. Toxvaerd, Phys. Rev. Lett.71, 388(1993).

[26] S. Ahmad, S. K. Das, and S. Puri, Phys. Rev. E85,031140 (2012).

[27] A. Craievich and J. M. Sanchez, Phys. Rev. Lett. 47, 1308 (1981).

[28] Y. C. Chou and W. I. Goldburg, Phys. Rev. A 23, 858 (1981).

[29] J. S. Langer, inSolids Far from Equilibrium, edited byC. Godr'eche (Cambridge University Press, 1992).

[30] A. Bray, Advances in Physics43, 357 (1994).

[31] H. Nagamanasa, K. Gokhale, S. Sood, R. Ganapathy, Nature Phys **11**, 403–408 (2015).

End of Chapter